Structural and geologic controls on gigantic (>1 Gm^3) landslides in carbonate sequences:
case studies from the Zagros Mountains, Iran and Rocky Mountains, Canada

by

Nicholas Jason Roberts

A thesis
presented to the University of Waterloo
in fulfillment of the
thesis requirement for the degree of
Master of Science
in
Earth Sciences

Waterloo, Ontario, Canada, 2008

AUTHOR'S DECLARATION

I hereby declare that I am the sole author of this thesis. This is a true copy of the thesis, including any required final revisions, as accepted by my examiners.

I understand that my thesis may be made electronically available to the public.

Abstract

Gigantic landslides are those greater than 1 Gm^3 in volume. They include the very largest landslides on Earth and on continental landmasses they reach volumes in excess of 10's of Gm^3. Two gigantic landslides in carbonate sequences were studied through a combination of remotely sensed (orbital and aerial) datasets and detailed field investigation. Remotely sensed datasets included orbital optical imagery (Landsat and SPOT), digital elevation models (Shuttle Radar Topographic Mission and Canadian Digital Elevation Database). Field investigations supplemented the remote analysis at both sites by providing outcrop-scale characterization, structural measurements, geomechanical characterization and ground truthing. The work presents the first detailed documentation of the Seymareh (Saidmarreh) landslide, Zagros Mountains, Iran, which is shown to be the largest known rock avalanche in the world and the largest known landslide of any type on the Earth's land surface. Volume of the Seymareh rock avalanche (38 Gm^3) was previously underestimated by nearly 50 percent. The failure mode was complex planar sliding involving fold-related bedding-parallel shears and local break-through of bedding. The overall dip of the sliding surface was 11°. Lateral release and toe release were provided by tectonically-weakened joints and by break-out likely assisted by fluvial undercutting, respectively. Broad scar morphology and outcrop-scale features indicate the presence of nine discrete sliding surfaces distributed through the failed sequence and define nine stacked plates involved in the detachment. The plates enhanced mobility of the rock avalanche during initial transport through upward-increasing cumulative displacement in the failed mass. A radiocarbon date (8710 ± 80 years B.P.) from detrital charcoal near the bottom of a 130 m thick lacustrine deposit form by a lake dammed by the debris indicates a younger age (~9,000 years B.P.) than that previously suggested (10,370 ± 120 years B.P.). The Valley of the Rocks rock avalanche (1.3 Gm^3), Rocky Mountains, Canada is also described in detail for the first time and is shown to be the largest known rock avalanche in North America as well as the largest known landslide of any type in Canada. The failure mode was simple planar sliding along a bedding-parallel, slightly concave-up surface possibly coinciding with a thrust fault (average dip 25°). Lateral release and toe release were provided by bedding-normal joints and by glacial undercutting, respectively. Transport and emplacement involved two stages: the initial rock avalanche and a secondary distal flow due to undrained loading of valley bottom sediments. Geomorphic evidence suggests failure was post-glacial, likely 9,000 to 10,000 years B.P. There is a surprisingly high degree of similarity between the two rock avalanches, despite differences in tectonic and climatic setting. The most influential

preconditions of failure for both landslides were landscape-scale attributes. Detachment was determined by a high degree of structural continuity and slope geometries that led to large planar failures. Geologic structure also influenced initial transport in the case of the Seymareh rock avalanche. Although the landslides differ by more than an order of magnitude, some aspect ratios of the two source areas are comparable. Depth:length ratios are similar while the depth:width is much greater for the Seymareh landslide, suggesting that 1) there may be a relationship between slope length and limiting failure depth, and 2) the greater volume of the Seymareh landslide resulted mainly from greater failure width (15 km). Similarities and differences between the two gigantic landslides suggest several factors important in volume determination of gigantic landslides in carbonate sequences: 1) extensive contiguous source slope; 2) high degree of structural continuity, especially across slope parallel to strike; 3) a comparatively low failure surface dip; 4) discontinuity-parallel slopes, and subsequent toe undercutting; and 5) hard-over-soft geomechanical contrasts. Comparison with magnitude-mobility relationships for landslides over five orders of magnitude shows that both landslides fit the expected trend. The Valley of the Rocks rock avalanche has not previously been considered. The Seymareh rock avalanche suggests an upper limit for landslide magnitude (~40 Gm^3) and, therefore, mobility (fahrböschung = ~4°) on the Earth's continental surface.

Acknowledgements

I would like to thank Professor Stephen Evans for the outstanding support and inspiration he provided throughout my degree.

Numerous individuals provided crucial assistance during the investigation of each the Seymareh and Valley of the Rocks rock avalanches. Their help is greatly appreciated. Dr. Hossein Memarian (University of Tehran and University of Waterloo) facilitated work in Iran and contributed to useful discussions about the Seymareh rock avalanche. Masoud Mojarab (University of Tehran) was of great assistance in the field and in acquisition of topographic maps and aerial photographs. Staff at the Seymareh Hydroelectric Project (Iran Water and Resources Power Development Company) provided critical assistance both during fieldwork at the Seymareh rock avalanche and in acquisitions of Iranian data sources. Arash Saliminia , Reza Sekhavat, Rahim Bogari and MohammadReza NoriNejad were particularly helpful. Ali Shafiei Reza Jalali (University of Waterloo) assisted in translation of key documents.

Katya Pioro (Moscow State University) was of great assistance in the field during site investigation of the Valley of the Rocks rock avalanche. Staff at the Mount Assiniboine Lodge provided important local knowledge about the Valley of the Rocks area. The British Columbia Ministry of Environment granted authorization to conduct research in Mount Assiniboine Provincial Park.

I am without end grateful to my family, would have been incredibly supportive throughout my entire education. Finally, I thank Karen – I cannot express how much your undying support means to me and how much it has helped me.

"I have traveled for geological purposes quite extensively, but can truthfully say that no geological phenomena has impressed me more than this enormous rockfall, that is so large that a whole generation of geologists failed to explain its debris – probably because their route followed the distal edge of the debris where it had reached ca. 2000 feet above its lowest point. Had satellite or air photographs been available it would have been seen immediately for what it was!" (Voight and Pariseau, 1978)

(Norman L. Falcon, letter to Barry Voight referring to the Seymareh rock avalanche, Zagros Mountains, Iran)

Table of Contents

List of Figures

List of Tables

List of Appendices

Chapter 1
Overview

1.1 Gigantic landslides

Gigantic landslides are those exceeding a cubic kilometre (1 Gm^3) in volume. On the Earth's continental surface gigantic landslides range up to nearly 40 Gm^3 (Chapter 2), while submarine landslides up to 1000-3000 Gm^3 (Gee et al., 2007; Talling et al., 2007) and extraterrestrial landslides up to 1000-5000 of Gm^3 (Lucchitta, 1979; Quantin et al., 2004) are known. A 1 Gm^3 cut-off is appropriate as it is convenient and includes most landslides widely recognized as exceptional events on historic and even geologic time scales.

Gigantic sub-aerial landslides occur in most mountain belts of the World (cf. Harrison and Falcon, 1937; Kojan and Hutchinson, 1978; Peart, 1991; Pollet and Schneider, 2004) and are associated with the instability of stratovolcanoes within volcanic belts of the world (Figure 1.1). The global distribution of gigantic landslides may be attributed to some combination of factors largely determined by tectonics, geologic structure, uplift, volcanism and seismicity, as well as exogenous conditions such as climate. These factors influence rates of the denudation of relief (Burbank and Anderson, 2001). For non-volcanic gigantic landslides planar sliding is the most common failure mode, and rocks involved are most commonly sedimentary sequences, especially in the case of the largest failures (cf. Deplazes et al., 2007; Harrison and Falcon, 1937 and 1938; Philip and Ritz, 1999).

By the very nature of landslide magnitude-frequency relationships, gigantic landslides are uncommon (cf. Guthrie and Evans, 2007). Consequently, relatively few examples exist for study (Figure 1.1) and only a small number have occurred in historical time. Additionally, nearly all historical gigantic landslides have been relatively small (e.g. 1911 Usoi, Tajikistan 2 Gm^3 (Schuster and Alford, 2004); 1974, Mayunmarca, Peru, 1.6 Gm^3 (Kojan and Hutchinson, 1978); 1988 Kaiapit, Papua New Guinea, 2 Gm^3 (Peart, 1991)).

1.1.1 Importance

Although gigantic landslides are very rare relative to smaller scale mass movements documentation and understanding of their processes is particularly important for three reasons:

Firstly, behaviour of gigantic landslides differs from that expected from smaller-scale landslides. Landslide mobility typically increases with size (Hayashi and Self, 1992; Legros, 2002), suggestive of strong scale effects.

Secondly, gigantic landslides can pose a significant, but undervalued, hazard in mountainous terrains. Because of their ability to impact large areas and their long-run out, gigantic landslides have high potential to negatively impact communities and infrastructure in mountainous areas. Uncertainty about the hazard posed by gigantic landslides is especially high because of the general lack of knowledge about their behaviour and timing.

Thirdly, gigantic landslides exert major and long-lasting influences on landscapes. The degree of instantaneous modification of natural landscapes due to gigantic landslides can exceed annual sediment transport in the ranges they occur in. Modification include major disturbance of drainage, including damming of large lakes, (Hewitt, 1998; Korup, 2004; Korup et al., 2006) and shaping of mountain slopes (Cruden, 1976). Persistence of landscape modification by gigantic landslides exceeds 10^7 years (Guthrie and Evans, 2007).

1.1.2 Investigation methods

Large landslides are difficult to detect on the ground, but detection and description are facilitated by interpretation of small-scale aerial photographs (Dishaw, 1967), although dimensions of some of the largest gigantic landslides (10s of kilometres) make even the use of aerial photographs difficult. Consequently, some form of remote sensing is integrated in most modern studies of gigantic landslides on the surface of the Earth. Aerial photographs are the traditionally-used remote dataset (cf. Hancox and Perrin, 1994; Watson and Wright, 1969). Similarly, remote sensing is required for investigation of submarine (cf. Gee et al., 2007; Talling et al., 2007) and extraterrestrial (cf. Lucchitta, 1979; Quantin et al., 2004) landslides because of their size and inaccessibility.

Due to accelerated development of space and sensor technology since the 1970s, the use of orbital (optical and RADAR) datasets is increasingly common (c.f Philip and Ritz, 1999; Strom and Korup, 2006). Because of limitations of aerial and orbital remote sensing in resolution, accuracy, type of information conveyed and viewing geometry, field investigation is a critical part of the holistic investigation of gigantic landslides. Some reconnaissance studies of gigantic landslides, however, use remote sensing as a surrogate for field investigation (Strom and Korup, 2006).

The present investigation is the first to combine field investigation, analysis of aerial imagery, analysis of orbital imagery and orbital topographic data. Field investigation included geologic and geomorphic mapping, measurement of the orientation of major structural features, characterisation of geomechanical

strength and, at one site, sampling for radiocarbon dating. Remotely sensed datasets were used to describe and to characterize the degree of continuity of large scale features. Specifically, optical orbital imagery was used for consideration of landscape-scale features, while vertical aerial photographs facilitated observation at scales intermediary between outcrop- and landscape-scales. Orbitally-derived topographic data aided structural characterization and evaluation of three dimensional metrics.

1.2 Objectives

The chapters that follow address two aspects of knowledge about gigantic landslides. Firstly, results of detailed investigations of two gigantic rock avalanches by means of combined field investigation and remote sensing provide fundamental documentation of specific landslides. Secondly, important characteristics observed from the two case studies contribute to knowledge of gigantic landslides in a global context, particularly in understanding landscape and rock mass controls on landslide size and initiation. Specifically, the present work has four objectives:

1. Provide the first ever detailed geomorphic, geometric and geomechanical documentation of the Seymareh (Zagros Mountains, Iran) and Valley of the Rocks (Rocky Mountains, Canada) rock avalanches.

2. Analyze factors influencing the size, detachment and initial transport of these two gigantic landslides.

3. Develop geomatics-based methodology for site investigation of gigantic landslides.

4. Extend knowledge of non-volcanic gigantic landslides on the Earth's continental surface.

1.3 Structure of the thesis

The Seymareh rock avalanche (Zagros Mountains, Iran) is one of the largest and best known landslides on Earth. Despite being known for over 70 years, however, it is grossly understudied in the geologic literature. Chapter 2 presents the first detailed geomorphic and geomechanical investigation of this spectacular natural feature. New findings about the Seymareh rock avalanche include a dramatic correction to its estimated volume, greater constraint on its age, and proposal of the first ever geomechanical model that explains its enormous size and initiation.

The Valley of the Rocks rock avalanche (Rocky Mountains, Canada; Evans, 2001) is the largest known non-volcanic catastrophic landslide in North America. Consequently, it is unique in a Canadian context, and at the same time is representative of large mass movements in the Foreland Belt of the North American Cordillera. Despite this importance, it is almost unknown in the geologic literature and is

3

missing from all global reviews of large landslides. Chapter 3 provides the first comprehensive documentation and analysis of the Valley of the Rocks rock avalanche.

Chapter 4 compares the size, detachment and transport of these two gigantic landslides and the ultimate factors determining their size and mobility. Consequently, the discussion presented in Chapter 4 suggests implications of the current work in improving the general understanding of gigantic landslides on the Earth's continental surface.

Methodological approaches are outlined in detail in appendices. Specifically, these include: the remote sensing-based approach for investigation of gigantic landslides (Appendix A), explanation of the determination of geometrics of gigantic landslides (Appendix B) and field-estimation of rock mass strength in the case of the Seymareh rock avalanche (Appendix D). Additional appendices contain collected data. Structural measurements for the Seymareh rock avalanche and details of a sample used for radiocarbon dating of the rock avalanche are contained in Appendices C and E, respectively. Structural measruements for the Valley of the Rocks rock avalanche are contained in Appendix F.
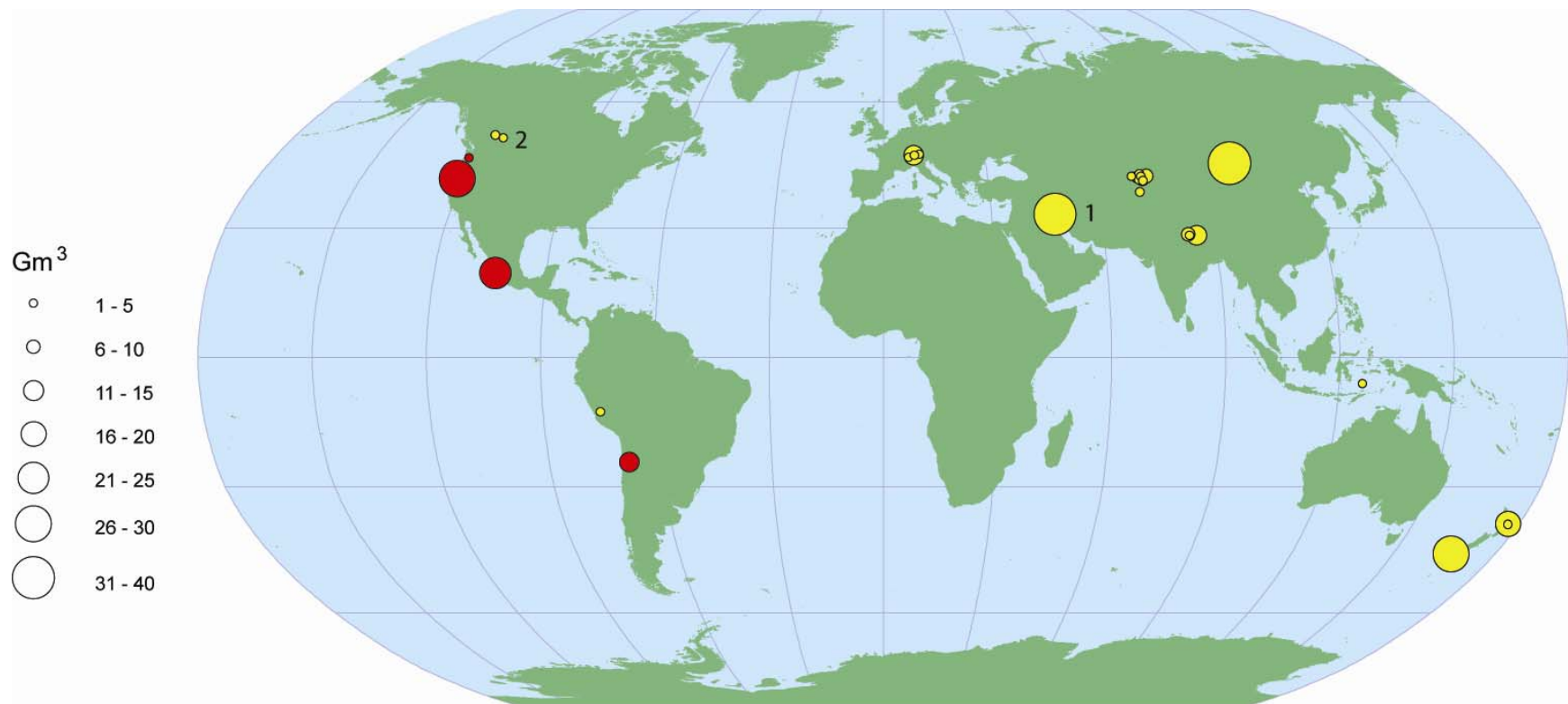
Figure 1.1:Global distribution of gigantic (1 Gm^3 or larger) landslides (n = 30).

Both volcanic (red; n = 4) and non-volcanic (yellow; n = 26) are included. Landslides investigated in this work are 1) Seymareh rock avalanche, Zagros Mountains and 2) Valley of the Rocks rock avalanche, Rocky Mountains.

Chapter 2

The Seymareh (Saidmarreh) rock avalanche, Zagros Mountains, Iran; the largest rock avalanche in the World

2.1 Introduction

2.1.1 Overview

The prehistoric Seymareh (Saidmarreh) landslide in the foreland margin of the Zagros Mountains, Iran is one of the largest known on the Earth's continental surface. The landslide occurred along the provincial border between Ilam and Lorestan, 60 km west of the Iraqi border. Failure initiated as a gigantic, catastrophic, carbonates-mudrock rockslide from the flank of the Kabir Kuh anticline in eastern Ilam province and travelled into the adjacent province of Lorestan, crossing a wide synclinal valley, and over-topping the nose of a plunging anticline before continuing well into the next valley. The extensive debris sheet dammed two of the largest rivers in the western Zagros, producing extensive lacustrine deposits.

2.1.2 Previous investigations

An early scientific investigator in the Zagros Mountains mistook the debris for moraine (de Morgan, 1895), presumably because of its immensity, morphology and material characteristics. Harrison and Falcon (1937) were the first to recognized the feature as a landslide. Initial investigations of the landslide (Harrison and Falcon, 1937; 1938) provided thorough descriptions of the debris and landscape impacts, as well as rough dimensions and morphology of the source area. These first papers are the only ones to discuss detachment of the landslide. Harrison and Falcon (1938) also discussed triggers and transport mechanisms, and suggested the failure initiated as an incipient 'knee flap' (Harrison and Falcon, 1934; 1936).

Later, Oberlander's (1965) brief re-evaluation of geomorphic preconditions of failure spawned renewed interest in the landslide. Later work in the 1960s focused on mechanisms of debris transport and emplacement. Watson and Wright (1969) discussed final stages of transport and debris emplacement based on debris surface features mapped from high altitude aerial photographs. In their synopsis of Harrison and Falcon's (1937; 1938) benchmark works, Shoaei and Ghayoumian (2000) suggested a volume between 24 and 32 Gm^3 based on rough source area dimensions. Despite the greater volume suggested by Shoaei and Ghayoumian's (2000) reconnaissance study, initial work by Harrison and Falcon (1937; 1938) remains the source of basic metrics (20 Gm^3 volume) for the landslide (cf. Legros, 2002).

2.1.3 Contributions of the present work

The Seymareh has been known for nearly 80 years and is one of the most cited landslides in the geoscience literature; mention of the landslide is included in investigations of other gigantic landslides (cf. Bown et al., 1985; Lucchitta, 1978; Schuster and Alford, 2004), reviews of landslide research (cf. Schuster and Highland, 2007; Voight and Pariseau, 1978), work on rock avalanche mechanics (cf. Kent, 1966; Melosh, 1979; Shreve, 1968; Yarnold, 1991), and studies of empirical relations between landslide metrics and mobility (cf. Hsü, 1975; Legros, 2002; Scheidegger, 1973). The Seymareh landslide has, however, never been documented in detail. The source area is particularly understudies, being only loosely depicted in maps in previous investigations (Harrison and Falcon, 1937; 1938; Watson and Wright, 1969). The lacking data and documentation precluded detailed analysis of the landslide. The resulting knowledge gaps include understanding of factors influencing the occurrence and behaviour of the landslide and determination of mechanisms of detachment, transport and debris emplacement.

The present study fills many of these gaps through the first ever detailed documentation and analysis of the Seymareh rock avalanche. The new investigation was facilitated by rigorous collection of new data, application of modern techniques, and review of the large body of work that has been conducted on the structure and stratigraphy of the Zagros since the initial studies of the landslide in the 1930s. The latter includes detailed mapping due largely to sustained petroleum interests and development of hydroelectric projects (cf. Ghobadi et al., 2005; Gholipour, 1998; James and Wynd, 1965).

The current work provided numerous contributions to documentation and analysis of the Seymareh rock avalanche. Using orbital and aerial remotely sensed datasets, accurate geometrics are determined including reassessment of those estimated by Harrison and Falcon (1937; 1938) as well as establishment of some never previously reported. Investigation of the source area, which was lacking in all previous studies, has allowed the first ever structural characterization, kinematic analysis and geomechanical documentation of the landslide. Subsequently, understanding of detachment and initial transport mechanisms, of preconditions of failure, and of factors determining the size of the landslide are provided for the first time. Additionally, a new AMS radiocarbon date provides additional constraint on the age of the landslide.

2.2 Data sources and methods

2.2.1 Remote sensing

Remotely sensed imagery has commonly been used for assessment of gigantic landslides (cf. Philip and Ritz, 1999; Strom, 1998; Strom and Korup, 2006; Zhou et al., 2001). The present analysis improves upon

this approach through the multi-scale datasets including stereoscopic aerial photography and through detailed use of orbitally-collected elevation data. The methodology is outlined in detail in Appendix A.

Two orthorectified Landsat7 ETM+ images and a single 10 m un-orthorectified SPOT image provided coverage of the landslide and adjacent terrain (Appendix A). For each image bands were individually contrast-enhanced using linear histogram stretches and combined as colour and false colour composites. Multispectral Landsat composites (30 m) were pan-sharpened using the panchromatic band (15 m). Medium scale (1: 60 000) panchromatic aerial photographs produced in 1955 for the United States Army Map Service, Corps of Engineers, provided coverage of the landslide source area and debris.

Optical systems were used for qualitative interpretations and quantitative assessment of horizontal metrics (Appendix B) of the landslide. Pan-sharpened Landsat7 ETM+ composites were used for characterization and mapping of regional- and macro-scale features, and for determination of metrics. Large outcrop-scale features (e.g. major fractures) were clearly discernable on the SPOT image, which was thus, used to aid interpretation of Landsat images. Because of non-systematic distortions, the SPOT image was not used for quantitative characterization of metrics. Aerial photographs facilitated interpretation of outcrop-scale features not discernable on the orbital imagery and aided stratigraphic correlation of field observations.

Quantitative assessment of metrics with vertical components (Appendix B) was based on a SRTM (Shuttle RADAR Topographic Mission) DEM (digital elevation model). Absolute horizontal and vertical errors for the dataset are 20 m and 16 m, respectively (Farr et al., 2007). Data gaps in interferometric RADAR DEMs are common in areas of high relief due to topographic shadowing. General relief in the Zagros fold-thrust belt is not extreme compared to other mountain chains, but some gaps occur in the study area typically corresponding with tangs (local term for steep canyons eroded across anticlines by transverse drainage), cliffs at lateral margins of the landslide or the steep upslope-facing portion of the head scarp.

2.2.2 Field data collection and ancillary data sources

Fieldwork included structural measurement of bedding surfaces, geologic and geomorphic mapping, and assessment of geomechanical strength based on a modification of the Geological Strength Index (GSI). Field traverses focused mainly on the source area because of the lack of previous documentation.

Remote sensing analyses and field investigations were checked against ancillary sources. Geologic maps (1: 100 000) compiled by the Iranian Oil Operating Companies in the 1960s were used to assess geologic observations and 1: 50 000 national series topographic maps were used to check elevations and horizontal metrics. Extensive literature on the stratigraphy (Alavi, 2004; Alavi and Mahdavi, 1994;

Amirshahkarami et al., 2007; Ghasemi-Nejad et al., 2006; Hessami et al., 2001; James and Wynd, 1965; Mohseni and Al-Aasm, 2004; Motiei, 2003; Setudehnia, 1978; Vaziri-Moghaddam et al., 2002), structural geology (Alavi, 2007; Gholipour, 1998; McQuillan, 1973; McQuillan, 1974; McQuillan, 1985; Stephenson et al., 2007; Wennberg et al., 2006) and tectonics (1937; 1938) of the Zagros Mountains aided development of a geologic model.

2.3 Study area

Initial investigations recognized the importance of structural and lithologic control in failure (Harrison and Falcon, 1937; 1938). Understanding detachment mechanisms of the landslide requires understanding of these controls. Determining the ultimate causes of the landslide, however, requires consideration of the tectonic setting, the form of the Kabir Kuh anticline and stratigraphy. Increased understanding of these aspects of the Zagros orogeny has resulted from resource development in the region, technological advancements and continued scientific investigations. Petroleum exploration and hydroelectric development had improved understanding of geology of the Zagros including stratigraphy (cf. Alavi, 2004; James and Wynd, 1965; Murris, 1980), structure (cf. Alavi, 2007; Stöcklin, 1968) and geomechanics (cf. Ghobadi et al., 2005; McQuillan, 1973; McQuillan, ; Stephenson et al., 2007). Modern technologies have improved characterization and understanding of tectonics in the region (cf. Hessami et al., 2006; Vernant et al., 2004).

2.3.1 Regional setting

The Zagros Orogeny forms a ca. 1,500 km segment of the Alpine-Himalayan Orogenic system between Eastern Turkey and the Strait of Hormuz. The Neo-Tethys sea, which separated Arabia and Iran, formed along this axis by Triassic extension and subsequently closed during the Mesozoic and Tertiary by northeast sea floor subduction under Eurasia (Berberian and King, 1981; Falcon, 1974). Continental collision and subsequent subduction of the Arabian plate began in the Neogene (Stöcklin, 1968) and initiated formation of the present day Zagros Mountains (Sepehr and Cosgrove, 2004).

2.3.1.1 Tectonics

Far field stress conditions are heterogeneous along the belt due to obliquity of convergence and rotation of the Arabian plate (McClusky et al., 2003; Vernant and Chery, 2006; Vernant et al., 2004). Current shortening is 9 ± 2 mm yr^{-1} and 4.5 ± 2 mm yr^{-1} in the southeast and northwest of the Zagros, respectively (Vernant et al., 2004). Convergence is nearly frontal in the southeast with negligible strike-slip displacements, but in the northwest it is oblique (~45°) and includes a significant component of right-lateral strike-slip (Walpersdorf et al., 2006). Cumulative shortening of the belt in the Lorestan region is

estimated at 57 km (McQuarrie, 2004). In addition to across-belt shortening, along-strike extension of the belt has been observed (Hessami et al., 2006).

A ca. 12 km thick cover sequence of sandstone, limestone and shale (Falcon, 1969; Stöcklin, 1968) is separated from the underlying Precambrian basement by décollement within the Cambrian Hormoz Salt (Berberian, 1995). Shortening within the cover sequence is accommodated by folding and reverse faulting. The Gachsaran Formation provides an upper décollement detachment within the cover sequence (Berberian, 1995).

Faulting is predominated by belt-parallel reverse faults. Northeast-dipping basement faults are suspected to be reactivated normal faults formed during Triassic extension (Jackson, 1980a). High angle reverse and thrust faults developed within the cover sequence likely nucleate at basement irregularities, such as basement fault scarps, although some may also occur as continuations of basement faults (Blanc et al., 2003). Relatively few faults reach the surface (Berberian, 1995), but many of those that do run nearly the entire length of the range or compose fault systems that do (Figure 2.2).

Focal mechanisms (Tatar et al., 2004) and geodetic measurements (Hessami et al., 2006) reveal transverse faulting, principally dextral, concentrated in the central and northwest Zagros (Figure 2.2). Many of the larger dextral faults form transfer faults linking dip-slip faults (Figure 2.2) (Sepehr and Cosgrove, 2004). They may, however, also occur independent of major faults (Tatar et al., 2004). Transverse faulting is thought to result from the oblique convergence between the Arabian and Eurasian plates, which is accommodated by right-lateral shear (Stephenson et al., 2007; Tatar et al., 2004).

The Zagros orogeny is divided into two parts (Alavi, 2007): the Zagros imbricate zone and the Zagros fold-thrust belt.   Shortening began at the Arabia-Eurasian suture, defined by the Zagros Main Thrust fault (Figure 2.2), and migrated toward the forelands causing deformation and uplift to decrease toward the southwest (Figure 2.2). Consequently, folds in this Zagros imbricate zone have been destroyed by intense thrusting and erosion since the Late Cretaceous whereas folds in the less deformed Zagros fold-thrust belt remain largely intact.

2.3.1.2 Geology

Belt-parallel tectonic zones are further subdivided into basins (Oberlander, 1965), typically separated by transverse faults (Bahroudi and Koyi, 2004). Tectonic structures determined stratigraphic variations between these basins, and the resulting rheological differences influence deformation (Sepehr and Cosgrove, 2004) as well as secondary features such as fracture spacing and persistence (Stephenson et al., 2007). Geology of Lurestan shows broad alternations of competent typically highly fractured (characterised by the Asmari Limestone, which is a major ridge-forming unit and petroleum reservoir

throughout the Zagros fold thrust-belt) and incompetent less fractured units (Figure 2.3). Similar stratigraphic successions are present throughout the Zagros and result from basin migration normal to the trend of the range (Alavi, 2004; Berberian and King, 1981).

2.3.1.3 Physiography

Tectonic structural elements and stratigraphy strongly control physiography in the Zagros fold-thrust belt since destruction by surficial faulting and erosion is relatively limited. Folds are typically symmetrical to slightly asymmetrical and are commonly crossed perpendicularly by transverse drainage (Oberlander, 1965). Most anticlines are well preserved 'hog-back' forms because of their resistant Asmari Limestone carapaces are largely intact. Folds with breached carapaces show exposed cores of alternating layers of resistant and weak units forming in some cases small perched basins. Where breaching reaches a lower highly resistant unit (e.g. Sarvak Formation), the anticlines form a pair of parallel ridges composed of stratigraphically higher resistant flank lithologies, which are often incised to form cols. The two ridges are often separated a minor ridge formed by the lower resistant unit in the hinge region of the anticline. Synclines contain units overlying the Asmari as well as Quaternary sediments. The highly mobile Gachsaran Formation predominates in many valley bottoms where it is commonly rilled to form badlands exhibiting up to 100 m of relief.

2.3.2 Kabir Kuh anticline

The landslide slid from the northeast flank of Kabir Kuh (Great Mountain), an anticline situated along the foreland periphery of the fold-thrust belt. Kabir Kuh is a unique structural and topographic feature in the Zagros mountains; it is the longest anticline in the Zagros fold-thrust belt (Blanc et al., 2003), and exceeds adjacent folds in amplitude, wavelength and degree of erosion. Unlike adjacent anticlines, the crest of Kabir Kuh has been breached and greatly eroded. Despite such denudation, crestal elevations of Kabir Kuh are much greater than adjacent, un-breached folds. The only fault feature observed in the vicinity of the failed portion of Kabir Kuh is a high angle fault present in the headscarp region; evidence is lacking of faulting near the toe of the failed slope.

2.3.2.1 Formation and structure

The form of Kabir Kuh is defined by both its folding and belt-scale tectonics. Advanced formation and erosion of Kabir Kuh indicates it greatly predates adjacent folds. Oberlander (1965) suggested that the anticline initiated in the Oligocene, well before advancement of the Zagros fold front to the vicinity of Kabir Kuh in the Middle-Late Miocene (Hessami et al., 2001). Additionally, its greater wavelength (ca. 10-15 km) than adjacent folds (2-5 km) suggests possible differences in formation. Two tectonically-

driven models for the formation of Kabir Kuh could explain these observations: origin as a forced fold in the hanging wall of a thrust (Alavi, 2007; Blanc et al., 2003); or propagation of a thrust fault in the core of the anticline that is either blind (Blanc et al., 2003) or does not greatly displace strata at the surface of the fold (Setudehnia and Perry, 1967a).

Structural continuity of bedding within the limbs of Kabir Kuh is high both down-slope, due to its box fold form (Blanc et al., 2003), and along slope, due to its length (ca. 200 km). The only major deviations in continuity are steepening near fold hinges (Figure 2.4) and large-scale sinuosity of the fold axis (Figure 2.2). Sinuosity of the fold axis may result from forced formation over a series of linked fault segments (Blanc et al., 2003), expression of structural grains superimposed onto the current orogeny from earlier tectonics events (cf. Alavi, 2007) or, following its initiation, movement along blind transform faults resulting from oblique plate convergence.

Kabir Kuh is one of the few structures in the Zagros Orogeny to oppose major drainage cutting across the trend of the range (Harrison, 1945; Oberlander, 1965; 1985), which can be explained by its early formation (Oberlander, 1965) and large topographic scale. Kabir Kuh results in the diversion of two major rivers – first the Seymareh and then the Kashgan – which together drain a large portion of the fold-thrust belt (Oberlander, 1965).

2.3.2.2 Geology

The Asmari carapace that once covered Kabir Kuh remains only in the southeast end of the northeast limb of the anticline, particularly on its northeast flank. Breaching and erosion has exposed alternating limestone and mudrock units down to the Sarvak Formation (Cretaceous) (Figure 2.4). Strength contrasts between stratigraphic units results in a number of unique features: secondary valleys within the anticline where incompetent units have been more rapidly eroded, and ridges broken by cols along the flanks of the anticline due to fluvial erosion of more resistant units, likely along joints.

2.4 Observations and data

2.4.1 Debris

2.4.1.1 Metrics and morphology

The debris sheet measures 16.1 km parallel to runout and at its widest is 20.7 km transverse to runout. Total debris area is at least 196 km^2. Low-lying marginal debris emplaced in the Seymareh and Kashgan valley bottoms was subsequently buried under lacustrine deposits of the Seymareh and Jadiar lakes

respectively (Figure 2.5). Areas buried by lacustrine sediments extend far in from original debris limits and cause the presently exposed debris to take on a more lobate form in plan view. The area of the currently exposed debris, therefore, underestimates the total debris area, which was more likely ca. 220 km^2.

Total in-situ debris volume is estimated as 44 km^3. Debris is thickest (up to ~300 m) in the mid-proximal portion and thins toward the edges. Based on the estimated total debris area (220 km^2) and calculated debris volume, average thickness for the entire debris sheet is ~200 m. Surface relief of the debris ranges up to ca. 200 m due to the presence of broad waves in the debris and the formation of grabens on its surface, as noted also by Watson and Wright (1969).

Debris ran out a horizontal distance of 19 km from the crest of the source slope (L) over a total vertical distance of 1210 m (H), yielding a fahrböschung (vertical angle between the upper limit of the landslide scar and the distal debris limit defined by tan^{-1}(H/L)) of 3.6° (Figure 2.5c).

2.4.1.2 Lithology

Lithology varies along the debris sheet in a proximal-distal direction (Figure 2.6). On this basis, the debris sheet is divided into two parts: distal and proximal (Figure 2.5 b and c). The distal portion of the debris is completely composed of brown weathered Asmari Limestone ranging from fines up to boulders measuring 10s of metres in all directions (Figure 2.6a). All of the Asmari debris is highly angular and typically blocky, regardless of size (Figure 2.6a), and is highly weathered (Figure 2.6b). The proximal limit of the Asmari-dominated debris occurs in the vicinity of the Seymareh River (Figure 2.5b). At this limit, either blocky limestone debris lies adjacent to Eocene mudrocks along a discrete front (Figure 2.6c), or the ground surface is composed predominantly of Eocene mudrocks with large brown weathered limestone boulders perched on top (Figure 2.6d and e).

The proximal third of the debris is predominantly grey to buff weathered Eocene much rocks (Pabdeh and Gurpi Formations), especially that part still within the scar, which is completely composed of this material. Most of this material is gravel-sized (or finer) with boulders being uncommon (Figure 2.6f). Where boulders do occur, they are generally composed of interbedded shale and limestone (Figure 2.6g).

2.4.2 Source area

2.4.2.1 Morphology and metrics

The scar delineating the source area of the landslide has a very blocky form that steps upward toward the lateral margins and in a down-slope direction from the head scarp. Margins are defined by very high (up

13

to over 350 m) nearly vertical cliffs aligned parallel to the dip direction of the northeast flank of Kabir Kuh. A significant amount of talus has built up at the base of these cliffs. Lesser scarps within the scar are much lower (25 – 85 m) and are of various orientation including lateral and upslope scarps. In the deepest part of the source area, dendrite drainage has developed and relief is generally less dramatic than elsewhere in the scar.

The initial rockslide was 15.5 km wide (across slope, parallel to strike), 7.0 km long (down-slope, parallel to dip), covering an area of nearly 200 km^2 (normal to bedding). The total failure surface is more extensive than reported by Harrison and Falcon (1937; 1938). Previous investigations estimated scar width with reasonable accuracy, but estimated scar length as only 4.0 (Harrison and Falcon, 1937) to 5.0 km (Shoaei and Ghayoumian, 2000). The actual scar length (7.0 km) was determined by extrapolating the sliding surface down to the Seymareh Valley, as kinematically required for failure (see section 2.5.2), and by correction for orthographic viewing of an inclined surface. The latter resulted in a 6% upward correction of plane length and, therefore, scar area.

Thickness of the failed rock mass ranged from 250 m, along the left lateral margin, to 680 m, in the central upper region of the scar. Thickness of the failed mass is consistent over large areas (up to 25 km^2). Area-weighted thickness was ~ 410 m. Based on consideration of regular thickness variations over the blocky scar and areas of regions of consistent thickness, the volume of the failed mass is estimated as 38 Gm^3 (see Appendix B for details).

2.4.2.2 Structure

The broad steps composing much of the basal surface of the scar are seen in remotely sensed imagery to vary in size, shape and level (Figure 2.5b), but having similar orientations that align with the topographic surface of Kabir Kuh on either flank. Field observations indicate that the steps are the surface expression of either single extensive bedding surfaces or a combination of several bedding surfaces of close stratigraphic position. Average structural measurements of bedding surfaces collected throughout the source area (Appendix C.1) vary in dip from 14 to 23° and strike consistently west northwest confirming that the structural continuity of bedding within the limbs of Kabir Kuh is high both down-slope (Figure 2.7) and along slope. The only major deviation in continuity is steepening of bedding in the uppermost part of the scar (Figure 2.4, Figure 2.7).

The outcrop-scale appearance and nature of bedding surfaces varies in different parts of the source area and seems to depend on lithology (Figure 2.8). Resistant limestone bedding surfaces are overall very smooth and show some undulation as well as water-eroded channels. On some of the harder bedding surfaces striations are present (Figure 2.8f). Vertical scarps typically truncated at major bedding surface

(Figure 2.8b and e). In a small number of instances, a gap was present between the bedding surface and the overlying rock mass (Figure 2.8e).

In moderately weak materials, the exposed surface is composed of broken up, thinly-bedded surficial material forming a talus veneer (Figure 2.8a). Gullies 1 – 3 m deep are present on some extensive planar sections of the scar and are oriented directly down-slope (Figure 2.8d). These are most common in thinly-bedded units form surfaces with abundant talus. In such cases the overall surface was bedding-parallel, but structural measurements were made of intact bedding exposed in gullies. In the weakest units, bedding surfaces are not exposed. Instead, bedding outcrops in the sides of weathered slopes.

Bedding normal joints observed in the field show random orientation. Joints are unfilled and are typically closed. Major lateral scarps were observed to form parallel to joints. Weathered joint traces visible on bedding surfaces joints could be detected on aerial photographs and, in most cases, on the SPOT image. Some major highly weathered joint traces were also visible on the Landsat image. Major lateral scarps are visible on all forms of imagery examined and also on the DEM. In the remotely sensed datasets joint traces and lateral scarps show the same preferred orientations (Figure 2.7) (Appendix C.2). Roughly four prominent and highly persistent joint orientations are evident (Figure 2.7).

2.4.2.3 Stratigraphy and geomechanics

Three formations are exposed in the source area (Figure 2.9). The Asmari Formation is composed entirely of limestone and is relatively homogeneous. Individual units of the underlying Pabdeh and Gurpi Formations, however, are characterized by intra-unit alternating lithological variations. The upper Pabdeh is composed of limestone. The middle and lower Pabdeh are composed of interbedded limestone-shale (Figure 2.8c and e), and of a shale unit (Figure 2.8g) containing a single major limestone member, respectively (Figure 2.9). The Gurpi Formation is largely shale with a single major limestone member (Emam Hassan Member; Figure 2.8). Failure involved all of the Asmari and Pabdeh Formaton and the upper shale portion of the Gurpi Formation, totalling 700 m in thickness. The deepest extent of the initial rock slope failure was at the upper contact of the Emam Hassan Member of the Gurpi Formation (Figure 2.8h).

Based on the application of a Geological Strength Index (GSI) chart (Hoek et al., 2005; Marinos et al., 2005) for Kabir Kuh developed for this study (see Appendix D), and supported by other field descriptions from the Zagros fold-thrust belt (Alavi, 2004; James and Wynd, 1965; Motiei, 2003), four major geomechanical units of differing rock-mass strength and deformability characteristics were identified in the failed rock mass (Figure 2.8). The upper two geomechanical units are relatively homogeneous in rock-mass strength, whereas the lower two are very heterogeneous (Figure 2.9). The Asmari Limestone

15

unit, the upper and strongest geomechanical unit, is composed of fractured medium- (zone K1 in Appendix D; GSI = 68) to thin- (zone K2 in Appendix D; GSI = 58) bedded limestone. The underlying Pabdeh Limestone unit is similar to the Asmari Limestone unit, but is more thinly-bedded and, therefore, less resistant (zone K3 in Appendix D; GSI = 50). The Interbedded Pabdeh unit (zone K4 in Appendix D; GSI = 45) is composed of regularly alternating beds of fractured thinly-bedded shaley limestone and shale, while the lowest unit, the Pabdeh-Gurpi Shale unit, is composed largely of shale (zone K7 in Appendix D; GSI = 28) with several prominent fractured, shaley limestone beds. Overall, the failed sequence shows a marked downward reduction in strength, producing a hard-over-soft geomechanical contrast (Figure 2.9), resulting from the competence variations within the regional stratigraphy (Figure 2.3).

Stratigraphic and topographic comparison of the major bedding surfaces exposed in the scar show that all occur at one of nine discrete levels within the sequence (Figure 2.9). The surfaces most commonly occur at lithologic boundaries within the sequence and are concentrated within weaker geomechanical units (Figure 2.9). The Asmari Limestone unit is devoid of major exposed surfaces and only one exposed surface occurs within the underlying Pabdeh Limestone unit. Single exposed surfaces occur near the upper and lower boundaries of the Interbedded Pabdeh geomechanical unit at limestone/shale contacts. Exposed surfaces are most concentrated in the lower two geomechanical units. All three exposed bedding surfaces in the Interbedded Pabdeh unit occur at limestone-shale interbed boundaries. In the Pabdeh-Gurpi Shale unit, all three exposed surfaces correspond to the upper surfaces of major limestone beds. The lower-most exposed surface is the only one not limited to a single stratigraphic level; it is predominantly bedding-parallel, but cuts downward through the shale of the Upper Gurpi Formation to the top of the Emam Hassan Member of the Gurpi Formation in the central region of the headscarp.

Two springs were observed in the source area. Stratigraphic positions of the two observed springs are shown in Figure 2.9. The stratigraphically higher spring issues from a limestone surface while the lower spring issues from a shale sequence.

2.4.3 Lacustrine deposits

Damming of the Seymareh and Kashgan Rivers by the rock avalanche debris resulted in the formation of extensive landslide-dammed lakes and the deposition of 260 km^2 of lacustrine sediments. The lakes were at least as expansive, although their maximum extent is unknown as no shorelines area currently present. Lacustrine deposits are thickest towards their downstream limits (e.g. adjacent to debris) and onlap the debris sheet. Despite substantial erosion, surfaces of the deposits are visibly accordant (Figure 2.10). The present-day Seymareh and Kashgan Rivers have deeply incised the Seymareh and Jadiar lake deposits.

Plan forms of the rivers are meandering and several extensive terraces have been formed in the Seymareh lake deposit.   The upper surface elevation the Seymareh lake deposit is ca. 130 m above outcropping bedrock at the base of the sequence, just up river of the northwest debris margin.

Sediments are rhythmically bedded, being composed generally of a thick coarser grained (fine sand) unit and a thin finer grained (silt) unit that together form rhythmites a few to about 10 cm thick. Given the short amount of time available to investigate the sediments in the field it was not possible to determine if each pair represented an annual deposition cycle. Given the present degree of seasonality in the runoff in the region, inferences of past seasonality (Stevens et al., 2006; Stevens et al., 2001) and the regularity of rhythmic bedding throughout the sequence, it is very likely that each rhythmite represents one annual deposition cycle.

2.4.3.1 Radiocarbon sample

An Accelerator Mass Spectrometry (AMS) radiocarbon date was obtained from charcoal from the Seymareh Lake deposit (Figure 2.11) near the debris dam (Figure 2.5b). The sample was part of a charcoal-rich layer located ~3.5 m above river level (Figure 2.11a) and an estimated 15 m above the base of the 130 m thick lacustrine sequence. The sample was a ~6 x 6 x 3 cm mass of fine grained detrital charcoal fragments with minor amounts of silt and sand (Figure 2.11b). The sample (TO-13445) was processed at IsoTrace Radiocarbon Laboratory at the University of Toronto. The radiocarbon analysis report provide by IsoTrace, including details of sample processing, are provided in Appendix E. The uncalibrated conventional radiocarbon date of the sample is 8710 ± 80 years B.P.

2.5 Interpretations

2.5.1 Metrics

Comparison of volumes of the scar (37 Gm^3) and in-situ debris (44 Gm^3) suggests a 17% bulking during transport, which is broadly typical of values obtained in other large rock avalanches (e.g. Chen et al., 2005). The new estimate of the volume is nearly twice that of the original estimate (Harrison and Falcon, 1937 and 1938) (20 Gm^3) and substantially more than that of Shoaei and Ghayoumian (2000) (24-32 Gm^3). An early typographic error (Harrison and Falcon, 1937) suggesting a volume of 30 Gm^3 was propagated in later literature (Watson and Wright, 1969).

17

2.5.2 Detachment and initial transport

2.5.2.1 Kinematics of detachment

Detachment and initial transport of the Seymareh landslide was strongly controlled by four structural elements: 1) bedding-parallel sliding surfaces; 2) joints accommodating lateral release; 3) break-through between sliding surfaces; and 4) critical toe break-out through the Asmari carapace. The first two types of structures are clearly visible even on coarse resolution orbital imagery and dictate the blocky form of the scar. All four types of structures are required for the failure to have been kinematically possible. Additionally, release along the upper limit of the detachment area was enabled by previous erosional unroofing of the anticline.

The nine stratigraphic levels of major exposed bedding are inferred to be sliding surfaces based on their regularity, continuity and surface features (Figure 2.12). Sliding at the base of the failed rock mass was, therefore, distributed across multiple stratigraphically-defined sliding surfaces. The resulting stepped scar is topographically and stratigraphically deepest in its central region below the crown and at the crown, respectively. High structural continuity over individual sliding surfaces as wellas between different sliding surfaces (Figure 2.7) results from structural uniformity and persistence within Kabir Kuh, which is due to its box fold from and great axial length. Steepening (up to 49°) of the stratigraphically-lowest units is related to proximity to the northeast hinge zone of the box fold (Figures 2.1c and 3.4) near the fold hinge.

Bedding-normal fractures form major lateral release surfaces marking the limit of the detached mass and form lesser lateral release surfaces joining adjacent sliding surfaces of differing levels. Bedding normal joints have been observed to be randomly oriented at outcrop-scale, but show preferred orientation at smaller-scale elsewhere in the Zagros fold-thrust belt (McQuillan, 1973; McQuillan, 1974; McQuillan, 1985). McQuillan (1973) explains this discrepancy as follows: pre-existing (slightly post-depositional) fractures were randomly oriented, but some were subsequently exploited by tectonic stress causing them to be weaker. Regardless of their origin, preferentially weakened orientations are more easily eroded, allowing their identification on remotely sensed imagery while more minor fractures go undetected (McQuillan, 1974; Stephenson et al., 2007).

The four prominent joint orientations visible on remotely sensed imagery are related to far-field stress conditions: NW-SE (fold-axis parallel), NE-SW (fold-axis orthogonal), ca. N-S and ca. E-W (Figure 2.7B). Similar orientations are prevalent throughout the Zagros both at anticline-scale (McQuillan, 1974; Stephenson et al., 2007) and as belt-scale faults (Figure 2.2). The fracture sets represent two sources of exploitation: those generated by fold formation (NW-SE and NE-SW) (Cosgrove and Ameen, 2000), and

those accommodating shear in the cover sequence that results from basement shearing along reactivated faults (N-S and E-W) (Stephenson et al., 2007).

Kinematic release of the Seymareh landslide required break-through across bedding because the slopes of Kabir Kuh are bedding-parallel and bedding does not, therefore, daylight[1]. Failure across bedding was of two types: break-through bedding within the failed mass and a major break-out across bedding from the upper-most sliding surface to the slope surface of the toe of Kabir Kuh. Break-through within failure mass involved breaking across 25 to 85 m thick, relatively weak units. Combined with lateral shearing along lineaments with a down-slope component (N-S, E-W, NW-SE), break-through allowed down-slope transport of the rock mass despite topographic and stratigraphic shallowing of the overall basal failure surface down-slope.

Critical break-out across the 250 m thick resistant Asmari Limestone carapace at the toe of the slope was required to overcome toe support of the failed mass. Harrison and Falcon (1938) suggested pre-failure slumping of the slope as an incipient 'knee-bend' structure (Harrison and Falcon, 1934; Harrison and Falcon, 1936) as a precursory condition of failure. However, field evidence of a pre-failure 'knee-bend' or of any tectonic structures in the Asmari Limestone is lacking and topographic profiles show that slumping has not occurred in either flank. Oberlander (1965) and Watson and Wright (1969) also reported that evidence for a 'knee-bend' is lacking. Oberlander (1965) noted that the Kashgan River possibly forced the Seymareh River closer to the toe of Kabir Kuh in the vicinity of the landslide. Due to the deflection of rivers along the northeast side of Kabir and subsequent concentration of flow in the Seymareh Valley, there was a great potential for undercutting at the toe of the northeast flank of Kabir Kuh. Such undercutting, had it occurred, would have greatly assisted break-out along a continuous length of Kabir Kuh.

Bedding-parallel sliding surfaces, break-through between them and the major toe break-out across the Asmari carapace created a low angle (11°) composite failure surface dipping much more gently than the mean dip of bedding in Kabir Kuh (20°) (Figure 2.13).

2.5.2.2 Plates and platelets

Gross morphology and outcrop-scale observations of detachment surfaces suggest the source rock mass consisted of a series of stacked sliding plates. Nine plates were defined vertically by the nine stacked sliding surfaces and laterally by major joint systems (Figure 2.15). Plates were sheet-like with thickness to width ratios of 1: 50 to 1: 550. Plates decreased in extent (from 100 to 8 km[2]) and, broadly, in strength

downward in the failed sequence. The uppermost plate was composed entirely of the Asmari carapace and was carried passively on the underlying failing plates during initial transport. The lowest three plates were predominantly composed of shale and, therefore, were much less rigid in form. The fragmentation of these lower plates provided the weak mass deposited at the bottom of the slope.

Major joint sets subdivided each plate into multiple platelets. Laterally limiting joints of the plates, preserved as major lateral scarps of the scar and as numerous lesser scarps within the scar, were also probably vertically persistent throughout the stratigraphic sequence. Joints marking the margins of one plate are, therefore, expected to have also formed major planes subdividing all overlying plates into platelets (Figure 2.15). Major joint spacing based on upward projection through the failed mass of lateral margins suggests typical size of platelets on the order of several (ca. 0.5 – 5) square kilometres. Assuming that the extent of the largest continuous sliding surface preserved within the scar provides an upper limit on the area of a single platelets, platelets would, at most, have been 29 km^2 in area.

2.5.2.3 Geomechanical model

Orientations of bedding, pre-failure slope, and lateral and crown release surfaces facilitated planar sliding (Figure 2.14). Preferentially weakened fractures facilitated major lateral release parallel to the dip direction of the slope and tectonically-sheared bedding facilitated sliding parallel to the slope. The major break-out across the Asmari Limestone carapace was required for kinematic release at the slope toe, and was likely assisted by fluvial undercutting by the Seymareh River. This combination of conditions ultimately led to massive rock slope failure.

Sliding along an overall basal failure surface of such low slope (11°) required unusually low shear strength conditions. Low rock-mass strength of units at depth, reduction to residual shear strength along sliding surfaces by tectonic shearing, decreased effective stress due to water capture in the unroofed crest of Kabir Kuh and subsequent down-slope transport in the failed mass along highly fractures limestone beds, and asymmetric loading in the central portion of the upper limit of the detachment area due to the steepening of the failure surface all contributed to this condition. Both the failure kinematics and debris morphology indicate the landslide was an instantaneous single event. Although many landslides lack proximate triggers, simultaneous failure over such an extensive area is suggestive of a major instantaneous trigger. Based on the high seismicity of the region and the temporal concentration of energy release in such events, a large earthquake probably triggered the landslide (cf. Ambraseys and Melville, 1982; Harrison and Falcon, 1938; Watson and Wright, 1969).

---

[1] The condition when a potential sliding surface at the base of a block dips and a flatter angle than the topographic slope, but with similar strike, causing the surface to be exposed on the slope surface (Wyllie and Mah., 2004; p. 38).

Morphology and extent of the source area and the low angle of failure can be explained by a geomechanical model considering the history of formation of Kabir Kuh. The geomechanical model includes two elements : the presence of bedding parallel shears prior to failure and the presence of elevated fluid pressures within the rock mass. It is suggested that both these elements played a direct role in failure. Broad correspondence of sliding surfaces with lithologic boundaries within the stratigraphic sequence and distribution between geomechanical units can be related to the structure and composition of Kabir Kuh. Fluid pressures in bedded sequences are greatest at lithologic boundaries due to permeability contrasts (Hodge and Freeze, 1977). In Kabir Kuh, fulid pressures would have been greatest at lithologic boundaries between highly fractured limestones and relatively unfractured impermeable shales, which characterize the failed sequence. During formation of Kabir Kuh by folding, elevated pore pressures at these boundaries decreased effective stress, defining planes of preferentially reduced shear strength. The shearing required to accommodate folding was focused along a select number of these planes at a spacing influenced by fold geometry, as is suggested by relations between fold geometry and shear surface spacing (Donath and Parker, 1964; Price and Cosgrove, 1990, p. 367). Shearing along these planes reduced their shear strength to residual values. Subsequently, low angle gravitational sliding was accommodated by exceptionally weak bedding-parallel pre-sheared surfaces. Although bedding-parallel shear is most common at lithologic boundaries and in low strength units, it also occasionally occurs within homogeneous limestone units (e.g. sliding surface 1, Figure 2.9) in the Zagros fold-thrust belt (Stephenson et al., 2007).

High permeability of fractured limestones in the region is demonstrated by dam foundation leakage (Ghobadi et al., 2005) and high productivity of oil reservoirs (McQuillan, 1985). Breaching of Kabir Kuh exposed limestone beds including the Asmari Formation, minor limestone interbeds of the Pabdeh Formation and limestone members of the Pabdeh and Gurpi Formations (Figure 2.4). Infiltration along the upslope scarp forming the northeast ridge of Kabir Kuh flowed down-slope through fractured limestone beds. Where overlying aquitards were present (e.g. shale interbeds of the Pabdeh Formation or shale members of the Pabdeh and Gurpi Formations), hydraulic pressures greatly increased down-slope within and at the base of the yet-to-fail mass. Similar aquifer recharge is demonstrated by many anticlines throughout the Zagros orogen, including the Ravandi anticline, adjacent to Kabir Kuh (Ashjari and Raeisi, 2006). Presence of contemporary springs within the scar indicate the presence of at least near surface aquifers in the northeast flank of Kabir Kuh.

Thus, in Kabir Kuh, lithologic boundaries result in permeability contrast that influenced creation of sliding surfaces first by producing bedding-parallel shear surfaces that defined planes favouring sliding and second by elevated fluid pressures along these pre-sheared surfaces prior to failure. Although

bedding-parallel shearing and elevated pore pressures were not directly observed, assumption of their occurrence is reasonable based on direct field observations and reconstruction of the failed mass through field investigation and analysis of remote datasets.

Contributions to the overall failed mass were unequally distributed between geomechanical units (Figure 2.9) and between plates (Figure 2.15). The Asmari Limestone constitutes over half (20.7 Gm^3) of the volume of the entire failed mass. The uppermost plate, which included the Asmari Limestone unit and the upper half of the Pabdeh Limestone unit, made up over 60 percent (23 Gm^3) of the landslide.

The presence of multiple stacked, parallel, persistent sliding surfaces indicates that initial transport involved composite superimposed displacements resembling sliding of an inclined deck of cards. Displacement of individual plates relative to Kabir Kuh increased incrementally upward through the failed sequence due to the cumulative effects of sliding on multiple stacked surfaces. Because failure was instantaneous and presumably simultaneous along the sliding surfaces, acceleration and velocity of the plates similarly increased upward due to their upward-increasing cumulative displacement. Consequently, stratigraphically higher blocks would have over-run those below and travelled a greater distance. Asmari Limestone in the only lithology in at least the most distal two third of the debris, but is completely lacking in the most proximal debris, indicating that the uppermost, passive plate was in fact displaced the farthest.

The great mass and acceleration of the thick passive Asmari Limestone sequence also begins to explain the high mobility of the landslide. Mechanical preservation of very large and angular blocks of Asmari Limestone across the surface of the debris sheet , particularly in the distal part, suggests rafting (Harrison and Falcon, 1938), probably on disintegrated underlying plates, during failure and transport.

Debris run-up over the plunging nose of a plunging anticline (Figure 2.5b) provides a minimum constraint on rock avalanche velocity. Assuming complete conversion of kinetic energy to potential energy, the relation between velocity, V, and height of debris run-up, h, over a barrier transverse to flow is expressed by the simple energy head formula:

$V = (2gh)1/2$ (Equation 1)

where g is gravitational acceleration. To surmount the ca. 500 m high portion of the anticline nose, the rock avalanche would have had a minimum velocity of ca. 100 m/s at the instant it encountered the topographic barrier. This estimate is, however, conservative as at least some portion of the kinetic energy was converted to forms other than potential during run-up. The barrier is over 6 km from the toe of the source slope, and velocity would have decreased over this distance due to frictional influences of the

22

valley bottom and internal friction within the debris. Consequently, the rock avalanche would have had a much greater velocity prior to encountering the barrier.

In addition to stacked sliding, lateral, and to a lesser degree, bedding-normal movements occurred within the failed mass during initial transport. Mobility of individual plates was enhanced by the presence of major joint sets that subdivided them into platelets more capable of sliding around (laterally) or over (bedding-normal) topographic barriers provided by rock that remained attached to Kabir Kuh and was either of the same stratigraphic level or was stratigraphically higher. Consider, for example, plate 4 (Figure 2.15). Its failure as a single intact plate is not kinematically possible because of down-slope barriers. The triangular portion of the plate closest to the left lateral margin (northwest) was most likely separated from the rest of the plate by a down-slope-dipping joint at its narrowest point. Subdivision of the remainder of the plate into platelets of varying size similarly would have improved mobility past down-slope barriers. The only plate with the kinematic freedom to fail as a single undivided mass was plate 1, the uppermost and passive plate, as down-slope topographic barriers were relatively absent; in addition to the major break-out at the slope toe, only an additional break-through of short extent (~1 km) part way up the slope near the left lateral margin was required.

2.6 Discussion

2.6.1 Metrics and mobility

With reference to published data on other gigantic sub-aerial landslides, the newly reported volume for the Seymareh rock avalanche (38 Gm^3) is exceeded only by the Baga Bogd rockslide, Mongolia (Philip and Ritz, 1999), which has a reported volume of 50 Gm^3. Reanalysis of the Baga Bogd landslide in this work, however, suggests that its volume was overvalued due to an overestimation of the debris area (Philip and Ritz, 1999) (300 km^2). A more accurate debris area determined in this study from Landsat ETM+ imagery is 180 km^2. Given the maximum reported thickness (Philip and Ritz, 1999) for the debris (200 m), the volume of the Baga Bogd rockslide cannot, therefore, exceed 37 Gm^3, and is probably much lower. The Seymareh landslide is, therefore, the largest known rock avalanche on earth and potentially the largest sub-aerial landslide of any type. The volume of the Seymareh rock avalanche approaches those of gigantic landslides on Mars (Quantin et al., 2004).

2.6.1.1 Denudation and Energy release

Because the Seymareh rock avalanche is one of the largest known sub-aerial landslides in the world, erosion rates resulting from the instantaneous denudation implied in its occurrence are unprecedented on the Earth's continental landmass. Given estimates of sediment fluxes for the global continental landmass

(14 Gt/a) (Syvitski et al., 2005) and for an arid mountainous area such as the Zagros Mountains (~0.1 Gt/a) (Einsele, 2000), the roughly 110 Gt Seymareh rock avalanche achieved the equivalent of 7.8 years of global- and 1,500 years of range-scale mechanical denudation. Contemporary sediment fluxes of the Seymareh and Kashgan basins upstream of rock avalanche are 0.0056 Gt/a and 0.0046 Gt/a, respectively (Iran Water and Resources Power Development Company, unpublished data). The Seymareh rock avalanche thus represents roughly 11,000 years of basin-scale mechanical denudation. Although materials involved in the failure were transported a short distance relative to typical fluvial denudation, the landslide further contributed to erosion on much longer time scales. Exposure of soft lithologies within Kabir Kuh and mechanical weathering of debris during transport drastically increased susceptibility of both materials to subsequent erosion.

Due to its large height of fall and massive volume, the energy released by the Seymareh rock avalanche was extremely large. Energy release of mass movements can be determined from the gravitational potential energy equation:

$$U_g = mgh \hspace{4cm} \text{(Equation 2)}$$

where m is mass, g is acceleration due to gravity, and h is the height of fall of the centre of mass. Given an estimated ca. 900 m fall of the centre of gravity of the 38 Gm^3 mass of and an approximate density of 2720 kg/m^3, energy release during this single event is on the order of 10^{18}J. Thus, energy released by the Seymareh rock avalanche is equivalent to the energy released by the M9.0 2004 Great Sumatra Earthquake (1.1 x 10^{18} J; Lay et al., 2005) and the 1883 eruption of Krakatoa (8.4 x 10^{17} J; Choi et al., 2003).

2.6.2 Age / timing

It is suggested that the age of the charcoal sample is fairly close to that of the landslide. The course texture (> 1 mm) of the dated fragments suggests they were transported a relatively short distance prior to deposition. Formation of the charcoal, therefore, likely only slightly predates its deposition. The sediment volume below the stratigraphic position of the dated charcoal is estimated as roughly 110 m^3 and the modern sediment load (Iran Water and Resources Power Development Company, unpublished data) of the Seymareh River is 5.64 Mt/a ($\sim$ 2.6 x10^6 m^3/a). Based on the assumption that sedimentation began immediately after impoundment by the rock avalanche debris, and that sediment loads during early infilling of the lake are broadly similar to those of today, the charcoal was deposited a few 10's, and certainly not more than a few 100's of years after the landslide. This result indicates that the Seymareh landslide occurred ca. 9,000 years B.P., i.e., in the early Holocene.

Because the sample is terrigenous, contamination by older carbon groundwater flowing through carbonate bedrock and dilution of the ^{12}C:^{14}C ratio (the hard-water effect) could not have occurred. Removal of roots and mineral sediment (silt and sand) prior to dating reduces the potential for contamination of the charcoal sample. Younger humic acid may, however, havebeen introduced by infiltration from the present terrace surface ~ 5 m above the sample location.

The date suggests a much younger age for the occurrence of the rock avalanche than a previously reported radiocarbon age for a bulk sample of peaty layer from the base of a sediment core taken from lake on the debris (10,370 ± 120 years B.P.; Y-1759) (Watson and Wright, 1969). Due to the hard-water effect, the age reported for the sediments is considered to be overestimated by an unknown amount (Stevens et al., 2006). Further, the date may underestimate the age of the landslide by an unknown amount; the lake is in a graben that was inferred by Watson and Wright (1969) to post date the landslide by a 'short', but unknown period.

The dated charcoal has lower likelihood of contamination and more certain time relation to the landslide than does the sediment bulk sample dated by Watson and Wright (1969). The date presented here, therefore, provides more reliable age constraint on the landslide than that previously reported.

2.6.3 Implications for gigantic landslide occurrence

2.6.3.1 Commonalities of gigantic landslides on continental surfaces

Globally, the majority of known gigantic landslides are rockslides or rock avalanches evolving from rockslides. Understanding of detachment and initial transport is particularly important because these influence the size and timing of gigantic rockslides and rock avalanches and influence debris transport, and subsequent debris emplacement. Consequently, understanding of detachment and initial transport of gigantic landslides initiating as rockslides, such as the Seymareh rock avalanche, has the potential to greatly increase knowledge about gigantic landslides.

General conditions that combined to cause detachment and initial transport of the Seymareh rock avalanche have also been reported for other gigantic landslides around the world. Most gigantic rockslides initiated by planar (Baga Bogd; Flims [Deplazes et al., 2007]) or asymmetrical wedge (Green Lake, Waikareti [Hancox and Perrin, 1994]) failure. In the latter case, the steeper plane of the wedge failure can be considered to act more as a lateral release (cf. Beetham et al., 2002). Such bias in failure mechanism can be explained by the scale of the landslide relative to the landscape. Relief within mountainous terrain has physical limits (Schmidt and Montgomery, 1995). Since rocksliding requires an included sliding surface, albeit potentially of very low angle for gigantic landslides (cf. Beetham et al.,

2002; Philip and Ritz, 1999), and kinematic freedom at the slope toe, relief subsequently constrains potential detachment thickness. To achieve the volume of gigantic landslides, large along-slope failure dimensions are required. Given this requirement and limits on thickness, wedge geometry would either have to be very wide-angled or more closely resemble planar failure with an inclined lateral release surface, to achieve large volume failures.

Nearly all occur in sedimentary (clastic and carbonate) (Baga Bogd, Waikareiti, Flims, Beshkiol [Strom and Korup, 2006]) or, to a lesser degree, metamorphic lithologies (Green Lake, Langtan [Heuberger et al., 1984]) indicating the importance of the presence of large scale extensive anisotropies within the rock mass in defining gigantic landslide masses and controlling their detachment. In all cases, multiple sets of cross-cutting large scale discontinuities are required. Additionally, rock-mass heterogeneity over the scale of the entire failed mass is important. Presence of very resistant material over very soft ones (e.g. Seymareh and Baga Bogd) have potential to enhance the volume of a catastrophic failure as lower units decrease stability of the overall mass and increase the potential depth of failure while upper units, typically passively involved in failure, load the lower and protect them from slower long-term denudation by more typical erosional processes.

2.7 Conclusions

Revised metrics of the Seymareh rock avalanche indicate that many previously determined metrics, especially the more complex metrics such as volume, were inaccurate. Failure and initial transport of the Seymareh rock avalanche are explained by a geomechanical model involving bedding-parallel shear, preferentially weakened joint orientations, local break-through between bedding at different stratigraphic levels and a major break-out through the Asmari Limestone carapace at the toe of the slope. Location of bedding-parallel slip was determined by lithologic variation and folding of the Kabir Kuh anticline. Preferential joint weakening resulted from local stress due to the formation of Kabir Kuh and from far field stress influenced by reactivation of basement faults from a previous tectonic episode.

The immense volume of the detached rock mass at Seymareh resulted from 1) the high degree of lateral continuity of bedding planes that exhibited uniform orientation over ca. 100 km^2 ; 2) marked downward weakening in the rock mass sequence, since without weaker layers at depth, failure would not have penetrated as deeply into Kabir Kuh; 3) the presence of multiple weakened bedding surfaces resulting from folding-induced bedding plane slip and 4) the presence of a resistant carapace of highly resistant Asmari Limestone without which the weaker materials would have gradually been denuded by slope erosion processes. Together these conditions ultimately lead to a landslide record-breaking size.

The resulting energy release of the Seymareh rock avalanche is comparable to that of some of the largest historical cataclysmic catastrophic geophysical events. Initial failure involved nine stacked plates separated by bedding-parallel shears and each laterally divided into platelets by pervasive bedding-normal joints. Structures involved in the geomechanical model favoured detachment and transport of such a large mass because of their low shear strength and, in particular, the high degree of structural continuity within Kabir Kuh.

The age of the Seymareh rock avalanche is on the order of 1,500 radiocarbon years younger than previously reported. Coupled with the dramatic upward revision of the volume of the rock avalanche, this new age has important implications for the global magnitude-frequency relationships of gigantic landslides.

Figure 2.1: Panorama of the Seymareh rock avalanche including the source area central portion of the debris sheet.

The scar is over 15 km wid. The visible debris is composed entirely of angular limestone ranging from fines up to house-sized boulders. Low flat surfaces of small lake deposits, such as that in the middle foreground, are common on the debris sheet. Utility poles on the debris in the foreground are ca. 12 m high. The vantage point is the debris limit on the southwest flank of the plunging anticline ~15 km from the central part of the crest of the scar (see Figure 2.5).
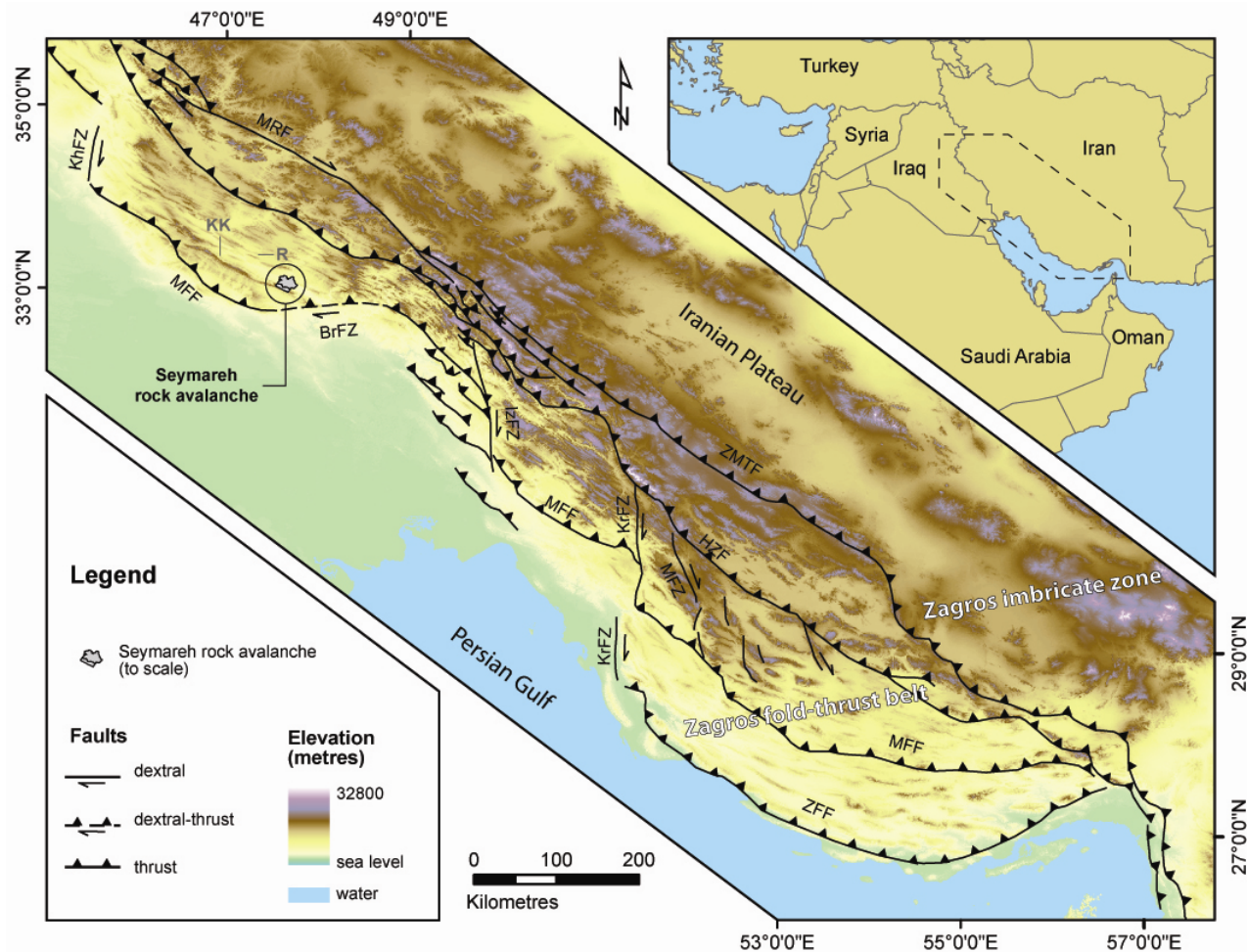
Figure 2.2: Tectonic and physiographic setting of the Zagros Orogeny.

Tectonic features after Blanc et al. (2003) and Sepehr and Cosgrove (2004). Fault abbreviations: BrFZ, Bala Rud Fault Zone; HZF, High Zagros Fault; HZF, High Zagros Fault; IzFZ, Izeh Fault Zone; KhFZ, Khanaqin Fault Zone; KrFZ, Kazerun Fault Zone; MFF, Mountain Front Fault; MFZ, Mengarak Fault Zone; MRF, Main Recent Fault; ZFF, Zagros Frontal Fault; ZMFT, Zagros Main Thrust Fault. Elevations from GTOP30 DEM. Anticlines mentioned in text are Kabir Kuh (KK) and Ravandi (R). Note that the gross morphology of the Seymareh rock avalanche is visible even when the study area is viewed at belt-scale.
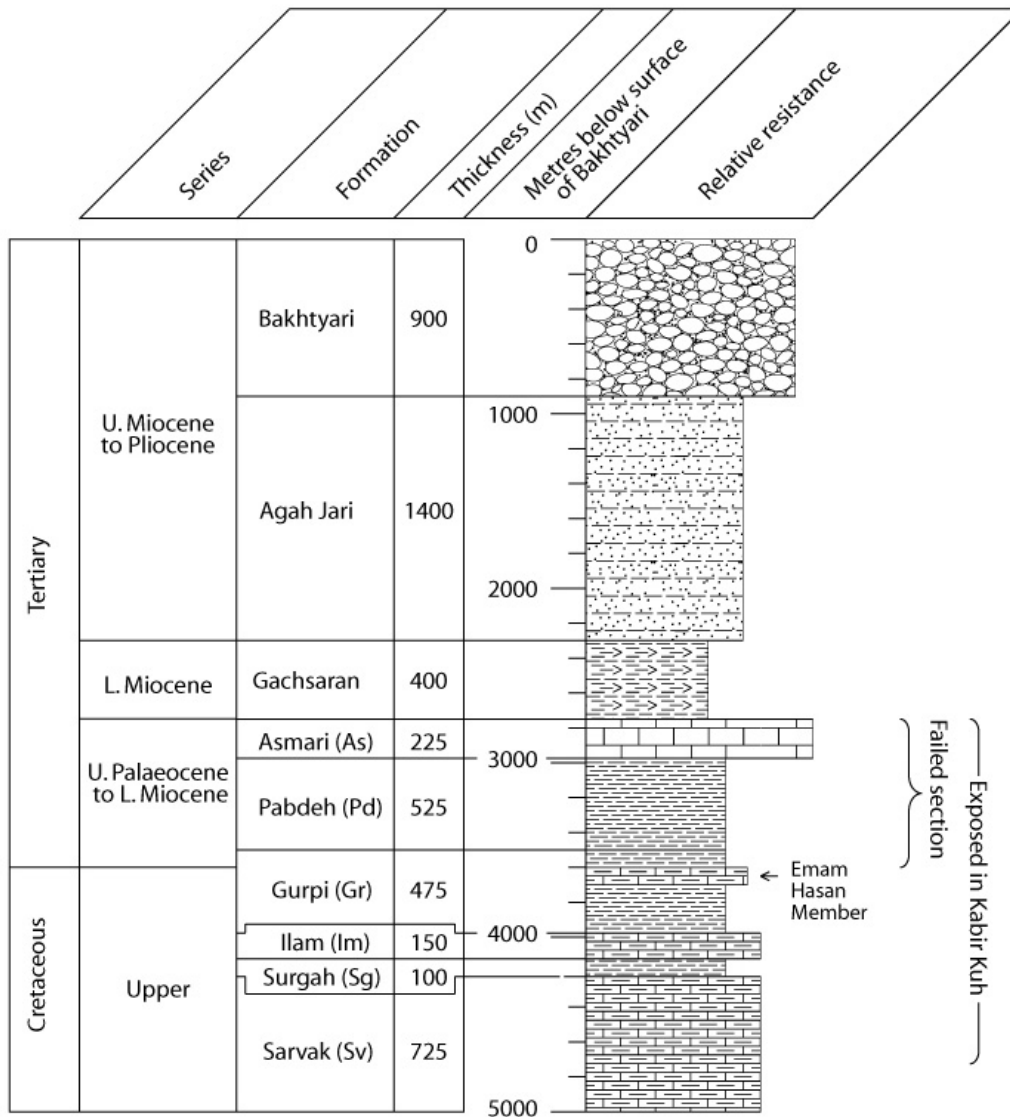
Figure 2.3: Regional stratigraphy of the Lorestan area (Lorestan and Ilam provinces).
Formations, ages, thicknesses and lithologies are based on James and Wynd, 1965.
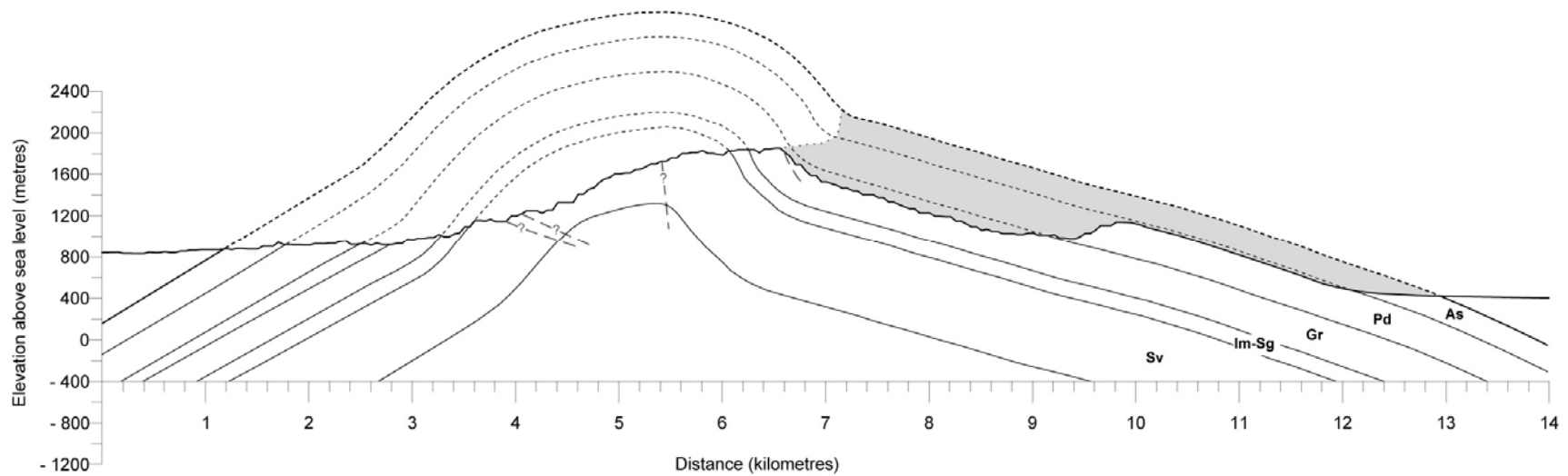
Figure 2.4: Profile across Kabir Kuh at approximately the central portion of the source area of the Seymareh rock avalanche with superimposed structure and stratigraphy.

Present topographic surface (solid black line) is derived from an SRTM DEM and represents a combination of long-term erosion and failure of the Seymareh rock avalanche (shaded grey). Boundaries between geologic formations are shown where they existed prior to erosion (dotted lines) and where they now exist within un-eroded portions of the anticline (solid lines). The upper boundary of the Asmari Formation represents the pre-erosion surface of Kabir Kuh. Known and uncertain (?) faults are shown as grey dashed lines. Stratigraphy and faults are derived from field mapping and after Setudehnia and Perry (1967a), Macleod (1970), Takin et al. (1970) and Blanc et al. (2003). Formations are defined in Figure 2.3 (As, Asmari; Pd, Pabdeh;, Gr, Gurpi; Im, Ilam; Sg,, Surgah; Sv, Sarvak)
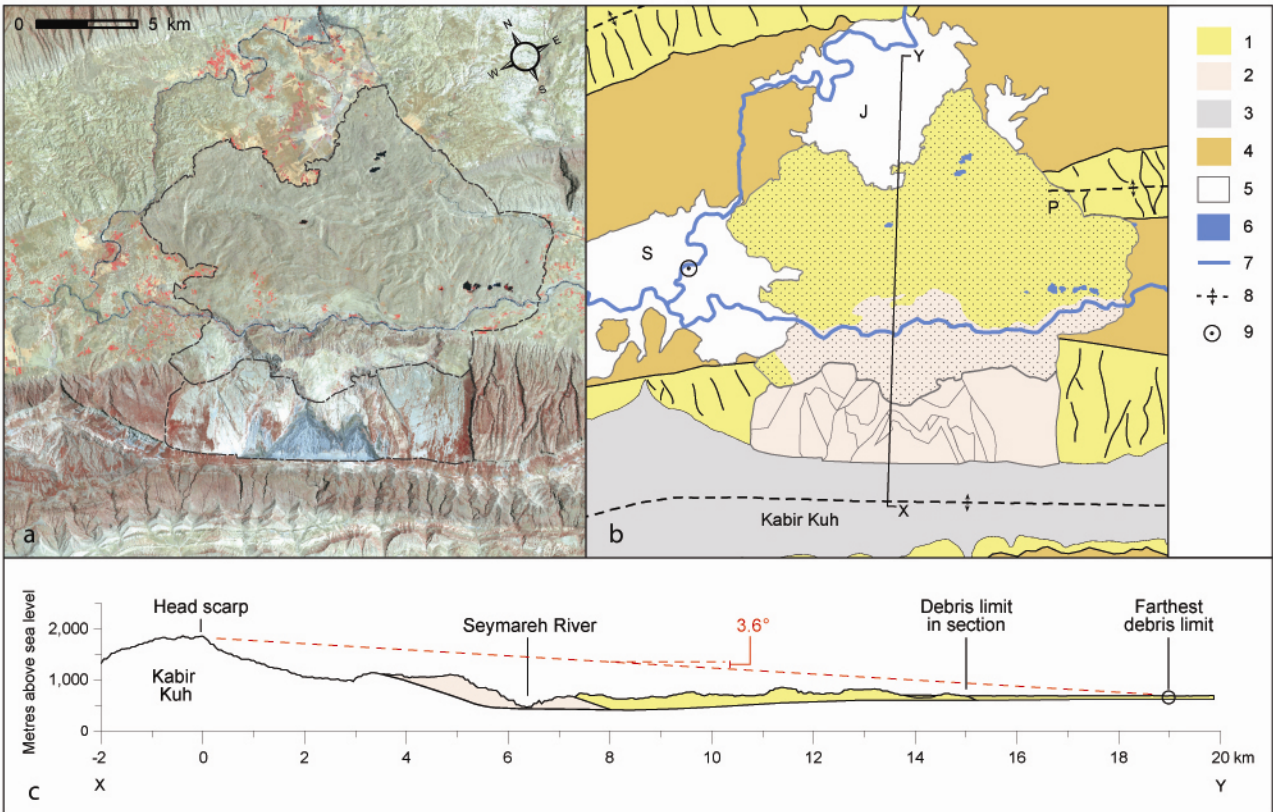
Figure 2.5: Overview of the Seymareh rock avalanche.

a. Near infrared false colour composite of 30m Landsat ETM+ imagery showing extent of the Seymareh landslide and associated landslide-dammed lake deposits. The landslide scar and debris are outlined; b. Thematic map of the landslide scar, debris and immediately surrounding terrain based on interpretation of Landsat imagery in a, augmented by interpretation of 5 m multispectral SPOT imagery, interpretation of small-scale panchromatic aerial photographs and field observations. Legend: 1 – Asmari Limestone (carapace, solid; debris, stippled); 2 - Pabdeh and Gurpi Formations (source area, solid; debris, stippled); 3 – breached anticline (mostly Ilam and older formations); 4 – valley bottom; 5 – lake deposits (Seymareh, S; Jaidar, J); 6 – existing lakes on the debris surface; 7 – river; 8 – anticline axis; 9 – location of radiocarbon sample (see Figure 2.11). Parts of the distal margins of the rock avalanche debris are buried beneath the deposits. Note that the debris overrides a plunging anticline at its eastern limit (P); c. Longitudinal profile (X-Y in b) from the head scarp, through the scar, debris and landslide-dammed lake deposits. Profile constructed from SRTM DEM and interpretations added from SPOT and Landsat imagery.

Figure 2.6: Photographic examples of debris morphology and lithology.

a. Distal debris composed of Asmari Limestone (left lateral margin and left portion of scarp are present in the distance); b. weathered surface of an Asmari Limestone block in the distal debris; c. Debris surface at the division between distal Asmari portion (left) and proximal Eocene portion (right); .d. debris surface at the division between distal (Asmari-dominated) and proximal (Eocene-dominated) debris, composed of dispersed large blocks of limestone with a finer grained mudrock matrix; e. a single large limestone block and surrounding mudrock fines from the area shown in d; f. proximal debris composed of Eocene mudrocks (note field book for scale); g. Boulder of interbedded limestone and mudrock exposed in the proximal debris.
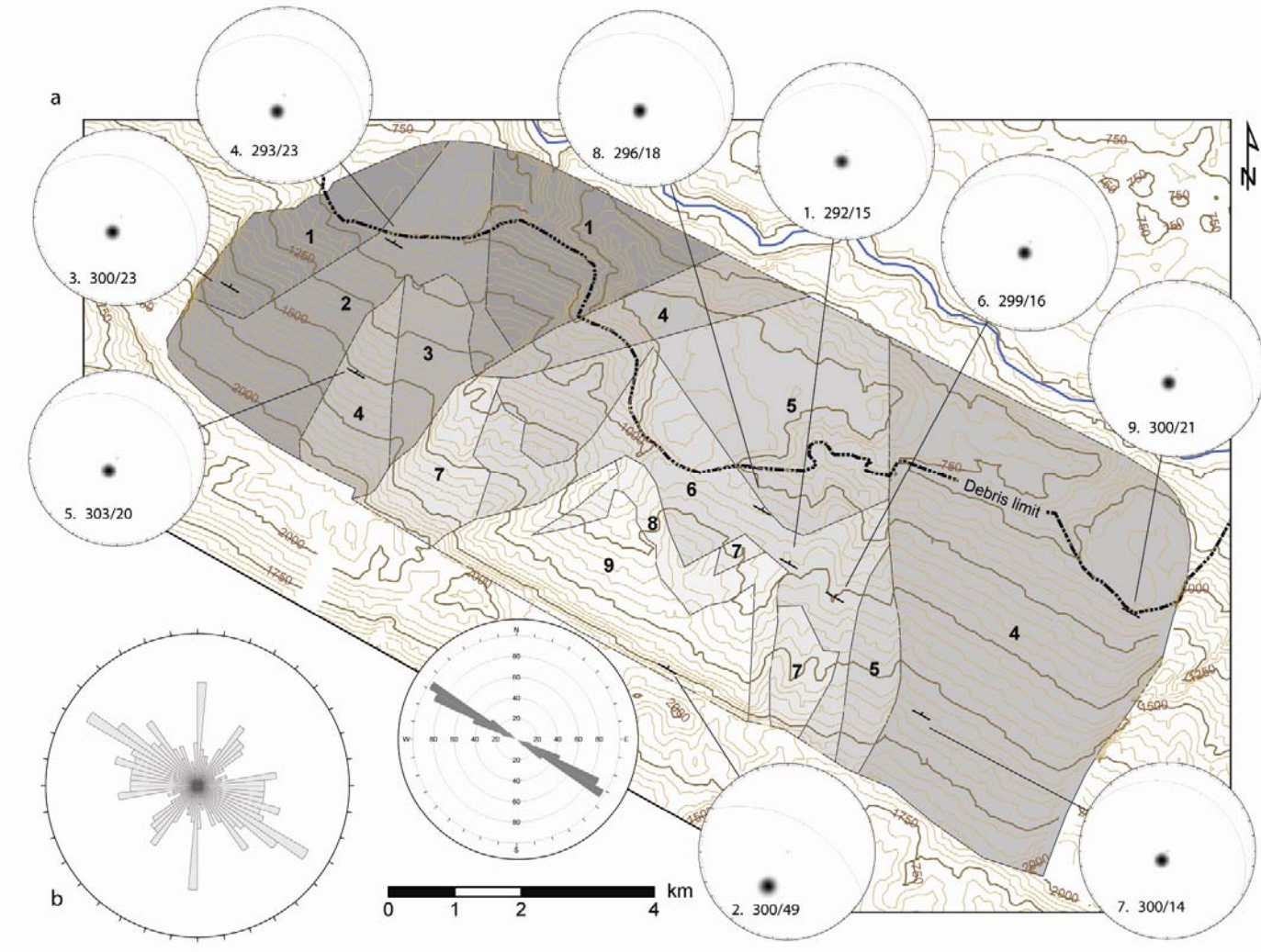
Figure 2.7: Structural map of the source area of the Seymareh rock avalanche.

a. Each structural measurement location represents 20 to 40 individual measures of bedding surfaces (Appendix C.1). The rosette plot represents bedding strike. See Figure 2.9 for stratigraphic position of numbered sliding surfaces; b. Rosette plot of apparent trends of joints visible on the Landsat image (Appendix C.2). Most linear edges of sliding surfaces represent major joints.

34

Figure 2.8: Photographic examples of source area stratigraphy and bedding surfaces.

Stratigraphic positions of photographs are showing in Figure 2.9. a. in-situ bedding surface of thin-bedded limestone below thin talus cover (note backpack in left middle ground for scale); b. weathered surface of an Asmari Limestone block in the distal debris; c. interbedded shale and limestone (note arm in left middle ground for scale); .d. bedding of intebedded shale and limestone exposed in a down-slope oriented gully; e. Mass of interbedded shale and limestone resting on sliding surface 4; f. Limestone bedding surface (sliding surface 4) with striations (note compass for scale); g. Shale of the Pabdeh Formation; h. Upper contact of the Emam Hassan Member exposed in the central head scarp.

35

Series	Formation	Photograph	Metres below surface	Relative rock mass strength	Sliding surfaces	Unit	Thickness (m)	Failed volume (Gm³ & percent)	Description
Lower Miocene	ASMARI		0–225			Asmari limestone	225	20.7	55 %	Medium- to thick-bedded limestone
Upper Palaeocene to Oligocene	PABDEH	a; b?; c; d?; e & f; g			1 (white); 2 (grey); 3 (white); 4 (grey); 5 (white); 6 (grey)	Pabdeh lmstn.	50	4.3	12 %	Asmari-type limestone with occasional thin interbeds of shale
						Interbedded Pabdeh	205	10.5	28 %	Thinly-bedded shaly limestone alternating with more thickly-bedded more competent limestone
Upper Cretaceous to Lower Palaeocene	GURPI	h			7 (white); 8 (white); 9 (grey)	Pabdeh –Gurpi shale	200	2.1	6 %	Clayey calcareous shale & marl with frequent minor interbedded clayey argillaceous limestone and two more major thin clayey limestone layers

Emam Hassan Member

Figure 2.9: Stratigraphic sequence of the rock mass that slid from the northeast flank of Kabir Kuh showing major lithologies, location of sliding surfaces, and delineation and description of four geomechanical units.

Stratigraphic divisions are from published sources (James and Wynd, 1965; Setudehnia and Perry, 1967a; Takin and Akbari, 1970). Thickness and lithological composition of divisions are based on field observations. Relative rock mass strength is based on qualitative field assessment of rock mass characteristics (Appendix D). Designation of geomechanical units is based on lithologies and field-based relative rock mass strength. Identification of sliding surfaces and positioning within the sequence is based on published geologic maps (Setudehnia and Perry, 1967a; Takin and Akbari, 1970), remotely sensed imagery, SRTM DEM and field observations. Major sliding surfaces (4 in total), identified as those contributing most to the total failure surface area represented by the scar, are designated by grey filled triangles. Minor sliding surfaces (5 in total) are designated by white triangles. Letters indicate positions of photographs from Figure 2.8.

Figure 2.10: Eroded lacustrine deposits of the ancient Seymareh Lake.

Note the high degree of accordancy of the heavily rilled lacustrine materials in the fore- and middle-ground. The slightly higher, more irregular, coarser material in the middle ground of the left two-thirds of the photograph is the northwest limit of the debris sheet. The source area is visible in the right background.
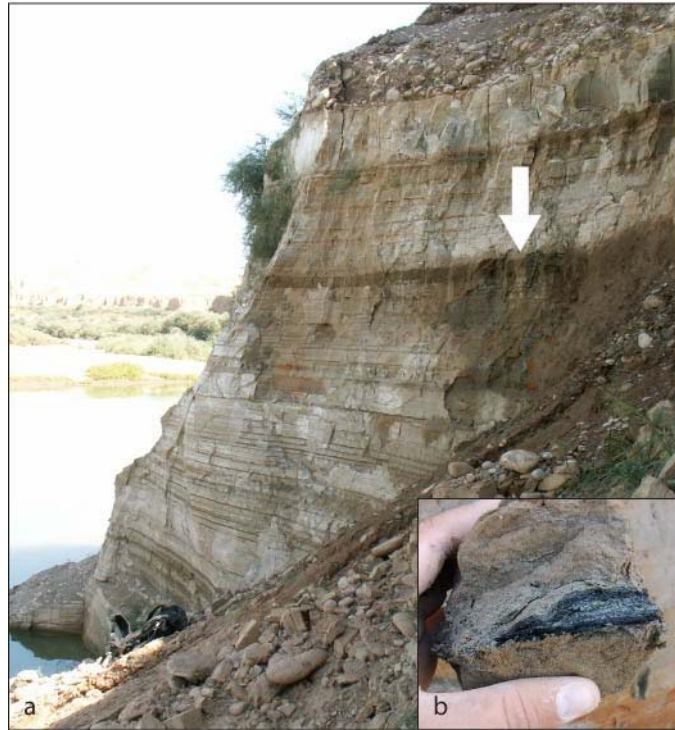
Figure 2.11: Charcoal sample from Seymareh lacustrine deposit used in radiocarbon dating.

a. Stratigraphic location of charcoal-rich horizon within a lacustrine sequence exposed in river cut of the Kashgan River (see Figure 2.5b for location). Note backpack in lower left for scale. Total height of sequence from river level to bottom of gravel unit ~5m. Charcoal-rich layer is ~3.5 m above river level. Sample is estimated to be 15 m above the base of the lacustrine sequence. b. Detrital charcoal sample used in radiocarbon dating.

Figure 2.12: Stacked sliding surfaces in the source area of the Seymareh rock avalanche viewed from the proximal debris limit.

Multiple sliding surface levels are visible. Surfaces are parallel to bedding (outcropping in lateral scarp in the left foreground). Debris in the right fore- to middle-ground is composed completely of Eocene mudrocks. The view is toward the left lateral margin (middle background).
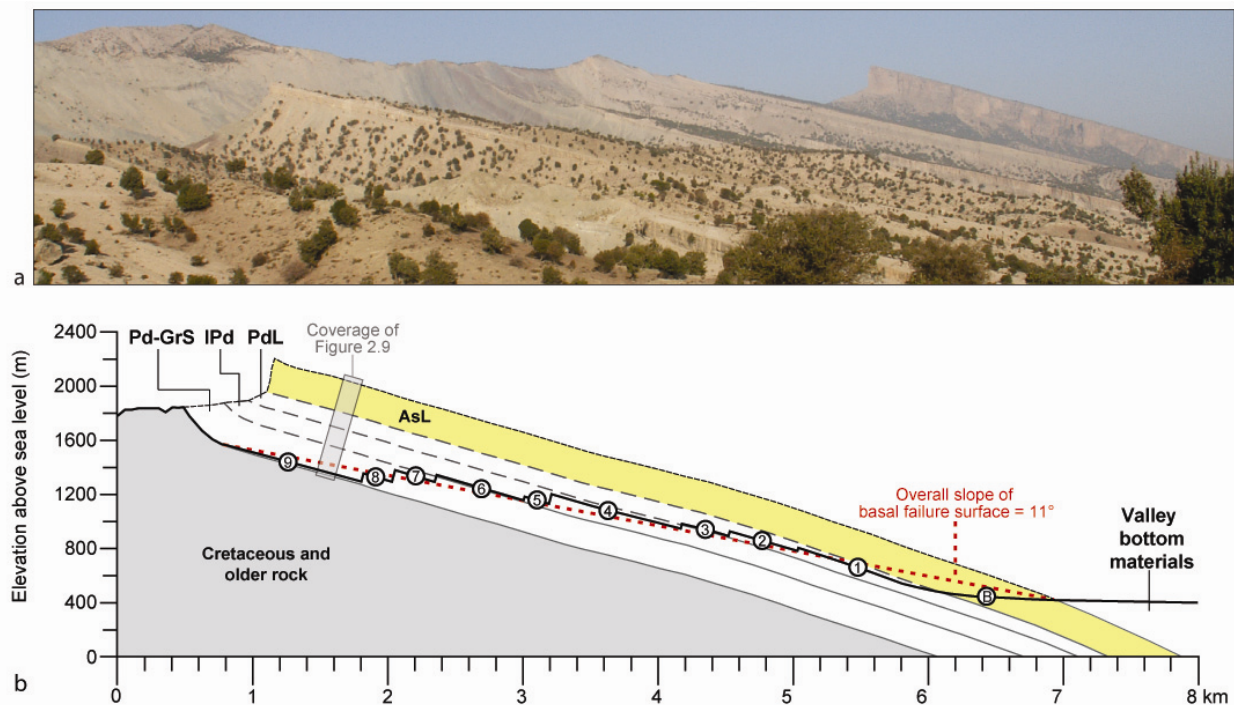
Figure 2.13: Multiple sliding surfaces forming the complex basal failure surface of the Seymareh landslide.

a. Left lateral margin of the scar viewed from proximal limit of the debris in the middle of the scar. The distant right skyline consists of Asmari Limestone above sliding surface 1. The steep scarp on the right skyline indicates the high resistance and high rock mass strength of the Asmari unit. Sliding surfaces below the Asmari are visible between the right skyline and the camera position. From farthest and highest to closest and lowest, they are surfaces 1 to 6 (see Figures 2.7 and 2.9 for location in stratigraphic sequence). b: Topographic profile showing geometry of the generalised basal failure surface, composed of nine (numbered 1 to 9) bedding-parallel sliding surfaces linked by break-through across bedding . Total failure of the rock mass was achieved by major break-out (B) through the Asmari Limestone carapace at the toe of Kabir Kuh. Elevations are from the SRTM DEM. The represented lengths of individual sliding surfaces are proportional to the contribution of each to the total area of the basal failure surface. Overall slope of the basal failure surface (11°) is less than that of individual sliding surfaces (~20º) because of stratigraphic deepening of the basal failure surface upslope. Geomechanical area units delineated and described in Figure 2.9: AsL - Asmari Limestone; PdL - Pabdeh Limestone; IPd - Interbedded Pabdeh; PdGrS - Pabdeh-Gurpi Shale.

40
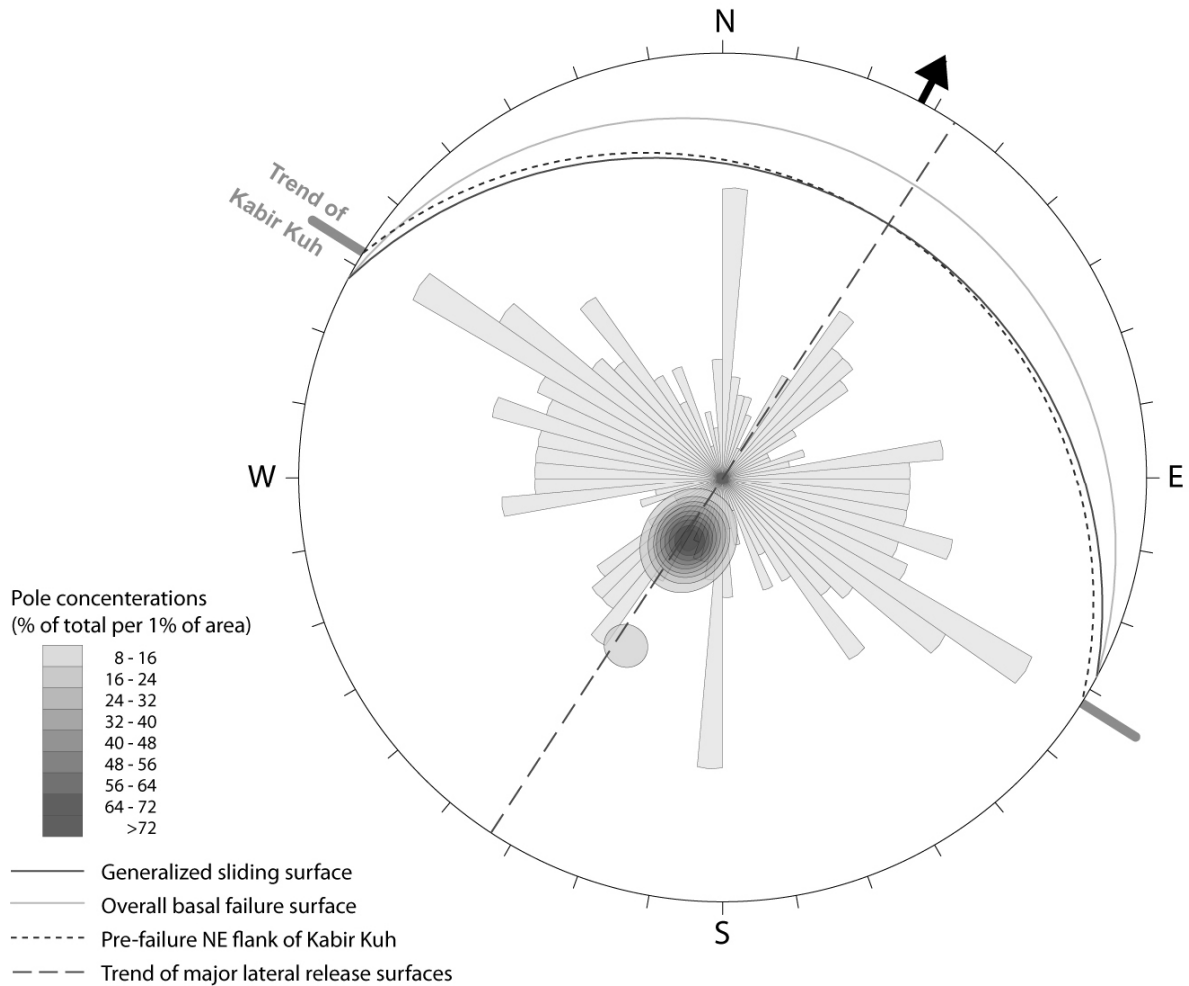
Figure 2.14: Kinematic summary of initial failure of the Seymareh rock avalanche represented on a stereonet.

The generalised sliding surface, overall basal failure surface and approximate pre-failure topographic slope are represented by great circles. Field measurements of bedding surfaces (Appendix C.1) are shown as pole concentrations. The rose diagram shows the apparent trend of joints visible on Landsate imagery (Appendix C.2. Black arrow in northeast quadrant is mean direction of initial movement. The stereonet indicates the failure mode was planar, with sliding parallel to both the bedding and topographic slope dip direction (perpendicular to the trend of Kabir Kuh).
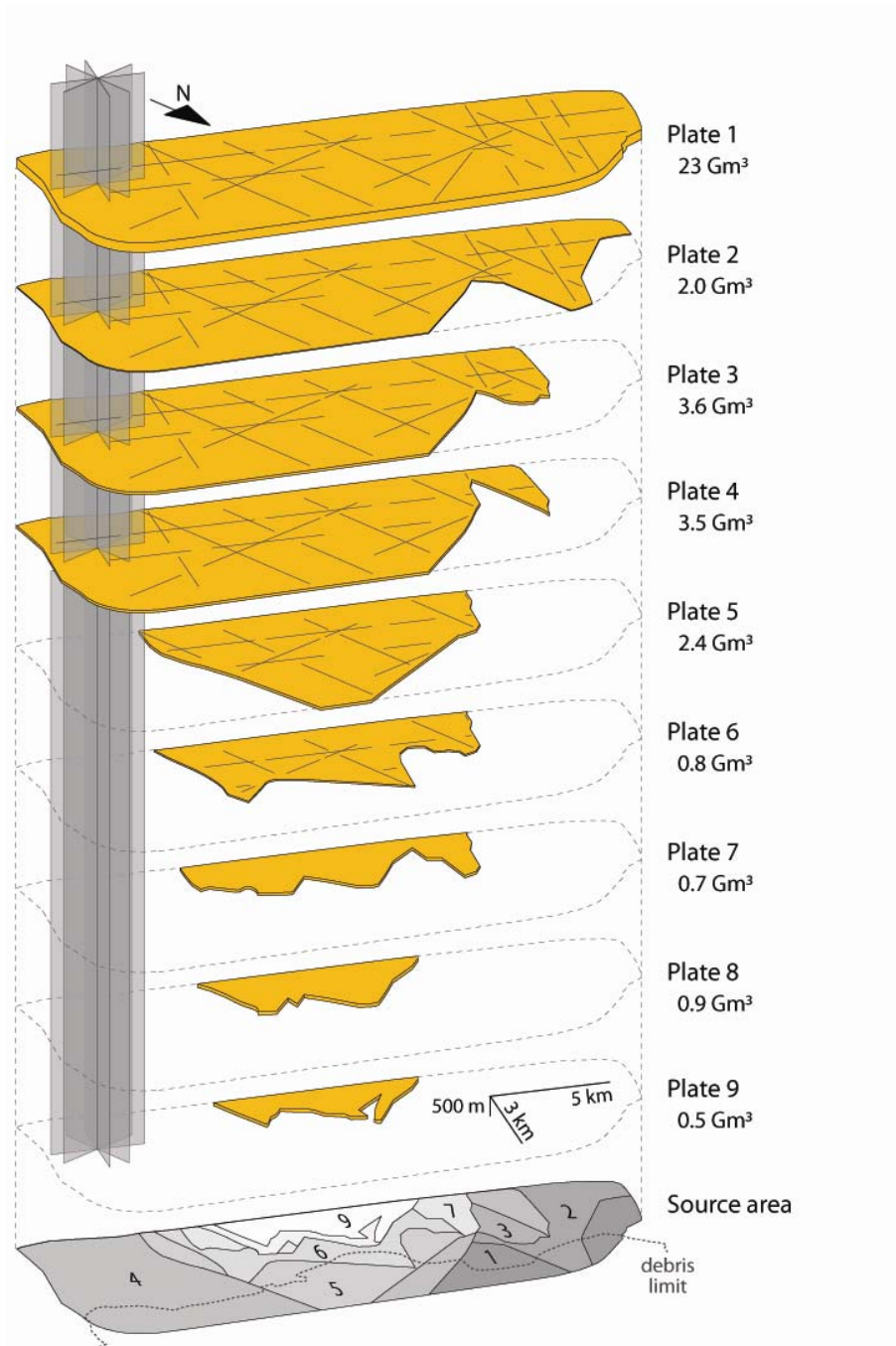
Figure 2.15: Three-dimensional exploded view of plates involved in the failure and initial transport of the Seymareh rock avalanche.

Plates are numbered from top to bottom of the failed mass. Calculated plate volumes (see Appendix B for calculation methodology) decrease overall downward. Sliding surfaces of the source area are shown at the base of the sequence of plate. Traces of major joints are based on upward projection of lateral scarps within the source area. Major joint orientations are indicated in the by the planes (grey) passing upward the plates.

Table 2.1: Summary metrics of the Seymareh rock avalanche.

Failed mass

Volume[a]		38 Gm^3
Area		100 km^2
Maximum width (across slope)		15.5 km
Length (down slope)		6.1 km
Depth:	minimum	250 m
	maximum	680 m
	mean[b]	380 m
Maximum elevation		2130 m
Central headscarp elevation		1900 m

Structure

Mean bedding dip		22 °
Mean bedding dip (without headscarp)		19 °
Maximum bedding dip		49 °
Overall basal failure plan slope (estimated)		11 °
Mean strike (without headscarp)		298 °
Mean bedding strike		300 °
Flank	strike	308 °
	dip	20 °
Right flank	strike	302 °
	dip	16 °
Left flank	strike	316 °
	dip	29 °

Debris

Volume (bulked)[a]		44 Gm^3
Volume (with out bulking)[c]		37 Gm^3
Area		196 km^2
Maximum width transverse to runout)		20.7 km
Maximum length (parallel to runout)		16.1 km
Depth:	maximum	300 m
	mean[b]	220 m
Distal elevation		690 m

Mobility proxies

Runout (failure plan toe to distal debris)	12.9 km
Runout (headscarp to distal debris) (L)	19.0 km
Height of fall (headscarp to distal debris)	1210 m
H/L	0.064
Fahrböschung	3.6 °

[a] independently estimated
[b] area-weighted
[c] assuming 20% bulking

Chapter 3

The Valley of the Rocks rock avalanche, British Columbia; the largest non-volcanic rock avalanche in the North American Cordillera

3.1 Introduction

3.1.1 Landslides in the Canadian Foreland Belt

Mountain slopes in the Canadian Foreland Belt (the Mackenzie Mountains and Canadian Rocky Mountains) are commonly subject to mass movements that are in turn controlled by rock mass properties. Reviews of landslides within the Rocky Mountains (Cruden, 1976; Cruden, 1985) and Mackenzie Mountains (Eisbacher, 1979) demonstrate that the majority of large rock slope failures are dip-slope failures involving cliff-forming Paleozoic carbonate sequences. The volume of these is mostly a function cohesion per unit area of the sliding surface and dip orientation of discontinues (Cruden, 1976). Toppling on anaclinal slopes in hard rock sequences is also common in the Rockies (Cruden, 1985), but produces much smaller mass movements.

The best known landslide in the Canadian Foreland Belt is the Frank Slide (30×10^6 m^3), which failed along a series of linked structures including joints, bedding and a minor thrust fault (Benko and Stead, 1998). Numerous larger landslides exist in the Belt, but are lesser known because they are prehistoric and, therefore, predate major settlement in the region. The largest landslides in the belt are dip-slope rockslides of carbonate rocks. They include the landslides at Rockslide Pass (0.37 Gm^3) (McLellan and Kaiser, 1984) and Avalanche Lake (0.2 Gm^3) (Evans et al., 1994) in the Mackenzie Mountains; Maligne Lake (ca. 0.5 Gm^3) (Cruden, 1976) and Medicine Lake (86×10^6 m^3) (Cruden, 1976) in the Rocky Mountains. Both the Rockslide Pass and Avalanche Lake rockslides progressed into rock avalanches. Numerous other planar cataclinal rockslides $> 5 \times 10^6$ m^3 have been documented in the southern Canadian Rockies, predominantly in Paleozoic carbonate sequences (Cruden, 1976). Significant antiquity of nearly all of the large dip-slope failures is likely explained by an exhaustive model for temporal distribution of failures, having been initiated following destabilization of many mountain slopes during glaciation (Cruden and Hu, 1993). Very few rockslides and rock avalanches in the Foreland Belt are, however, specifically age dated (Evans et al. 1994).

3.1.2 Valley of the Rocks rock avalanche

The largest non-volcanic rock avalanche known in the North America Cordillera is the Valley of the Rocks rock avalanche, in the Front Range of the Rocky Mountains (Evans, 2001) (50° 59' N 115° 38' W; Figure 3.1). The landslide is located in Mount Assiniboine Provincial Park, British Columbia, 35 km west of Canmore, Alberta. It occurred as a remarkable dip-slope failure involving a ridge line along the Continental Divide.

   Despite its importance in the North American context, and its potential for adding to global knowledge of gigantic landslides, the Valley of the Rocks rock avalanche has received little attention. Duffy (1967) first identified the landslide in a brief , largely qualitative, account. It was later noted in reconnaissance bedrock mapping of the western half of the Kananaskis Lake sheet (82JW (Leech, 1979)) and briefly described in a reconnaissance study by Evans (1992). Consequently, even basic information about the rock avalanche, including its precise dimensions, volume and age, is unknown.

   We present the first detailed investigation of the Valley of the Rocks rock avalanche based on a combination of field investigation and analysis of remotely sensed data. A documentation of the landslide is presented including geomorphic description and interpretation, comprehensive determination of metrics, constraint of its age, and characterization of pre-conditions of and mechanisms involved in failure, transport and emplacement. Through these contributions, the present work adds to knowledge about rock mass movements in the Foreland Belt of the Canadian Cordillera and to the global understanding of gigantic landslides.

3.2 Study area

3.2.1 Front Range of the Canadian Rocky Mountains

3.2.1.1 Geology and tectonics

The Canadian Rocky Mountains are predominantly sedimentary rock (90% of outcropping area) of Palaeocene to Pre-Cambrian age and have undergone approximately 150 km of shortening and 8 km of thickening to form a northeast tapering wedge (Wheeler et al., 1974). Shortening occurred between the Middle Jurassic to Eocene (Wheeler et al., 1974) driven by subduction at the western margin of the North American plate. The Front Range is the western most part of the belt and is composed of alternating ridge-forming carbonate units and valley-forming shale units. In both units bedding forms pervasive discontinuities dipping generally between ca. 25 and 35° to the southwest.

Geologic mapping in the vicinity of Valley of the Rocks shows the presence of a complex series of westward dipping thrust sheets involving Precambrian to Mississippian units (Leech, 1979). The Devonian Palliser Formation forms major ridges within this complex, including the source ridge of the Valley of the Rocks rock avalanche (Leech, 1979). The Palliser is unconformably overlain by fine-grained clastics of the Banff and Exshaw Formations and, in the southern Canadian Rockies, conformably overlies the Sassenach Formation (Geldsetzer et al., 1986). In thrust sheets in the region near Mount Assiniboine Provincial Park, the Sassenach Formation is missing and the Palliser directly overlies the Fairholme Group (Leech, 1979).

Thickness of the Palliser varies in thickness from 200 to 320 m in the area of Banff and Jasper National Parks, increasing in thickness from east to west (McLaren, 1955), and is composed of the Morrow Member (200 m) overlain by the Costigan Member (75 m) (deWit and McLaren, 1950). In the study area, the Morrow Member is exclusively a cliff-forming grey limestone of alternating lime-grainstones forming ledges and lime-mud and lime-wackestones forming recesses (Geldsetzer et al., 1986). The less massive Costigan Member is recessive and consists ofbedded carbonates mostly composed of medium- to thin-bedded buff limestone with thin, laminar, shale-like mudstone interbeds (Geldsetzer et al., 1986) (Meijer Drees et al., 1993).

3.2.1.2 Physiography

Relief in the study area is largely inherited from pre-glacial fluvial processes (Jackson, 1980b) and is greater than that of the American Rockies because of the contrast in erosional resistance between shale and carbonate units. Typical relief in the area is of 1000 m, much lower than that elsewhere in Mount Assiniboine Provincial Park or in the Front Range. Most surfaces have been substantially modified during the Holocene by glacial and meltwater processes. Most valley bottoms are U-shaped due to glacial-widening, ridges commonly contain alpine glacial features, and valley sides and bottoms are frequently mantled by moraine (Rutter, 1972). Numerous large alpine glaciers are present elsewhere in the Front Ranges, but are largely absent in the Valley of the Rocks area.

Generally, shapes of most features in the Canadian Rockies are controlled by the structure of the predominantly sedimentary lithologies (Cruden and Hu, 1999). Within the Front Range, topography is largely determined by uniformly southwest-dipping strata producing an over-all grain that trends northwest-southeast along bedding strike. The majority of slopes are steep northeast-dipping anaclinal and gentler southwest-dipping cataclinal slopes (Cruden, 1976); oblique (bedding and topographic slope strike differ by > 20° (Cruden and Eaton, 1987)) and strike-dip slopes are relatively rare.

3.3 Methods

3.3.1 Remote sensing

Remotely sensed data were heavily used due to the large scale of the landslide. Interpretations of surface condition were based mainly on a single orthorectified Landsat ETM+ (30 m visible and near infrared multispectral; 15 m panchromatic) image and 1: 15 000 panchromatic aerial photographs. Landsat normal colour and false colour near infrared composites were pansharpened (see Appendix A for details). Elevation information was provided by Canadian Digital Elevation Data (CDED) digital elevation model (DEM) extracted from scanned 1: 50 000 National Topographic Series (NTS) maps sheets. Specifically, elevations in the vicinity of the source area and deposit were extracted from TRIM (Terrain Resource Information Management) elevation data for British Columbia. Accuracy is dependent on source data (e.g. NTS map sheet) accuracy.

Overall, remotely sensed datasets were used to interpret large scale geomorphology and physiography of the landslide and associated features prior to fieldwork. The Landsat image and DEM were used for interpretation of large scale features. Air photos provided additional detail and allowed interpretation of smaller scale features.

3.3.2 Fieldwork

Field investigation was conducted over a two week period in late July 2006. Traverses were Global Positioning Systems (GPS) controlled, allowing direct comparison of in-field observations with remote datasets and to aid correlation of field observations over the area of the landslide. Tasks during fieldwork included collection of structural data, examination of outcrop-scale geomorphic and geologic features, and ground truthing of interpretations made from remotely sensed datasets. Structural measurements were systematically collected (across and down) the sliding surface where it was exposed. Fieldwork observations and post-fieldwork reinterpretation remotely sensed data were used in combination to assess simple metrics of the landslide (e.g., debris area, scar dimensions) and to estimate volumes.

3.4 Observations and results

3.4.1 General description

3.4.1.1 Source area

The source slope is composed entirely of thick-bedded nearly massive limestone of the Devonian Palliser Formation. The scar is continuous along (down dip) and, for most of the source area, across (along strike)

slope. It is slightly concave- up in profile, (Figure 3.2) roughly 160 m deep, and is marked by steep lateral scarps oriented down-slope (Figure 3.3). Except where a ca. 90 m high head scarp remains near the left margin (Figure 3.3), the sliding surface reached the anaclinal slope along the entire width of the scar (Figure 3.4). Removal of the left flank of the ridge shifted the ridge crest and, therefore, the Continental Divide, ca. 80 m to the northeast (Figure 3.1). Brown to buff weathering Cambrian/Ordovician McKay Group shale and limestone has been thrust over grey Devonian Palliser Limestone northwest of the scar, but are lacking in the lateral scarps of the landslide, suggesting failure involved only the Palliser Formation.

   Similarity of the orientation of the sliding surface to that in regularly spaced bedding outcropping along the anaclinal slope indicates that failure was bedding parallel (Figure 3.4). Where exposed, the sliding surface is very weathered and contains frequent deeply eroded rills. A substantial amount of debris still covers the toe of the sliding surface, although talus covers much of the lower half. The lower portion of the sliding surface is vegetated by mature trees at lower elevations and by small trees and shrubs nearer the tree line (ca. 2200 m) (Figure 3.2). Locally, wide swaths of vegetation are missing or replaced by much younger vegetation (Figure 3.2), indicating recent surface failures of talus. Toward the left (southwest) portion of the sliding surface, extensive talus (derived from the left lateral scar and from upslope tower-type landforms), a lack of trees or shrubs, and presence of occasional large fragments of sun-bleached wood debris suggest more recent mobilisation (Figure 3.4).

   The left lateral scarp is nearly vertical and, although highly variable in orientation over shorter distances, overall trends down-slope. A 90 m high segment joins the main basal sliding surface to a subsidiary sliding surface, which is bounded to the southeast by a less steep lateral scarp (Figure 3.4). The surface of this lesser sliding surface is much less weathered than the rest of the scar and generally lacks rills. Caves a few to 10s of metres in dimension occur where major bedding surfaces outcrops in the left lateral scarp and castellated remnants.

   The right lateral scarp is less uniform due to irregularity of the pre-failure slope surface. A secondary ridge part way down the slope on the right flank forms a small cirque that truncates at the scar. The lateral release surface is composed of a near vertical section as well as a slightly inclined section, which are both variable in strike, but generally parallel to bedding dip direction. An elongated concave depression along the upper ca. 800 m of the base of the lateral scarp is likely a cirque (Figure 3.1).

3.4.1.2 Debris

The debris mass is not a continuous sheet , but instead is composed of two broad regions that vary in morphology and debris composition as a result of topographic influences and differences in transport

mechanism. Overall, the debris includes a large bulk (rocky debris mass) in the valley bottom directly below the scar, and a large distal lobe that reaches down valley. The major division between the two regions of debris is a steep (70 m high, 500 m wide) arcuate scarp along the northwest edge of the rocky debris mass. Both debris regions contain large deep often flat-bottomed depressions, as noted by Duffy (1967).

From its proximal limit on the lower part of scar, the surface of the main debris mass follows the sloping form of the sliding surface and then rises almost immediately to form hummocky mounds, beyond which the debris climbs sharply to form several prominent mounds that extend far up the opposite valley side. The large mounds attain elevations of 2200 to 2300 m and are concentrated in the southeast half of the rocky debris mass. Maximum relief across the rocky debris mass is ca. 280 m. The mass of debris is composed completely of jagged pieces of grey weathered Palliser limestone ranging from fines to large boulders 10s of metres in length and width. Blocks in the debris are commonly fractured, but remain intact in place.

The distal lobe extends ca. 5.5 km from the arcuate scarp. Its width transverse to the trend of the valley (ca. 1 km) is variable, generally narrowing down valley, and substantially less that that of the rocky debris mass (2.2 km). The surface of the distal lobe is hummocky, although the size, relief, and distinctiveness of hummocks decreases down valley. A few small depressions contain marshes. The lobe terminates in a rounded nose.

Surface hydrology in the vicinity of the landslide is mostly absent. Og Lake lacks both surface inflow and outflow channels. Its shores are composed of limestone cobbles and boulders and a single very large boulder forms a small island in the middle of the lake. Surface drainage is lacking within the Valley of the Rocks as far down as the right lateral margin of the source area where, from the opposite valley side, a tributary of the Simpson River enters the valley cutting through bedrock at the edge of the debris. Once it reaches the valley floor it stays tightly against the left valley slope toe for over 4.5 km and then once it passes the terminus of the distal lobe makes its way into the centre of the valley bottom where it remains for a further 5 km until it makes a sharp 90 degree turn to the southwest to follow a transverse valley.

3.4.2 Morphology and metrics

Accuracy of landslide metrics depends on both the data source consulted and nature of the metric being measured. Data sources utilised here are reasonably accurate relative to the scale of the landslide. Consequently, the greatest sources of error stem from uncertainty about pre-failure topography. Horizontal metrics are, therefore, the most accurate, while depths of failed or deposited material are greater. Volume estimates are the most uncertain because of compound errors. Metrics involving

components oriented along the failure surface (e.g. scar length and area) were adjusted by a correction factor of 1.1 to compensate for foreshortening resulting from orthographic projection of an inclined (25°) surface. A summary of quantitative metrics discussed below is presented in Table 4.1.

3.4.2.1 Source area

The scar left by the failed rock mass is uniformly 4.2 km wide along slope, and varies in length down-slope from 1.35 to 2.65 km. The total area of the sliding surface is 7.2 km^2, 0.3 km^2 of which comprises the upper surface along the left margin. Elevation of the basal surface of the failed mass ranged from 2000 m at the toe of the sliding surface, to 2875 m at the unnamed peak in the central part.

Estimated thickness of the main slab was approximately 160 m. Depth of the failed mass varies from 40 m (above the minor sliding surface at the left margin) to roughly 400 m where the secondary ridge below Golden Peak entered the failure mass near the right margin. Based on the shape and depth of the scar and on the additional volume contributed by the additional ridge, volume of the failed mass, before bulking, is estimated as 1.3 Gm^3. This refines a previous rough estimate of 1 Gm^3 by Evans (2001). Overall, the average thickness of the failed mass was ca. 170 m.

3.4.2.2 Debris

Typical measurements used to characterize landslide deposits such as length (parallel to run out) and width (transverse to run out) do not directly apply to the Valley of the Rocks debris because of its irregularity and asymmetry. The morphology and mobility of the debris has been drastically influenced by topographic barriers, mainly the southwest valley slope, and differing transport modes. At its greatest dimensions, the debris stretches 2.3 km across the valley and 9.7 km along it. Surface elevations of the debris vary from 1625 m (at the distal limit) to 2330 m, with local relief within the debris varying from a few 10s of metres up 280 m.

The total debris area (13.25 km^2) includes approximately equal parts of the rocky debris mass (7.7 km^2) and the distal lobe (5.5 km^2). Volume contributions of these two parts to the total debris volume are very different due to substantial differences in debris thickness. The rocky debris mass comprises the majority of the deposit volume (ca. 1.3 Gm^3) and varies in thickness from roughly 50 to 300 m. The distal lobe (ca. 0.2 Gm^3) varies in thickness from a few metres near the distal and lateral margins to roughly 150 m in the proximal portion.

The total estimated volume of the in-situ debris is 1.5 Gm^3. Assuming an bulking factor of 20%, roughly that reported for the Tsaoling rock avalanche (Chen et al., 2005), the unbulked debris volume is ca. 1.2 Gm^3, an estimate that agrees very well with the estimated volume of the failed mass (1.3 Gm^3).

Comparison of the estimated source and debris volumes gives a lower bulking factor, (~12%), but uncertainty around this value is high as it is affected by uncertainly in the estimation of both volumes.

3.4.3 Orientation and morphology of sliding surface

Structural measurements from across the sliding surface (Figure 3.1) show a high degree of structural continuity over the entire source area (Figure 3.5). Mean strike varies less than 15 degrees over the entire area of the sliding surface. Mean dip varies from roughly 30 degrees to 22 degrees from the upper part to the lower part of the sliding surface. As these dips suggest, the sliding surface shows a slight concave-up profile and also seems to steepen and rotate clockwise very slightly nearer the right margin. Field observations (Figure 3.2) and profiles of the sliding surface parallel to dip direction (Figure 3.6) indicate that the concave-upward trend is continuous across the scar.

Joints are not apparent on the exposed sliding surface, except on the upper, fresher sliding surface at the left lateral margin where two sets align with jagged surfaces making up the lateral scarps. Widely spaced bedding-normal joints were visible in vertical exposures through the Palliser Formation, particularly at the left lateral scarp and in towers along the ridge marking the upper limit of the sliding surface. No joints sets could be resolved by the 15m panchromatic imagery.

Overall lateral release surfaces strike parallel to the dip direction of the sliding surface. The apparent trend of these aligns with other topographic features cutting across the structural grain of the area. In particular, the right lateral margin aligns with a steep ridge on the opposite valley side (Figure 3.1).

3.5 Discussion

3.5.1 Failure kinematics

Initial failure of the Valley of the Rocks rock avalanche involved simple planar sliding (Figure 3.7). Lateral release surfaces were almost parallel to the direction of sliding. Although they cannot be related directly to bedding normal joints, similarity of the orientation of lateral release surfaces to the features transverse to the overall structural grain of the area suggest macro-scale fabric of the range is important in defining release surfaces. Specifically, alignment of the right lateral scarp with a cliff on the opposite valley side suggests presence of a major structure cutting transversely across the entire valley and helping to define the right lateral release surface.

Daylighting resulting from steepening of the pre-failure valley slope is apparent in slopes immediately northwest of the right lateral margin and is observed to extend down valley. This toe steepening is likely a result of glacial erosion when the area was occupied by valley glaciers. Based on the current degree of

variability along cataclinal slopes in the valley and adjacent areas, the pre-failure slope was also likely variable (represented as a zone in Figure 3.7).

The average dip of the sliding surface corresponds to the lower limit of basic friction angles of slope forming Paleozoic carbonate rocks determined from natural slope orientations in a study area immediately to the southeast (Cruden and Eaton, 1987). Based on laboratory experiments and field observations, Cruden (1985) suggested that bedding-parallel shear strength in undeformed, unsoftened, unaltered, unpolished bedding planes in hard carbonate rocks in the Rocky Mountains is best approximated by the basic friction angle, which varies from 21.5 to 41.3 degrees for ridge forming carbonates in the Rocky Mountains (Cruden and Hu, 1988).

The nearest mapped thrust faults to the scar outcrop in the anaclinal slopes of the source ridge and of the opposite valley side, but no thrust faults are mapped corresponding to the sliding surface (Leech, 1979) nor were they detected in the field. The high extent of the sliding surface suggests, however, that a preferentially weakened surface may have been present prior to failure; given the tectonic setting and the orientation of the sliding surface a thrust fault is most likely. The resulting bedding parallel shear would have reduced shear strength along the sliding surface. Fault pre-shearing would help, but is not required to, explain the lower than average friction angle implied by the dip of the sliding surface.

3.5.1.1 Importance of landscape-scale controls

The size and shape of the initial failure mass was limited by geologic structures and relief. Simultaneous failure over such a large area requires high structural continuity of the sliding surface and pervasive persistent lateral release surfaces. In the case of the initial rock slide, these were provided by uniform unfolded bedding surfaces and the probable existence bedding-normal joint sets.

The overall shape and area of the sliding surface was influenced by pre-failure ridge line topography, which resulted in additional loading by the high central peak and potentially preferential location of lateral release surfaces oriented parallel to dip. . Release along such a great length of the toe of the failed mass resulted from the parallelism between the strike of the sliding surface and the valley-side slope as well as oversteepening resulting in under-dip conditions. Toe release was, therefore, ultimately a result of the influence of structural grain on topography and Pleistocene glaciation.

The great thickness of the failed mass resulted from a combination of the high strength of the rock mass involved, which resisted more temporally uniform mass wasting, and the presence of relatively few preferentially weak discrete discontinuities with the mass. Tectonic modification of the rock mass may have also played an important role in the size of the failure by defining an extensive preferentially weakened surface for sliding.

3.5.2 Debris transport and emplacement

Overall the landslide was highly mobile. Substantial run up on the opposite valley slope and significant run out down valley indicate transport at catastrophic rates. Fragmentation and dispersal of the debris suggest substantial disintegration and spreading during transport.

   Variations in morphology and other characteristics of the debris indicate two separate transport mechanisms. The failed mass disintegrated during transport to form a rock avalanche, represented by the main rocky debris mass. Morphology of this deposit resembles other known rock avalanches in carbonate rocks (e.g. Avalanche Lake, Rockslide Pass) and, in particular, other gigantic rock avalanches in carbonate sequences (e.g., Seymareh, Flims) in several ways. Presence of shattered but unseparated blocks too large and numerous to be attributed strictly to post-failure weathering, such as those observed at the Valley of the Rocks, have been reported from various rock avalanche deposits (Harrison and Falcon, 1938; Shreve, 1968). The steep irregular surface relief of the debris, including wave-like mounds, is similar to those reported at the Seymareh rock avalanche (Chapter 3; Harrison and Falcon, 1938). Debris run up of 300 m up the opposite valley side is comparable to run up over major topographic barriers reported for the Seymareh rock avalanche (500 m; Chapter 2) and the Avalanche Lake rock avalanche (640 m; Evans, 1989). The steep back slope of the debris mass and occurrence of lowest debris elevations near base of the sliding surface indicate that debris did not remobilise back down the slope in a reverse direction. The fragmental flow was, therefore, not fluid after initial upslope motion stopped and supports the impression that the initial fluidity of the mass was due to flow as a rock avalanche rather than due to water content.

   Following the initial rock avalanche, the northeast part of the debris remobilized as a distal flow. The overall fragment size of the rocky debris mass decreases from the left to right sides of the scar. The displaced material is present as the hummocky distal lobe. The substantial difference in debris morphology and surface relief when compared to the rocky debris mass suggest remobilisation involving a different transport process. Specifically, lower relief, more lobate morphology, greater soil development and gentler surface slope of debris suggest its movement was more fluid. This morphology and enhanced run out suggested that undrained loading of valley fill, consisting of glacial materials, caused the liquefaction of the subjacent materials resulting in a more mobile flow. A similar distal deposit is visible on air photos of the Rockslide Pass rock avalanche, Mackenzie Mountains. The large scarp marking the limit of the remobilized flow indicates that it failed in a down-valley direction and that is was a distinctly separate process rather than a continuation of the initial transport mechanism.

3.5.2.1 Importance of landscape-scale controls

Mechanisms of debris transport and emplacement in the Valley of Rocks rock avalanche were a direct result of the conditions of initial failure and of the physiography of the valley. Disintegration of the rock slide into a rock avalanche required rapid energy release and, therefore, resulted from the initial catastrophic transport of the rock mass. The relatively short run out and great thickness of the rock avalanche deposit resulted directly from the topographic barrier posed by the opposite valley side.

Lateral spreading of the rock avalanche was limited because of the short run out. Spreading in the up valley direction was further limited by topographic resistance and this portion of the debris was not mobile. At the down-slope end, the lack of lateral spreading and the great thickness of the initial deposit resulted in high, steep and debris margin which would have been unstable. The valley slope here favoured continued transport, but the geometry of this path relative to the initial transport direction prevented continuity of flow from the rock avalanche. Instead, the unstable margin was remobilized by a secondary failure of the debris, which left the large scarp, resulting in the downstream distal flow. Morphology of this secondary failure is suggestive of increased water content, which most likely resulted from undrained loading of the valley bottom sediments. Correspondence of the secondary failure with valley bottom sediment loading suggests that it was more-or-less contemporaneous with the rock avalanche. The much greater run out of this secondary distal flow (5.7 km parallel to its overall transport direction) relative to that of the initial rock avalanche (1.9 km from the toe of the sliding surface parallel to its overall transport direction) was a result movement parallel rather than transverse to the valley trend, and due to the decreased frictional resistance at the base of the debris due to undrained loading of valley bottom materials.

3.5.3 Age / timing

Timing of the rock avalanche was likely de-glacial or immediately post-glacial. The degree of in situ weathering of debris and erosion of the exposed sliding surface suggest the rock avalanche is of substantial antiquity. The hummocky debris surface in the Valley of the Rocks does not exclusively indicate that failure was onto a valley glacier that subsequently melted, as Duffy (1967) suggested; similar hummocky surfaces are common on rock avalanche deposits, including those in areas that have never been glaciated (Chapters 2 and 3). There is no evidence of modification of debris by ice or melt water. Since the failure must have occurred after the valley bottom became ice free, a maximum age for the failure is suggested. The Eisenhower Junction Advance (Rutter, 1972) was the last advance of valley glaciers along this region of the Continental Divide (Jackson, 1980b). Minimum ages for subsequent

retreat of ice to cirques range from over 10,000 years BP (Luckman and Osborn, 1979) to 9,330 ± 170 (GSC-332) (Rutter, 1972).

The geomorphic evidence suggests that the failure occurred sometime after the removal of valley glaciers otherwise undrained loading of valley bottom sediments would not have been possible. It is likely that the failure followed soon after deglaciation as the source slope would have been most prone to failure just immediately following the de-buttressing of the steepened rock slope toe by retreating valley ice. The maximum age for the landslide of roughly 9,000 to 10,000 ^{14}C years BP is, therefore, also the most likely age.

3.6 Conclusions

The large volume of the Valley of the Rocks rock avalanche resulted from the high degree of structural continuity of the sliding surface. The dip-slope failure occurred in a southwest-dipping thrust sheet and was completely within massive Devonian Palliser Limestone without involvement of weaker units. The failure mode and lithology involved are both common in mass wasting in the region, as are the presence of thrust sheets. The sliding surface may have been weakened prior to failure by bedding plane slip resulting from tectonic processes.

Debris was emplaced in two modes: initially as a rock avalanche and, subsequently, by remobilization of the northwest part of the mass due to undrained loading of valley bottom sediments. The latter mode resulted in enhanced mobility of the distal lobe and in differential mobility of the failed mass. Age of the rock avalanche appears to be very late glacial or very early post-glacial. Timing of the largest rock avalanche in North America is thus similar to most non-volcanic gigantic landslides around the world (Chapter 2; Deplazes et al., 2007; Hancox and Perrin, 1994).
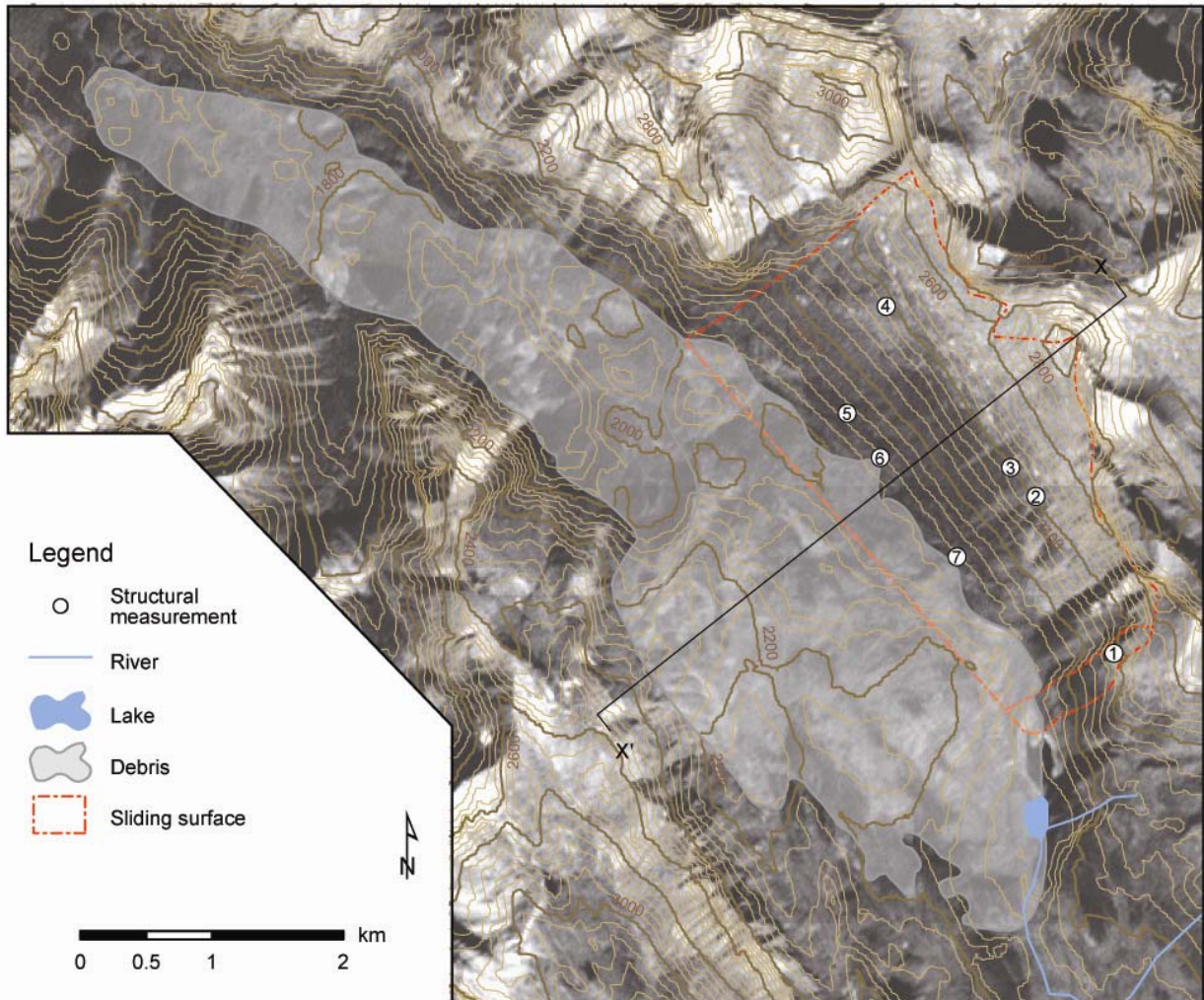
Figure 3.1: Map of the Valley of the Rocks rock avalanche, Mount Assiniboine Provincial Park, British Columbia, Canada (50° 59' N 115° 38' W).

Note differences in debris morphology. Locations of structural measurements summarized in Figure 3.5 and location of cross-section x-x in Figure 3.6 are indicated. Map based on interpretation of aerial photographs, Landsat image, DEM and on field observations. Contours line from CDED DEM (contour interval is 40 m). Image base is the Landsat image.

Figure 3.2: View down valley through the Valley of the Rocks from near the left lateral scarp showing the sliding surface and central portion of the rocky debris mass.

Nasswald Peak (N) is visible at the top of the right lateral margin and the northwest-most castellated remnant is visible at the upper limit of the sliding surface (upper right middleground). The debris of the distal flow extends roughly 5 km down valley beyond Nasswald peak.

Figure 3.3: Left lateral scarp of the Valley of the Rocks rock avalanche.

The main sliding surface (left) is covered in this area by talus. The higher and smaller surface (right) is the minor sliding surface. Discontinuous head scarp above this portion of the main sliding surface is up to 90 m high.

Figure 3.4: Anaclinal slope of failed ridge.

Central part of the dipslope sliding surface extending down from the unnamed peak (centre middleground) is parallel to bedding outcropping in the anaclinal slope. Nasswald Peak and the back of Og Mountain are visible in the centre background and left foreground, respectively. Minor peak just past Og Mountain is the back of part of the discontinuous head scarp. The overall ridge in this view forms part of the Continental Divide. Sliding was to the left, parallel to bedding.
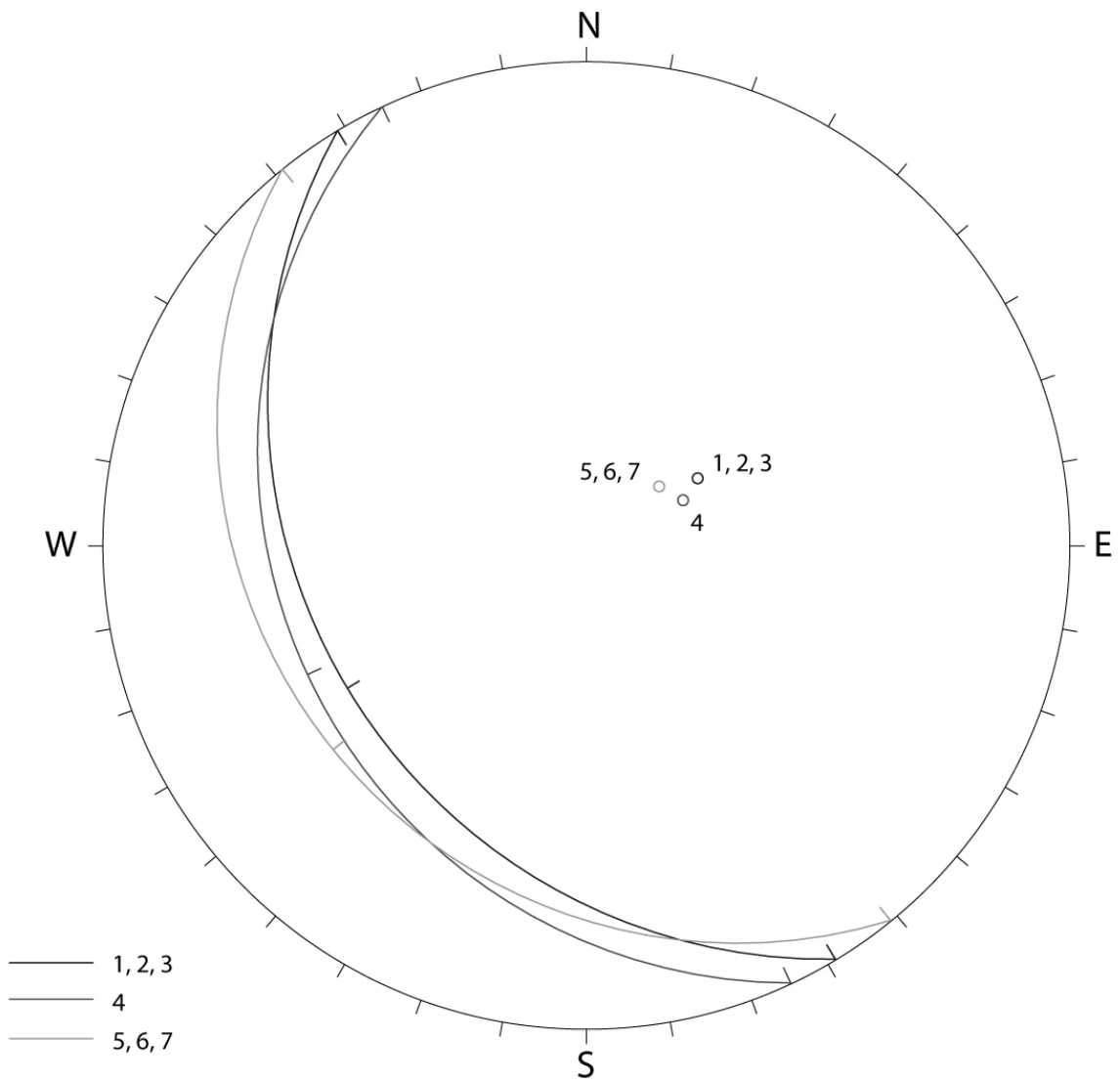
Figure 3.5: Stereonet showing minor structural deviation across the sliding surface.

See Figure 3.1for location of measurements. Poles and great circles are plotted for three mean orientations (locations 1, 2 and 3; location 4; and locations 5, 6 and 7) each representing consistent bedding measurements. Sampling at each of the seven locations included between 15 and 42 individual structural measurements of the exposed bedrock surface (Appendix F).
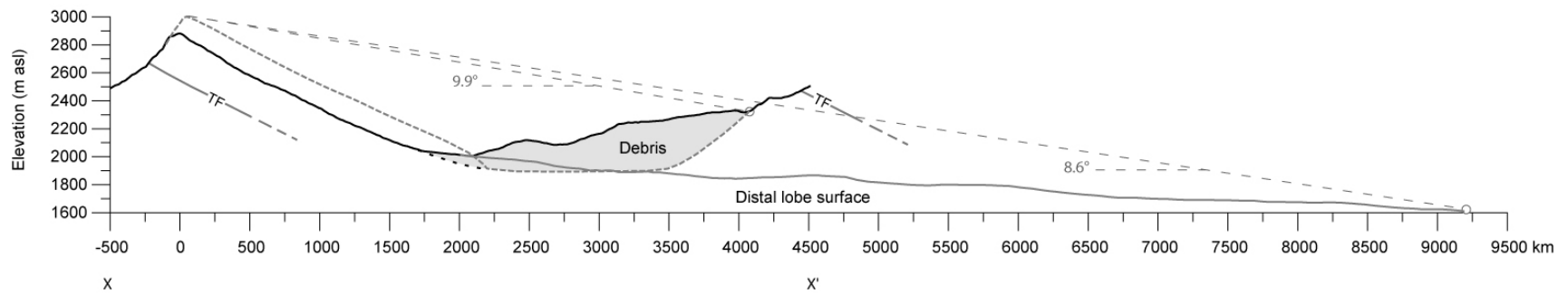
Figure 3.6: Cross-section through the Valley of the Rocks rock avalanche.

See Figure 3.1 for profile location. Thrust fault (TF) location is approximate, based on Leech (1979). Thrust faults mark contacts of Palliser Limestone (Devonian).

61
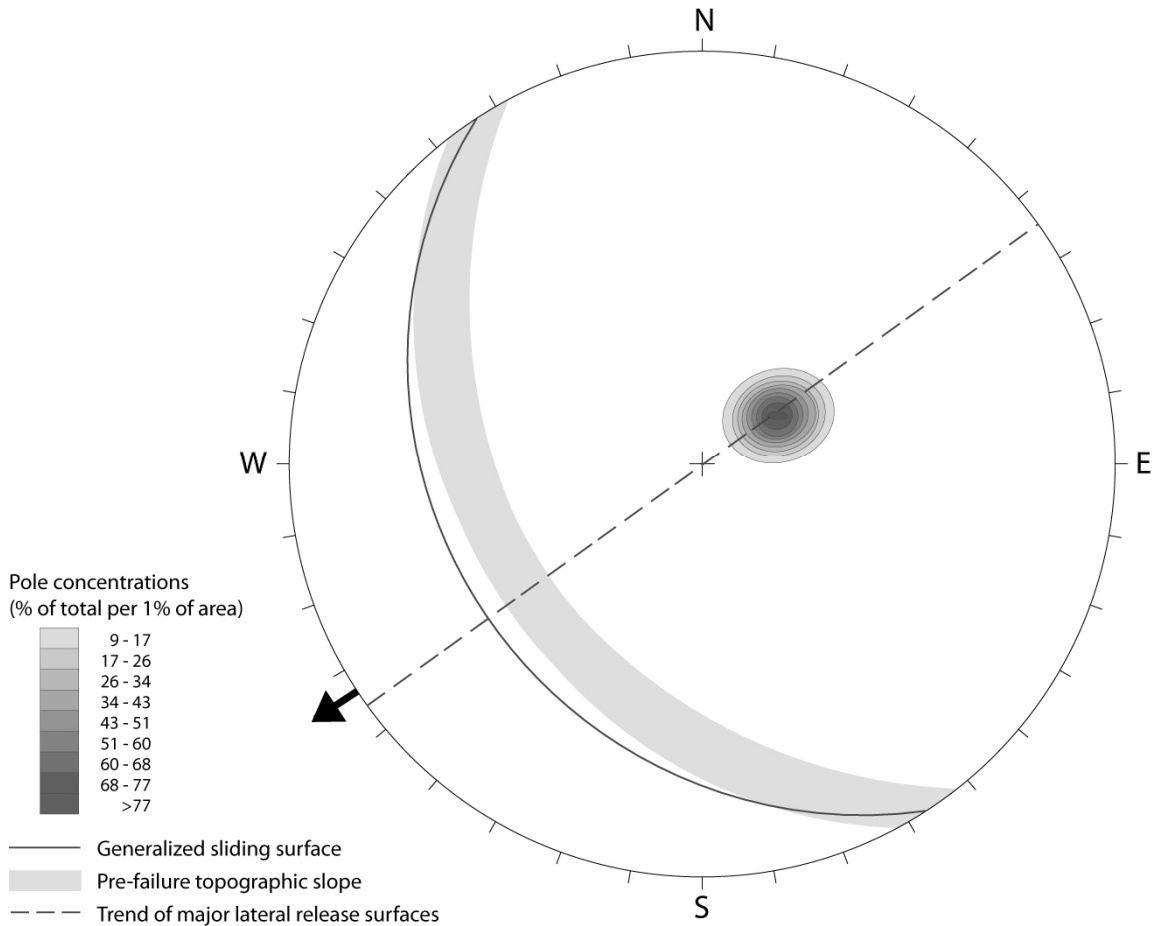
Figure 3.7: Kinematic summary of the initial rock slide at Valley of the Rocks represented on a stereonet.

Mean sliding surface orientation is shown as a great circle. All sliding surface measurements are shown as a pole concentration. Due to variability in actual orientation, the pre-failure topographic slope is represented as a zone. Black arrow in southwest quadrant is mean direction of initial movement. The stereonet indicates the failure mode was planar, with sliding parallel to both the bedding and topographic slope.

Table 3.1: Summary metrics of the Valley of the Rocks rock avalanche.

Failed mass

Volume[a]		1.3 Gm^3
Area		7.2 km^2
Maximum width (across slope)		4.20 km
Length (down slope)		2.65 km
Depth:	minimum	40 m
	maximum	400 m
	mean[b]	180 m
Elevation range		875 m
Minimum elevation		2000 m
Maximum elevation		2875 m

Structure

Mean sliding surface dip	25 °
Mean sliding surface strike	147 °

Debris

Volume (bulked)[a]		1.5 Gm^3
Volume (with out bulking)[c]		1.2 Gm^3
Area		17.0 km^2
Maximum width (transverse to valley trend)		2.3 km
Maximum length (along valley)		9.7 km
Depth:	minimum	10
	maximum	300 m
	mean[b]	90 m
Distal elevation		1625 m
Maximum elevation		2330 m

Mobility proxies: rock avalanche portion

Runout (failure plan toe to distal debris)	7 km
Runout (headscarp to distal debris) (L)	9.2 km
Height of fall (headscarp to distal debris)	1250 m
H/L	0.136
Fahrböschung	8.6 °

Mobility proxies: distal lobe

Runout (failure plan toe to distal debris)	1.9 km
Runout (headscarp to distal debris) (L)	4.1 km
Height of fall (headscarp to distal debris)	575 m
H/L	0.140
Fahrböschung	9.9 °

[a] independently estimated
[b] area-weighted
[c] assuming 20% bulking

Chapter 4
Discussion and Summary

4.1 Comparison

Initiation of the Seymareh and Valley of the Rocks landslides was determined mainly by structural and topographic controls, which are remarkably similar for both cases. Both landslides involved planar sliding on bedding characterized by an extremely high degree of structural continuity. At the Valley of the Rocks the sliding surface may have been pre-weakened by thrust faulting. At Seymareh, pre-weakening of bedding surfaces by fold-related slip is strongly supported by field observations, broad scar morphology and relation to stratigraphy. Lateral release in both failures was provided by bedding orthogonal joint sets, although faulting may have had a role in defining the right lateral release surface of the Valley of the Rocks rock avalanche. Multiple joints defined release surfaces of both landslides, but in the case of Seymareh continuous release along specific joints was more pervasive. This difference is likely to do significant weakening of select joint orientations in the Zagros fold-thrust belt by far field stress conditions and because one orientation in particular was parallel to the dip direction of bedding and the pre-failure topographic slope. Topographic controls on initiation included similarity of pre-failure slopes in relation to pervasive rock mass structure, resulting to from high physiographic control of bedding. Kinematic release a the slope toe was provided by break-out assisted by fluvial undercutting in the cases of the Seymareh rock avalanche, and by day-lighting of bedding due to glacial undercutting in the case of the Valley of the Rocks rock avalanche.

Post failure behaviour of both rock avalanches was determined by topography and, in the case for the Seymareh rock avalanche, also by geologic structure. Initial transport of the Seymareh rock avalanche was as stacked sliding plates defined by bedding and divided laterally by major joint sets into platelets. Together with a lack of major topographic barriers (relative to the scale of the failure), stacked sliding contributed to the high run-out of the debris. Pre-failure valley bottom topography influenced morphology of the debris mass. There is no evidence for the role of structure in initial transport of the Valley of the Rocks rock avalanche. Topography greatly influenced debris transport and, together with undrained loading of valley bottom sediments, resulted in two discrete debris masses with differing transport mechanism.

64

Despite the aforementioned similarities in controls of initiation and transport, the volume of the Seymareh rock avalanche exceeds that of the Valley of the Rocks rock avalanche by over an order of magnitude. Comparison of source area dimensions of the failures (Table 5.1) suggests one likely explanation. Because of continuity and pervasiveness of structures in both source slopes, maximum constraints on potential failure length and width were defined by source slope dimensions. The dimension of the intact northeast slope of Kabir Kuh greatly exceeded those of the unnamed ridge involved in the Valley of the Rocks in width (parallel to strike) and length (perpendicular strike) and, consequently, the failure at Seymareh was wider (across slope) and longer (down-slope) (Table 5.1). The ratio of mean failure depth to length of failure is remarkable similar for both failures (Table 5.1). Given the similarity in structural dip ultimately controlling each failure, this relationship may suggest an upper limit on failure depth as a function of pre-existing slope length. Width to length ratio is greater for the Seymareh landslide by almost a factor of two (Table 5.1), suggesting that differences in failure width had the greatest affect on failure volume. It follows, therefore, that while the length of the flank of Kabir Kuh influenced failure size, the width along the strike of the anticline had the most pronounced influence on the volume of the failed mass.

Other factors were also important in determining the size of the failures. While the upper (topographic) surfaces of both failures were highly competent limestone, underlying weaker units were present only at Seymareh. Presence of weaker layers at depth may have allowed the failure to progress deeper into the sequence of the source slope than would have otherwise been possible. Structural orientation within the source slope also likely played a role in determination of the failure. For dip slope failures, lower bedding dip will result in the kinematic freedom of a greater thickness of material given the same amount of under cutting at the slope toe (Figure 4.1). Average sliding surface (e.g. bedding plane) dip at Seymareh was lower (by 5°) than at Valley of the Rocks (Table 5.1), favouring a greater thickness of failure normal to the failure surface. The even lower (11°) dip of the overall failure surface at Seymareh further aided this effect.

4.2 Volume and mobility

The mobility and volume determined for the Seymareh and Valley of the Rocks rock avalanches in this work agree well with other non-volcanic landslides (Figure 4.2). The mobility and volume of landslides is typically a power law (Hayashi and Self, 1992). Hayashi and Self's consideration of non-volcanic landslides included the Seymareh rock avalanche, but not the Valley of the Rocks rock

avalanche. the data they used for the Seymareh rock avalanche (from Harrison and Falcon, 1938), however, was in accurate; volume was grossly under estimated (20 Gm^3) and mobility were underestimated (H/L = 0.08).

Addition of the Valley of the Rocks rock avalanche to Hayashi and Self's (1992) dataset and revision of the Seymareh rock avalanche results in a slight change to the power law for non-volcanic landslides (Figure 4.2). Most importantly, the newly determined volume for the Seymareh rock avalanche suggests and upper limit for landslide volume and, therefore, mobility on the Earth's continental surface.

4.3 Summary

Documentation and understanding of the largest non-volcanic rock avalanche in North America (1.3 Gm^3) and the largest non-volcanic rock avalanche in the world (38 Gm^3) have been greatly improved by the investigations presented in Chapters 2 and 3. Additionally, this work adds to global knowledge of gigantic landslides, especially with regard to topographic and structural controls on size and initiation. The volume of both landslides were previously underestimated; undervaluing was especially great in the case of the Seymareh rock avalanche (nearly fifty percent). Age constraints on the Valley of the Rocks rock avalanche, based on geomorphic evidence, and for the Seymareh rock avalanche, from radiocarbon dating, indicate that both landslides are of roughly the same age and that they correspond with ages of numerous other non-volcanic gigantic landslides around the world (ca. 8-10 ka BP). Geologic structure (specifically bedding) and topography were the major factors controlling landslide size, initiation and initial transport. Topography played the most important role in the final stages of transport and in emplacement. A secondary outcome of the investigations is the demonstration of the value of combining remotely sensed data of different scales and types in the investigation of gigantic landslides. The approach used in the case of the Seymareh and Valley of the Rocks rock avalanches provides a general methodology for low-cost remote sensing-based investigation of gigantic landslides that can be varied depending on data availability. The utility of this approach is evident in the first ever detailed documentation and analysis of the largest rock avalanche in North America and of the largest rock avalanche in the World.
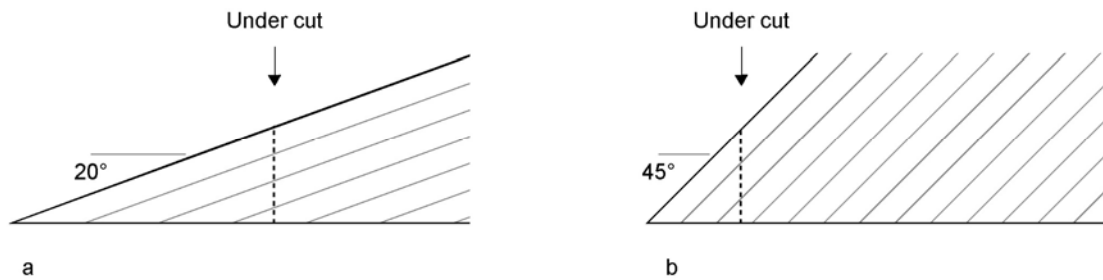
Figure 4.1: Schematic representation of influence of bedding dip on thickness of kinematically free mass following undercutting.

Two dip-slope rock masses with the same uniform bedding thickness dipping at a) 20° and at b) 45° are shown. Given the same depth of undercutting at the toe causing day-lighting, a greater thickness (three beds) will bed kinematically free to fail in the shallower dip-slope (a) than in the steeper dip-slope (two beds; b).
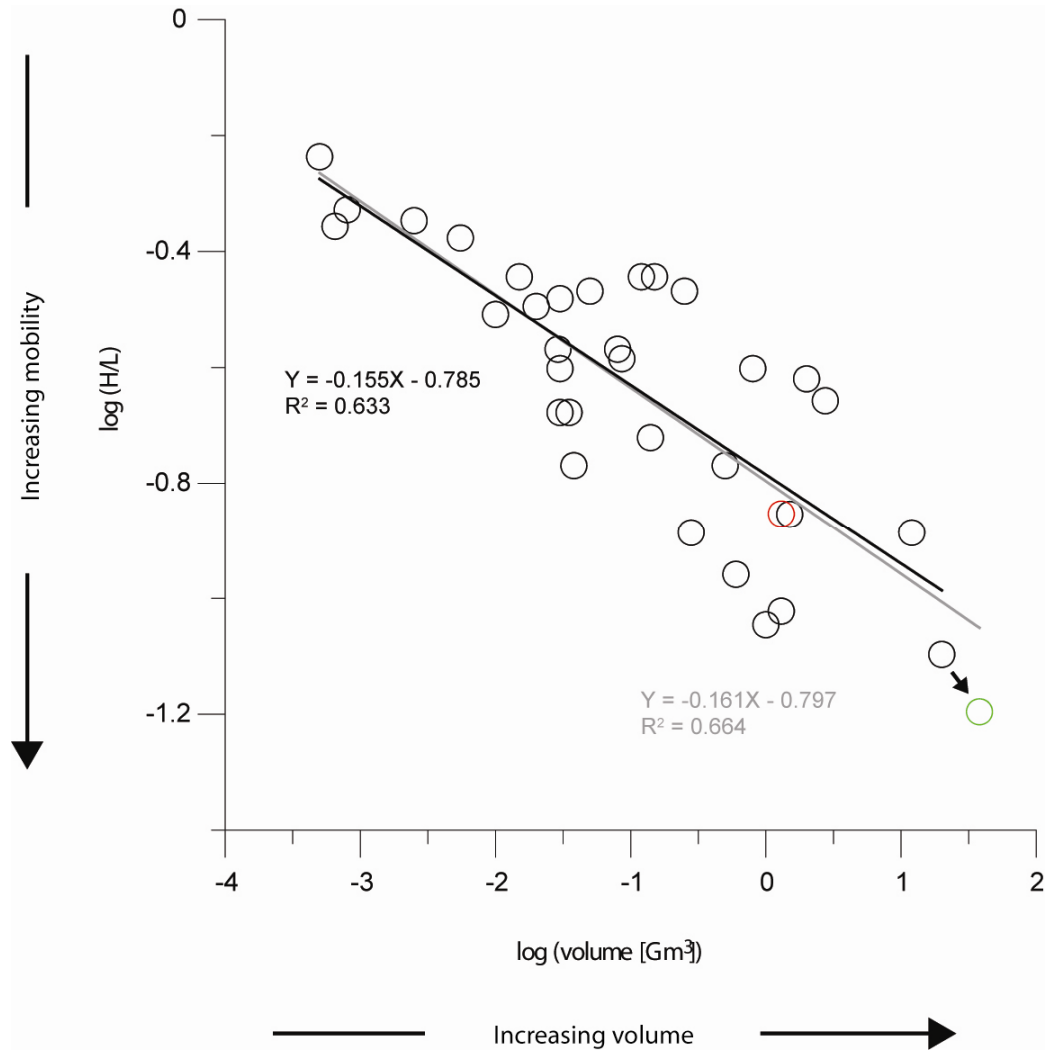
Figure 4.2: Mobility (H/L) – volume relationship for selected non-volcanic landslides on the Earth's continental surface.

Data from Hayashi and Self (1992) (black) and this study (Seymareh, green: H/L = 0.06, volume = 38 Gm^3; Valley of the Rocks, red: H/L = 0.14, volume = 1.3 Gm^3). Power laws are based on Hayashi and Self's data (black) and Hayashi and Self's data with the addition of the Valley of the Rocks rock avalanche and revision of the Seymareh rock avalanche (grey). Position of the Seymareh rock avalanche has shifted (from lower right-most black circle).

Table 4.1: Summary of source area metrics and structure of the Seymareh and Valley of the Rocks rock avalanches.

	Seymareh		Valley of the Rocks	
Dimensions				
Volume	38	Gm^3	1.3	Gm^3
Area	100	km^2	7.2	km^2
Maximum width (across slope)	15.5	km	4.2	km
Length (down slope)	6.1	km	2.7	km
Depth: minimum	250	m	40	m
maximum	680	m	400	m
mean	410	m	170	m
Aspect ratios				
Width:length	2.5		1.6	
Average depth:length	67.2		64.2	
Average depth:width	26.5		40.5	
Structure				
Mean sliding surface dip	19	°	25	°
Mean sliding surface strike	298	°	147	°
Overall basal failure plane slope	11	°	n/a	

Appendix A

Methodology for the remote sensing-based investigation of gigantic landslides

The methodology for remote sensing-based investigation of gigantic landslides used in the current study is described here. The methodology has been designed to provide a low cost option to improve the data coverage and information available for investigation of gigantic landslides, but it is also applicable to other spatially-extensive geomorphic feature that present challenges to holistic field investigation. The unique aspect of the approach is its integration of multi-scale datasets of various types with traditional field methods.

Remote sensing is not a replacement for field investigations, but rather a technique to expand the types and coverage of data available for investigation of large-scale landscape features. Field investigations are important in that they provide out-crop scale observations not possible using remote sensing alone because of scale and orientation of these features. Field observations are also necessary for ground truthing of interpretations and analyse of remotely sensed data. Ideally, the methodology should, therefore, be incorporated with traditional methods of field investigation to provide a truly multi-scale approach. In the case of very poorly accessible localities, however, the methodology can instead function as a general reconnaissance lacking field investigation.

The overview of the methodology below is divided into four parts: 1) an overview of datasets and sources used and the types of data that can be derived from them; 2) description of data processing used; 3) description of data extraction and interpretation used; and 4) description of final outputs.

A.1 Overview of datasets and sources

A.1.1 Orbital imagery

The specific uses and overall utility of orbital optical data depends on its spatial and spectral resolution. Increasing spatial resolution generally increases in the number of different types of features that can be interpreted or analysed. The number and types of spectral bands present determine how well features can be identified and differentiated. The two systems described below range from free to moderate cost. Very high spatial resolution systems (e.g. IKONOS and Quickbird) are available and have the potential to greatly assist investigation of gigantic landslides, but are very high cost and were, therefore, not used.

A.1.1.2   Primary uses

- Detection and general assessment of landscape-scale features (e.g. faults and other major structures, rivers)
- Delineation of major features of gigantic landslides (debris and scar morphology and area)
- Determination of horizontal metrics (from orthorectified imagery only).
- Detection and measurement of meso-scale structural and lithologic feature (e.g. joint and bedding control on topography, traces of weather discontinuities)

A.1.1.2   Datasets used

Seymareh

Two orthorectified Landsat7 ETM+ images were downloaded from the USGS Center for Earth Resource Observation & Science Center (EROS) using USGS Global Visualization Viewer (http://edc.usgs.gov/). One image (NASA Landsat Program, 2002a) provided complete covered of the landslide and adjacent terrain, but a second image (NASA Landsat Program, 2002b) was required to extend coverage to the entire area of the lacustrine deposits associated with the landslide. Each multi-band image is composed of a panchromatic band (15 m), six visible, near infrared and middle infrared bands (30 m), and a thermal infrared band (60 m). The images were projected in a local UTM zone (Zone 38N).

A single SPOT 5 (10 m) multispectral image was purchased from in 2001 (SPOT, 1994). The 4-band image provides coverage of the entire landslide and adjacent terrain. The images were projected in a local UTM zone (Zone 39N).

Valley of the Rocks

A single orthorectified Landsat7 ETM+ image (Centre for Topographic Information, 2004) was ordered and downloaded through GeoBase (http://www.geobase.ca/). The image provides coverage of the entire landslide and adjacent terrain. The image was projected in a local UTM zone (Zone 11N).

A.1.2 Aerial photography

Like orbital imagery, the utility of aerial imagery depends on resolution. Resolution in the case of aerial photographs is mostly a result of scale, which is in turn determined by flying height and camera focal length. In general, larger-scale (e.g. 1: 10 000) photographs provide greater resolution than smaller-scale (e.g. 1: 60 000) photographs. Even small-scale aerial photographs typically provide greater resolution than very high resolution orbital imaging systems. Consequently, aerial

photographs provide information on small-scale features. Additionally, stereoviewing provides information on three-dimensional morphology.

A.1.2.1 Primary uses

- Delineation of detailed features of gigantic landslides (e.g. meso- and even outcrop-scale morphology of debris)
- Detection and measurement of meso- to outcrop-scale structural and lithologic features (e.g. joint and bedding control on topography, traces of weather discontinuities)

A.1.2.2 Datasets used

Seymareh

Two sets of aerial photographs were used. Small-scale (1: 60 000) scale panchromatic photos made in 1955 for the United States Army Map Service, Corps of Engineers provided coverage of the entire landslide and immediately adjacent terrain. Large-scale (1: 20 000) panchromatic aerial photographs acquired by the National Cartographic Center of Iran cover the landslide debris, but not the source area. The latter were of relatively poor quality and low contrast. Both photo sets were received as hardcopy positives.

Valley of the Rocks

Panchromatic aerial photographs of various (1: 10 000 to 1: 60 000) scales were obtained from British Columbia and Alberta provincial archives. All photos are panchromatic and were received as hardcopy positives.

A.1.3 Digital elevation data

A.1.3.1 Primary uses

- Interpretation of three-dimensional morphology of landscape- and meso-scale features (e.g. nature of the debris surface)
- Determination of vertical geometrics

A.1.3.2 Datasets used

Seymareh

A Shuttle Radar Topographic Mission (SRTM) DEM covering slightly greater than the area of coverage of the Landsat images was downloaded from the USGS Seamless Data Distribution System (SDDS; http://seamless.usgs.gov/). The dataset was created during the Shuttle Radar Topographic mission, February 2000 (Farr et al., 2007). Its coordinate system was GCS WGS84 and was

downloaded as a .tiff file. Resolution of STRM DEMs varies with latitude, but is roughly 3arc seconds (~90 m).

Valley of the Rocks

Digital elevation models of the Canadian Digital Elevation Database (CDED) were downloaded from GeoBase (http://www.geobase.ca/). The DEMs were created from digitally converted NTS contour maps Datasets used were for map sheets 82 J/13 and 82 O/04. The coordinate system of both was GCS NAD83. Both were downloaded as .dem files. Resolution of CDED DEMs derived from 1: 50 000 map sheets is dependent on latitude, but is roughly 0.75 arc seconds.

A.1.4 Field observations and data collection

A.1.4.1   Primary uses

- Interpretation of outcrop-scale topographic, lithologic and geomechanic features.
- Ground truthing of landscape- and meso-scale interpretations from remotely sensed datasets

A.1.4.2   Datasets used

At both sites field investigation involved basic geologic and geomorphic mapping, collection of structural measurements, assessment of geomechanical properties and ground truthing of remotely sensed data (particularly orbital and aerial imagery). Locations of measurements and traverses were recorded by hand-held GPS.

A.1.5 Ancillary data sources

A.1.5.1   Primary uses

- Verification of interpretations based on and geometrics derived from remotely sensed datasets

A.1.5.2   Datasets used

Seymareh

Geologic maps compiled by the Iran Oil Operating Companies in the 1960's at 1: 100 000 scale were obtained in .tiff format. Four maps covered the area of interest (Macleod, 1970; Setudehnia and Perry, 1967a, 1977b; Takin et al., 1970). Two hard-copy 1: 50 000 topographic maps covering the area of interest were also obtained.

Valley of the Rocks

A recognisance geologic map (1: 100 000) produced by Leech (1979) and NTS topographic map sheets 82 J/13 and 82 O/04 were acquired as a paper maps.

A.2   Processing methods

Processing of digital datasets was conducted in a geographic information System (GIS) environment (ArcGIS 9.2). Aerial photographs were interpreted manually using a mirror stereoscope. Ancillary datasets in digital form were georeferenced to facilitate combination with other datasets in the GIS environment. Analogue ancillary datasets were compared visually with digital datasets. Features of interest from both digital and ancillary datasets were incorporated directly into the GIS environment by softcopy digitizing.

A.2.1   Orbital imagery

Visible and near infrared bands (bands 1-4) of each Landsat image were merged in ArcGIS. Normal colour (bands 1,2,3) and near infrared false colour (bands 2,3,4) composites were produced form merged bands. Individual bands of each composite were contrast enhanced by manual linear stretching in ArcGIS. Contrast enhanced composite images were pansharpened (Lillesand et al., 2007) in ArcGIS using the panchromatic band (band 8). Individual bands of the SPOT composite were contrast enhanced by manual linear stretching in ArcGIS.

A.2.2   Aerial photography

Air photos were not scanned and, consequently, not processed.

A.2.3   Digital elevation data

The SRTM DEM was left as a .tiff format. The CDED DEMs were converted to .grid formats in ArcGIS and then displayed. Projections of displayed .tiff and .grid DEMs were converted 'on-the-fly' in ArcGIS to the same local UTM zone used for the corresponding Landsat image. The projection conversion tool in ArcToolbox was not used because it did not function properly (Pers. Comm., ESRI, 2006). Raster images of slope degree, aspect and hillshade were produced from the projected DEMs in ArcGIS using ArcToolbox tools of the same names, respectively.

A.2.4 Field observations and data collection

No processing was required.

A.2.5 Ancillary data sources

Digital geologic maps were georeferenced using coordinate girds of the maps and using the same local UTM zone as the Landsat images. Hard-copy topographic maps were not scan and, consequently, not processed.

A.3 Data extraction and interpretation

A.3.1 Orbital imagery

Contrast enhanced, pansharpened Landsat composites and contrast enhanced SPOT composites were visually interpreted. Interpretations were compared with air photo interpretations, field observations and geologic maps. Horizontal metrics were measured using the measure tool in ArcGIS (Appendix B) and compared with ancillary data sources by either direct measurement (topographic maps) or measurement using the measure tool in ArcGIS (geologic maps). Features of interest (e.g. debris limits, source area, lacustrine deposits, drainage) were soft copy digitized. Areas were determined form digitized polygons (Appendix B). Apparent trends of linear features (e.g. traces of bedding normal joints) were measured in the GIS from orthorectified Landsat images.

A.3.2 Aerial photography

Viewing using a mirror stereoscope was used for manual interpretation of aerial photographs. The large-scale photos are of poor contrast and clarity. Due to their scale and lack of coverage for the source area, they were of limited use. The medium-scale air photos aided mapping of features not adequately represented on orbital images and extended the scope of field observations. Interpretations were made on acetate overlays and compared visually with interpretations of orbital imagery and with field observations.

A.3.3 Digital elevation data

Elevation data were used it two ways. Elevations at specific points of interest were determined using the inquiry tool in ArcGIS. Multiple transects parallel and perpendicular to the initial landslide transport direction and transects parallel to overall valley orientation were produced from the DEMs

and plotted. Transects allowed measurement vertical metrics of source area and debris geometrics and general characterization source area structure.

A.3.4   Field observations and data collection

Structural measurements of bedding orientation were made with a Brunton compass using the right-hand rule convention (Appendices C and F). All structural measurements (both field-measured and measured from orthorectified imagery) were compiled in stereonets using the software DIPS and interpreted visually.

Geologic and geomorphic field observations were recorded and documented photographically. Locations of all photographs and measurements were recorded by hand-held GPS and entered into the GIS environment to allow correlation with orbital imagery, DEMs and digital ancillary data sources.

A.3.5   Ancillary data sources

Geologic and geomorphic interpretations recorded on geologic maps were compared with those made independently in this study. Horizontal metrics were measure from geologic maps (in ArcGIS) and from topographic maps (manually). Vertical metrics were estimated from topographic maps by interpolation between contour lines.

A.4   Outputs

Analysis and interpretation of the above datasets yielded numerous outputs allowing holistic investigation of two gigantic landslides (thee Seymareh and Valley of the Rocks rock avalanches). The major outputs of the presented methodology are summarized below.

A.4.1   Terrain maps

Based on interpretation of orbital imagery, aerial photographs and DEMs, and from field observations and consultation of ancillary datasets, general terrain maps of each landslide and surrounding area were produced (Figure 2.5 and Figure 3.1). Terrain maps were the basis for interpretation of landscape impacts of the gigantic landslides and aided characterization of some metrics.

A.4.2 Structural summaries

Structural measurements made in the field and from orthorectified Landsat images were summarised on stereonets (Figure 2.14 and Figure 3.7). The summaries of structural element of each landslide allowed assessment of the degree of structural continuity of bedding, identification of preferred joint orientations and kinematic analysis. Based on these summaries, the failure mechanism and structural factors influencing landslide magnitude were determined.

A.4.3 Metrics

Summary metrics provide a complete overview of geometries and mobility for each landslide (Table 2.1 and Table 3.1).

Appendix B

Procedures for measurement and estimation of gigantic landslide geometrics

Metrics were determined from measurement, calculation and estimation on the basis of orbital imagery and SRTM and CDED DEMs (see Appendix A for detailed on datasets). Metrics were independently determined from topographic maps to confirm the accuracy of those determined by remote sensing. Discrepancies were minor where they did occur, and were most likely do to difficulty in delineating landslide features directly from 1: 50 000 scale topographic maps on the basis of contour lines and from interpolation between contour lines. Methods used for the determination of metrics are described below on the basis of metric type.

In general, accuracy was greatest for measured distances and decreased with the incorporation of additional calculation and estimation steps. The order of metrics described below roughly follows decreasing trend in accuracy because of the cumulative effects of errors from each step and, in particular, estimation of thickness of masses with only one visible surface.

B.1 Planar geometrics

B.1.1 Horizontal distances

Horizontal distances were measured directly from orthorectified Landsat images using the measure tool in ArcGIS. They were also measured directly from topographic maps and, for the Seymareh rock avalanche, directly from georeferenced geologic maps.

B.1.2 Non-horizontal distances (plunging parallel to the dip of a surface)

Non-horizontal distances were measured in the same way as horizontal distances, and a correction factor was then used to compensate for foreshortening resulting from orthographic viewing of an inclined feature. Correction factor was determined as the ratio of the down-slope length of a slope, b (it hypotenuse), dipping at θ to the horizontal length of the slope , a, where the hypotenuse is given by:

$$b / a = 1 / \cos \theta \qquad \text{(Equation 3)}$$

For slopes dipping at approximately 20° (e.g. dip of the bedding of the source area of the Seymareh rock avalanche) and 25° (e.g. dip of the bedding of the source area of the Valley of the Rocks rock

avalanche) the ratio b:a is 1.06 (or a ~6% increase in length) and 1.10 (or a ~10% increase in length), respectively.

B.2   Vertical geometrics

B.2.1   Elevations

Elevations were determined directly from DEM (SRTM or CDED) in ArcGIS. They were also estimated from topographic maps by interpolation between contour lines. In the Zagros Region, spatial and vertical accuracy of the SRTM data is ± 10 m or better and ± 12 m, respectively (Farr et al., 2007). For the CDED DEM used for the debris and source area of the Valley of the Rocks rock avalanche (82 J/13), 90% of discrete spot elevations were within 10 m (horizontal) and 5 m (vertical) of their actual positions (Centre for Topographic Information, 2005).

B.2.2   Elevations changes

Elevation changes were calculated as difference between two measured or two estimated elevations.

B.3   Calculated and estimated geometrics

B.3.1   Areas of horizontal surfaces

Areas were automatically calculated using ArcGIS from soft-copy digitized as polygons outlining features of interest.

B.3.2   Areas of non-horizontal surfaces

Areas were calculated in the same way as areas of horizontal surfaces, and the aforementioned correction factor was then used to compensate for foreshortening resulting from orthographic viewing of an inclined feature.

B.3.3   Thickness of features with only one visible surface (top or bottom)

Thicknesses were estimated by comparison of adjacent parallel topographic profiles representing the upper and lower surfaces. In the case of dipping bedding-defined failed masses, upper surfaces were represented by topographic surfaces of the flanks of the source area while lower surfaces were represented by present debris-free topographic surface within the source area. Regularity of the shape

of the failed masses (due to bedding-parallel slopes) greatly aided estimation of failed mass thickness. Evidence of topographic deviations in flanks of the source area was considered when estimating thicknesses. In the cases of in situ debris masses, upper surfaces were represented by the topographic surface of the debris while lower surfaces were represented by the present debris-free valley bottom. In cases where the compared profiles were not immediately adjacent, the valley gradient calculated immediately down valley of the debris was used to adjust for the valley slope.

B.3.4   Thicknesses of dipping features (e.g. bedding-defined failed units)

Thicknesses were estimated by calculating the distance between the base and top of the unit normal to the bedding surface. They were also measured normal to major surfaces by direct comparison of adjacent topographic profiles across the lower and upper surfaces of on interest by plotting profiles together.

B.3.5   Volume

Volumes were calculated by combining calculated horizontal surface area and estimated vertical thickness (e.g. debris) or by combining calculated non-horizontal area and estimated thickness of a dipping feature (e.g. failed units). Where source areas showed major variation in stratigraphic position of base or in likely pre-failure topographic surface, the source area was divided in corresponding units of approximately constant thickness and the volume calculated by using measured area corrected for dip and estimated thickness for each unit. Where debris showed major topographic and/or geomorphic variation, debris area was divided into corresponding geomorphic units and the volume calculated by using measured area and estimated thickness for each unit. Uncertainty in volume estimation was greater for debris than for source areas due to very regular geometry of the latter.

B.3.6   Bulking

Bulking is the volume increase resulting from dilation of debris during break-up and transport, and causes the in situ volume of debris to exceed that of the failed mass. Actual bulking was calculated as percent by comparing independently calculated volumes of the failed mass and debris.

For rock avalanches, bulking is typically on the order of 20%. The unbulked volume of debris was estimated by correcting the bulked volume assuming this value. Consequently, independently calculated values of failed mass and debris were more directly comparable.

Appendix C

Structural measurements collected from the source area of the

Seymareh rock avalanche, Iran

Appendix C.1: Strike and dip (using the right-hand rule) of exposed bedding in the scar by scan area location. Locations are given as easting and northing using WGS 1984 UTM Zone 38N and shown in Figure 2.7.

Location 1 745480, 3653288		Location 2 743652, 3651701		Location 3 737072, 3657461		Location 4 739589, 3658218		Location 5 739019, 3656188	
285 /	17	302 /	45	295 /	23	294 /	25	299 /	19
287 /	14	300 /	53	295 /	25	292 /	25	299 /	20
304 /	15	294 /	49	300 /	23	289 /	23	304 /	19
294 /	16	302 /	50	308 /	23	301 /	21	308 /	19
289 /	13	298 /	46	303 /	21	297 /	24	314 /	22
293 /	11	304 /	48	305 /	27	299 /	24	301 /	20
289 /	14	298 /	44	293 /	25	298 /	22	305 /	21
289 /	13	298 /	43	295 /	25	293 /	25	306 /	20
284 /	14	298 /	46	300 /	24	285 /	20	301 /	21
289 /	15	302 /	48	304 /	24	305 /	22	305 /	21
303 /	17	305 /	48	307 /	26	282 /	24	295 /	19
286 /	16	298 /	47	302 /	25	298 /	24	301 /	18
301 /	13	289 /	50	292 /	30	287 /	27	303 /	19
299 /	16	299 /	46	301 /	24	298 /	22	306 /	24
299 /	18	298 /	45	299 /	24	288 /	21	302 /	20
300 /	16	299 /	50	298 /	22	295 /	22	304 /	20
299 /	14	297 /	47	301 /	18	293 /	24	303 /	21
303 /	17	302 /	53	311 /	23	290 /	23	305 /	18
266 /	14	308 /	54	302 /	22	291 /	21	301 /	20
266 /	16	301 /	45	303 /	26	293 /	22	298 /	19
		293 /	51	294 /	22	300 /	24	297 /	19
		297 /	51	298 /	21	292 /	24	311 /	19
		299 /	51	294 /	21	293 /	23	305 /	21
		303 /	52	300 /	26	293 /	26	307 /	20
		299 /	54	302 /	21	296 /	25	304 /	19
		303 /	49	296 /	21	285 /	21	308 /	20
		303 /	50	307 /	20	292 /	21	291 /	21
		301 /	51	302 /	24	293 /	23	301 /	21
		304 /	50	297 /	22	291 /	23	297 /	21
		300 /	53	302 /	25	293 /	23	301 /	20
		305 /	46	295 /	21			310 /	20
		300 /	48	298 /	23			300 /	18
		295 /	54	299 /	21			310 /	19
		304 /	50	310 /	21			307 /	21
				308 /	21			300 /	20
				294 /	24				
				296 /	25				

Appendix C.1 continued…

Location 6 746175, 3652781		Location 7 747476, 3651008		Location 8 745079, 3654092		Location 9 750631, 3652547	
310 /	15	295 /	13	292 /	21	289 /	20
300 /	16	295 /	14	292 /	19	300 /	18
293 /	16	301 /	14	300 /	19	301 /	20
297 /	16	296 /	13	299 /	19	302 /	18
310 /	14	301 /	14	294 /	22	298 /	21
298 /	17	298 /	15	296 /	21	302 /	20
302 /	18	302 /	13	295 /	23	300 /	20
297 /	17	296 /	14	293 /	23	302 /	20
306 /	16	304 /	16	299 /	19	303 /	23
296 /	15	309 /	14	298 /	20	298 /	22
294 /	16	305 /	16	290 /	19	292 /	22
294 /	18	295 /	12	294 /	19	293 /	27
298 /	16	297 /	14	300 /	17	302 /	21
308 /	15	306 /	12	297 /	16	294 /	18
299 /	16	299 /	13	293 /	17	302 /	25
296 /	16	293 /	11	300 /	17	312 /	21
293 /	15	298 /	13	279 /	16	297 /	19
294 /	14	307 /	13	299 /	19	300 /	23
290 /	14	300 /	12	295 /	19	295 /	19
298 /	15	298 /	14	300 /	17	301 /	24
		304 /	15	294 /	20	300 /	23
		294 /	15	295 /	19	300 /	21
		300 /	13	304 /	12	296 /	20
		296 /	15	298 /	17	306 /	21
		298 /	15	303 /	16	298 /	21
		310 /	16	304 /	18	296 /	22
		297 /	15	296 /	16	304 /	21
		296 /	13	301 /	16	304 /	20
		293 /	13	302 /	19	301 /	20
		300 /	13	293 /	17	300 /	21
		305 /	16	297 /	17	301 /	19
		301 /	13	295 /	18	300 /	20
		305 /	14	298 /	17	301 /	20
		296 /	15	289 /	17	302 /	20
		298 /	16			298 /	23
		307 /	12			304 /	20
		307 /	13			302 /	20
		297 /	13			303 /	20
		302 /	13			301 /	20
		303 /	18			302 /	18

Appendix C.2: Apparent trend, length, and western most end coordinates of major lateral scarps and of joints visible in on exposed bedding surfaces in the source area as mapped form the Landsat image (n = 305). Locations are given as easting and northing using WGS 1984 UTM Zone 38N.

Easting	Northing	Length (m)	Trend (°)	Easting	Northing	Length (m)	Trend (°)	Easting	Northing	Length (m)	Trend (°)
736064	3656636	2348	32	738487	3657208	291	12	740627	3655705	167	45
736440	3656382	416	137	738530	3656474	400	30	740677	3653594	320	95
736768	3656020	396	7	738536	3658074	169	26	740701	3656231	295	16
736808	3655968	227	60	738663	3656583	232	161	740730	3653919	131	31
736835	3657205	396	111	738673	3655253	601	3	740750	3657042	215	137
736905	3657537	251	52	738697	3655217	308	128	740758	3653235	303	55
736966	3656727	211	10	738794	3656941	962	25	740790	3655834	130	79
737052	3655859	203	55	738833	3654833	559	48	740794	3656614	151	32
737137	3657594	233	170	738908	3654222	540	35	740820	3654133	467	18
737150	3657722	182	27	738921	3655553	297	136	740820	3654046	175	80
737209	3656155	219	134	738933	3657128	170	144	740844	3656252	233	55
737340	3657826	357	166	738967	3657582	244	24	740884	3655749	174	112
737373	3658696	487	90	738986	3655013	1336	6	740917	3657712	238	152
737436	3655911	276	121	739017	3654769	125	173	740951	3655050	299	67
737444	3657458	232	23	739041	3656930	225	33	740981	3657823	719	139
737449	3655470	306	17	739065	3654937	310	174	741037	3654069	1080	65
737454	3657915	586	150	739178	3656998	129	76	741039	3656916	383	147
737577	3656470	201	22	739201	3655725	264	1	741042	3656939	937	17
737580	3656823	166	55	739311	3655317	522	172	741043	3653620	514	60
737588	3655843	584	16	739317	3657248	106	39	741073	3655944	174	178
737698	3657367	566	15	739402	3656352	1206	173	741211	3654773	72	8
737709	3655577	152	30	739427	3657341	185	12	741220	3655214	188	10
737719	3656727	513	15	739449	3654841	385	42	741225	3654884	377	35
737789	3656422	351	118	739587	3654495	399	30	741244	3655744	336	127
737820	3658148	577	152	739625	3655745	384	92	741254	3656081	80	174
737827	3657381	341	53	739626	3656149	1451	1	741256	3655794	219	24
737859	3655588	163	16	739657	3656073	300	92	741259	3655444	182	97
737941	3655173	157	105	739791	3655174	817	36	741278	3656101	63	50
737959	3656727	194	128	739834	3654980	558	35	741311	3656974	184	30
737962	3658757	377	63	740159	3654522	242	130	741313	3657961	229	145
738033	3655815	354	27	740177	3657718	188	48	741444	3655995	395	165
738106	3656885	143	130	740235	3654773	108	75	741452	3656951	765	22
738121	3655145	331	21	740278	3654044	263	30	741465	3655451	128	33
738175	3658412	491	86	740325	3654679	144	134	741467	3654996	116	14
738195	3656548	205	119	740349	3653777	308	67	741501	3654907	51	90
738229	3655585	96	175	740373	3653458	268	58	741501	3655139	113	2
738256	3656190	295	41	740396	3656029	274	113	741507	3657304	143	67
738256	3656126	288	138	740427	3655590	174	44	741511	3655286	86	23
738261	3655013	283	31	740434	3654901	159	127	741553	3658118	382	158
738281	3655650	942	36	740451	3655541	193	51	741556	3655395	130	5
738309	3656566	352	20	740462	3654996	118	90	741563	3656039	242	127
738317	3657712	604	8	740482	3657554	204	140	741568	3653927	414	73
738428	3658392	510	163	740563	3654396	451	45	741580	3654918	209	32
738472	3658243	247	162	740576	3654953	160	168	741588	3657679	220	177
738481	3655313	328	135	740610	3657294	150	155	741601	3655844	280	27

Appendix C.2 continued…

Easting	Northing	Length (m)	Trend (°)	Easting	Northing	Length (m)	Trend (°)	Easting	Northing	Length (m)	Trend (°)
741671	3655809	182	177	743880	3653245	772	52	746226	3650484	245	138
741675	3654759	155	122	743919	3653192	117	174	746285	3650953	1532	7
741687	3656796	237	51	743975	3653192	142	140	746313	3650809	351	121
741696	3654810	1410	10	744175	3654072	640	86	746326	3650717	280	143
741696	3657063	552	17	744175	3653080	138	22	746372	3651050	163	50
741770	3654181	309	69	744239	3653248	171	53	746393	3651246	245	122
741777	3657712	338	41	744256	3653571	356	26	746409	3651537	228	128
741787	3657489	475	160	744355	3653156	297	10	746480	3651546	386	28
741875	3654727	596	59	744395	3653128	386	67	746484	3651866	282	34
741914	3655877	303	127	744423	3653484	231	53	746509	3652149	491	127
742026	3653737	462	69	744694	3653721	502	36	746567	3652813	603	24
742038	3655701	223	36	744787	3653296	96	48	746597	3651675	249	128
742061	3657052	608	33	744815	3653701	296	130	746621	3650260	403	42
742070	3654577	340	47	744826	3654122	188	37	746966	3653550	1056	174
742074	3656990	181	84	745020	3654316	308	29	746966	3653581	131	17
742113	3654140	407	54	745064	3654197	202	158	746991	3654163	414	177
742115	3654943	338	2	745097	3652008	423	3	746994	3651938	482	6
742122	3655358	1433	10	745140	3653392	243	126	746998	3654239	612	16
742267	3654565	246	52	745140	3653432	156	48	747038	3653648	304	140
742290	3656982	187	149	745158	3654009	200	131	747128	3652429	512	101
742443	3654570	173	55	745177	3654128	277	28	747145	3651738	649	4
742481	3654546	251	93	745267	3652162	316	8	747166	3650869	363	40
742505	3654407	443	91	745277	3653502	268	16	747300	3652799	241	120
742521	3655187	753	36	745280	3651564	521	48	747303	3651029	1736	93
742523	3654009	212	44	745283	3653452	112	128	747303	3651534	366	108
742567	3653877	244	76	745296	3652688	84	132	747340	3651344	160	108
742623	3654849	245	101	745302	3652757	232	14	747413	3652924	599	144
742711	3654189	144	88	745384	3653240	425	120	747460	3653395	107	172
742822	3654584	180	60	745392	3652638	74	85	747472	3653438	117	39
742871	3654305	168	176	745408	3653426	211	37	747488	3652453	222	95
742899	3654817	54	36	745440	3652093	123	15	747530	3653289	115	53
742995	3654325	281	139	745458	3652575	320	178	747537	3651297	79	46
743067	3654897	381	50	745481	3651114	226	123	747592	3653594	206	148
743157	3653808	396	130	745490	3653828	268	33	747596	3651799	302	93
743175	3653925	148	3	745503	3652674	262	29	747611	3651310	89	90
743290	3654120	328	139	745608	3653694	165	34	747758	3652000	494	101
743295	3654154	258	29	745633	3652907	193	8	747793	3651394	119	91
743459	3654601	211	33	745643	3650692	597	34	747835	3650576	483	97
743546	3653864	96	86	745648	3652339	385	178	747835	3651631	185	110
743654	3653966	243	24	745668	3654200	323	172	747852	3650811	1169	93
743660	3653850	231	175	745692	3652350	275	144	747879	3650696	347	100
743662	3653552	327	170	745715	3651481	591	44	747887	3651367	241	135
743730	3653677	406	160	745865	3651921	167	0	747920	3652317	648	101
743742	3653753	728	42	745966	3650302	639	28	747925	3651425	655	95
743755	3653186	230	175	745996	3651248	434	7	747925	3651771	206	109
743764	3652466	276	174	746109	3651725	370	19	747942	3652117	392	96
743765	3654351	323	39	746164	3650392	273	149	747983	3651445	166	35
743826	3652239	144	44	746201	3652699	572	175	748171	3651665	1138	91

Appendix C.2 continued…

Easting	Northing	Length (m)	Trend (°)
748206	3652071	509	70
748251	3652235	919	88
748420	3653086	252	83
748445	3650450	224	140
748489	3651802	1038	60
748641	3650555	240	128
748754	3650013	236	134
748779	3651929	300	142
748895	3651308	613	91
749062	3653328	345	133
749224	3653412	474	3
749364	3648673	308	32
749514	3649103	148	169
749576	3649248	260	35
749707	3652200	471	107
749743	3649493	226	10
749762	3651863	751	92
749772	3651674	619	90
749839	3649964	651	33
749854	3649755	178	0
749865	3651375	392	86
750124	3652354	462	93
750256	3650563	899	32
751092	3651823	266	170
751170	3651957	1108	12
751460	3653111	298	8

Appendix D

Modified Geological Strength Index (GSI) for the geologic sequence of Kabir Kuh

Appendix D.1: Description of modification of the GSI for the geologic sequence of Kabir Kuh.

Hoek et al.'s (2005) extension of the Geological Strength Index (GSI) for at surface, lithologically varied, tectonically undisturbed rock-masses (Hoek et al., 2005, Figure 10) was adapted to for the moderately disturbed limestone-mud rock sequence present in Kabir-Kuh (e.g. Asmari to Sarvak Formations in Figure 2.3. The modified GSI chart is presented in Appendix D.2. Values determined for units of the failed sequence of the Seymareh rock avalanche are represented in Figure 2.9.

In general, GSI charts are applied based on description of lithology and structure, and of the surface condition of discontinuities. Hoek et al.'s (2005) extension of the GSI was developed for stratigraphically variable classic sedimentary lithologies (mainly conglomerates, sandstone, siltstone and shale). Consequently, composition and structure consider by Hoek et al. (2005) are similar to those present in the limestone-mud rock sequences of Kabir Kuh. Modification of the GSI was achieved mainly through substitution of competent (limestone) and incompetent (shale) units present in Kabir Kuh for competent (conglomerate / sandstone) and incompetent (siltstone / shale) units, respectively, described by Hoek et al. (2005). The overall form of the Hoek et al. (2005) GSI was maintained with columns considering non-interbedded competent units (strongest), competent-incompetent interbedded units (intermediate strength) and non-interbedded incompetent units (weakest). Hoek et al. (2005) described only a single composition/structure condition for non-interbedded competent units. Due to the variation of strength of competent (predominantly limestone) units in the sequence of Kabir Kuh, the modified GSI differentiates between three classes of non-interbedded competent unit (K1 – K3) on the basis of bedding thickness. Classes defined for competent-incompetent interbedded units and non-interbedded incompetent units closely follow Hoek et al. (2005)

Surface condition of discontinuities is largely affected by composition and structure. Surface conditions generally decrease (from very good to very poor), therefore, with weakening composition and structure. In the modified GSI, position of classes in the' composition/structure-surface condition' space broadly follow those of Hoek et al. (2005).

87

Midpoints of each zone were used to quantitatively represent the relative rock-mass strength differences between units (Figure 2.9). Because of anisotropy of the rock-mass, the GSI was not used for stability assessment (c.f. Marinos et al., 2005).

Appendix D.2: Modified GSI for the limestone-mud rock sequence of Kabir Kuh.

Appendix E

Radiocarbon analysis report from IsoTrace Radiocarbon Laboratory

October 23, 2007

Submitter: N.Roberts, Dept of Earth and Environmental Sciences, Univ of Waterloo, Waterloo ON

Both samples were screened with a 1.0mm grid and the remaining silt and sand was removed by untrasonic cleaning or water flotation. The 1.0mm fraction of TO-13446 contained rootlets which were removed manually under a stereo miscroscope.

These results are the average of 2 separate analyses (normal precision) and are corrected for natural and sputtering isotope fractionation, using the measured $^{13}C/^{12}C$ ratios. The sample ages are quoted as uncalibrated conventional radiocarbon dates in years before present (BP), using the Libby ^{14}C meanlife of 8033 years. The errors represent 68.3 % confidence limits.

| Sample Identification	Description	Weight used (mg)	IsoTrace Lab number	$^{14}C/^{12}C$ (pMC)	Age (years BP)
NJR-SM-R001	charcoal (>1.0mm fraction)	827	TO-13445	33.82 ± 0.36	8710 ± 80
NJR-SM-R005	charcoal (>1.0mm fraction)	143	TO-13446	115.19 ± 0.81	

23-Oct-07

TO-13445 NJR-SM-R001 charcoal

Radiocarbon result : 33.82 ± .36 pMC

All solutions, with a probability of 50% or greater for the calibrated age
of this radiocarbon date, have been calculated from the dendro calibration
data. The 68% and 95% confidence intervals, which are the 1σ and 2σ limits
for a normal distribution, are also given. A probability of 100% means the
radiocarbon date intersects the dendro calibration curve at this age.
All results are rounded to the nearest multiple of 5 years.

No.	Probability	cal Age	68.3 % c.i.	95.5 % c.i.
1	100 %	7720 cal BC	7830 BC - 7595 BC	7990 BC - 7580 BC

Calibrated with the standard data set from:
 INTCAL04 Terrestrial Radiocarbon Age Calibration, 0-26 cal kyr BP
 P.J.Reimer et al.; Radiocarbon 46#3 (2004) p1029
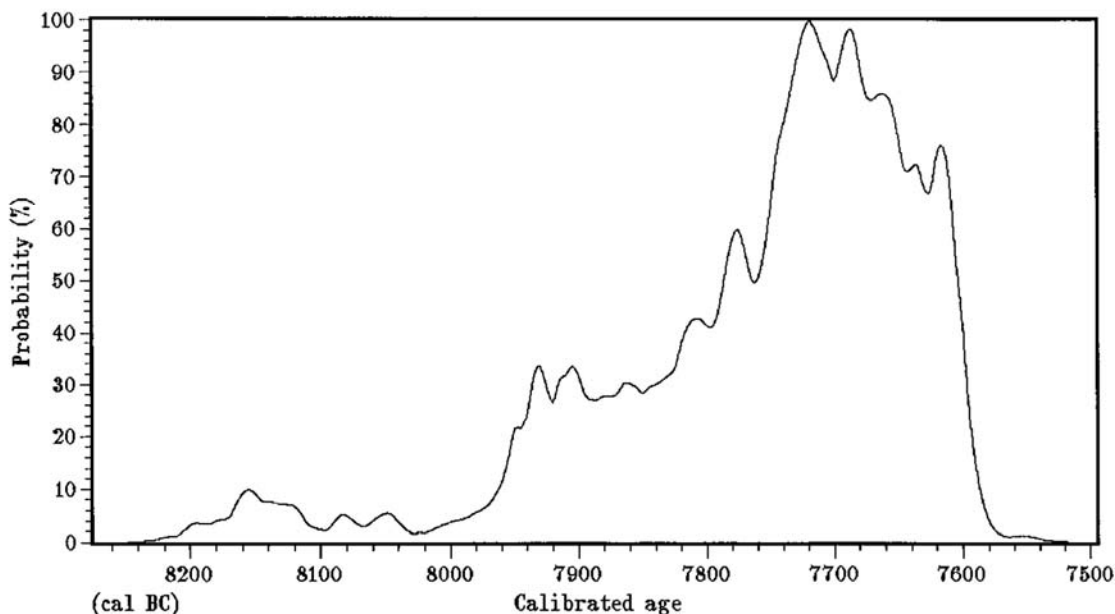
90
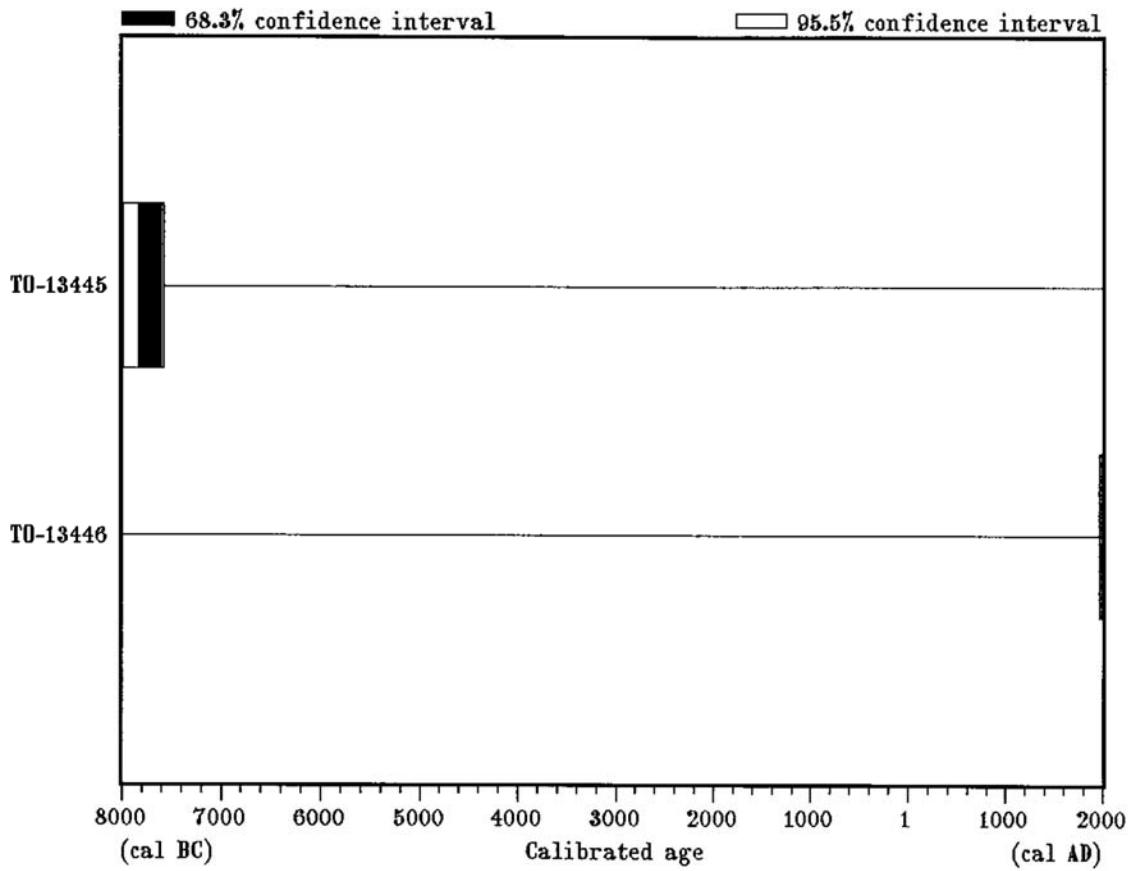
Appendix F

Structural measurements collected from the source area of the

Valley of the Rocks rock avalanche, Canada

Appendix F.1: Strike and dip (using the right-hand rule) of exposed bedding in the scar by scan area location. Locations are given as easting and northing using NAD 1983 UTM Zone 11N and shown in Figure 3.1.

Location 1 596647, 5646214		Location 2 596046, 5647433		Location 3 595857, 5647652		Location 4 594904, 5648867		Location 4 continued	
145 /	29	150 /	32	158 /	28	153 /	24	154 /	25
149 /	30	153 /	34	153 /	26	157 /	23	160 /	28
140 /	30	152 /	28	150 /	26	148 /	24	156 /	25
144 /	29	148 /	30	143 /	28	148 /	27	154 /	28
151 /	26	153 /	27	144 /	36	158 /	27	153 /	25
149 /	31	152 /	31	151 /	41	155 /	26	151 /	25
150 /	27	148 /	30	150 /	36	158 /	24	153 /	25
147 /	29	153 /	29	146 /	33	159 /	26	149 /	25
145 /	26	150 /	29	143 /	30	153 /	25	155 /	23
140 /	29	148 /	28	149 /	31	161 /	25	152 /	24
144 /	27	154 /	28	144 /	32	155 /	25	159 /	23
147 /	28	149 /	29	148 /	34	160 /	22	156 /	29
145 /	30	151 /	30	145 /	24	160 /	24	154 /	24
150 /	29	154 /	27	146 /	30	160 /	24	154 /	26
142 /	29	153 /	30	150 /	35	162 /	26	160 /	26
156 /	32	150 /	30			156 /	27	153 /	24
160 /	29	142 /	26			155 /	24	158 /	28
148 /	30	155 /	30			154 /	26		
153 /	26	153 /	29			154 /	25		
152 /	27	155 /	28			156 /	27		
145 /	30	140 /	30			158 /	26		
151 /	29	144 /	35			160 /	24		
156 /	28	148 /	32			148 /	25		
150 /	27	142 /	29			142 /	31		
145 /	31					148 /	26		

Appendix F.1 continued…

Location 5 594856, 5647728		Location 6 594605, 5648069		Location 7 595445, 5646968	
145 /	20	132 /	20	140 /	20
138 /	21	144 /	19	141 /	19
142 /	24	135 /	18	138 /	20
140 /	21	130 /	21	147 /	20
136 /	20	145 /	20	139 /	21
137 /	24	142 /	21	140 /	20
136 /	20	143 /	20	140 /	26
131 /	19	128 /	20	141 /	20
144 /	19	131 /	19	137 /	23
141 /	20	135 /	21	134 /	22
141 /	20	135 /	22	143 /	22
145 /	22	144 /	20	141 /	25
144 /	28	140 /	22	142 /	21
140 /	24	133 /	20	139 /	18
148 /	19	132 /	24	143 /	23
150 /	24	141 /	24	150 /	33
143 /	23	139 /	22	150 /	24
140 /	26	140 /	25	152 /	25
150 /	27	138 /	21	150 /	23
141 /	24	135 /	19	154 /	22
139 /	24	136 /	21	147 /	25
138 /	23	130 /	20	148 /	22
134 /	25	136 /	20	142 /	21
134 /	22	134 /	20	144 /	22
139 /	21	139 /	20	141 /	24
146 /	19	141 /	21	146 /	20
145 /	18	141 /	23	143 /	25
144 /	17	144 /	22	144 /	22
150 /	24	139 /	24	142 /	21
150 /	21	132 /	20	145 /	22
154 /	21	140 /	20		
154 /	20				

References

Alavi, M., 2004. Regional stratigraphy of the Zagros fold-thrust belt of Iran and its proforeland evolution. American Journal of Science 304 1-20.

Alavi, M., 2007. Structures of the Zagros fold-thrust belt in Iran. American Journal of Science 307, 1064-1095.

Alavi, M., and Mahdavi, M.A., 1994. Stratigraphy and structures of the Nahavand region in western Iran, and their implications for the Zagros tectonics. Geological Magazine 131, 43-47.

Ambraseys, N.N., and Melville, C.P., 1982. A history of Persian earthquakes. Cambridge University Press, New York, 219 p.

Amirshahkarami, M., Vaziri-Moghaddam, H., and Taheri, A., 2007. Sedimentary facies and sequence stratigraphy of the Asmari Formation at Chaman-Bolbol, Zagros Basin, Iran. Journal of Asian Earth Sciences 29, 947-959.

Ashjari, J., and Raeisi, E., 2006. Influences of anticlinal structure on regional flow, Zagros, Iran. Journal of Cave and Karst Studies 68, 118-129.

Bahroudi, A., and Koyi, H.A., 2004. Tectono-sedimentary framework of the Gachsaran Formation in the Zagros foreland basin. Marine and Petroleum Geology 21, 1295-1310.

Beetham, R.D., McSaveney, M.J., and Read, S.A.L., 2002. Four extremely large landslides in New Zealand, in: Rybar, J., Stemberk, J., and Wagner, P. (Eds.), Proceedings of the First European conference on Landslides, Prague, Czech Republic. A.A. Balkema Publishers, Lisse, pp. 97-102.

Benko, B., and Stead, D., 1998. The Frank slide: a reexamination of the failure mechanism. Canadian Geotechnical Journal 35, 299-311.

Berberian, M., 1995. Master "blind" thrust faults hidden under the Zagros folds: active basement tectonics and surface morphotectonics. Tectonophysics 241, 193-224.

Berberian, M., and King, G.C.P., 1981. Towards a paleogeography and tectonic evolution of Iran. Canadian Journal of Earth Sciences 18, 210-265.

Blanc, E.J.P., Allen, M.B., Inger, S., and Hassani, H., 2003. Structural styles in the Zagros simple folded zone, Iran. Journal of the Geological Society of London 160, 401-412.

Bown, T.M., Love, J.D., Crandell, D.R., Miller, C.D., Glicken, H.X., Christiansen, R.L., and Newhall, C.G., 1985. Catastrophic debris avalanche from ancestral Mount Shasta Volcano, California: discussion and reply. Geology 13, 79-80.

Burbank, D.W., and Anderson, R.S., 2001. Tectonic Geomorphology. Blackwell Science, Oxford, 274 p.

Centre for Topographic Information, 2004, Landsat ETM+ scene LE7043024_0102_010923, Geomatic Canada, 09/23/2001.

Centre for Topographic Information, 2005, CDED1-082J13_BC digital metadata, Natural Resources Canada

Chen Rou-Fei, Chan Yu-Chang, Angelier, J., Hu Jyr-Ching, Huang Chung, Chang Kuo-Jen, and Shih Tian-Yuan, 2005. Large earthquake-triggered landslides and mountain belt erosion: the Tsaoling case, Taiwan. Geoscience 337, 1164-1172.

Choi, B.H., Pelinovsky, E., Kim, K.O., and Lee, J.S., 2003. Simulation of the trans-oceanic tsunami propagation due to the 1883 Krakatau volcanic eruption. Natural Hazards and Earth System Sciences 3, 321-332.

Cosgrove, J.W., and Ameen, M.S., 2000. A comparison of the geometry, spatial organization and fracture patterns associated with forced folds and buckle folds. Geological Society Special PublicationS 169, 7-21.

Cruden, D.M., 1976. Major rock slides in the Rockies. Canadian Geotechnical Journal 13, 8-20.

Cruden, D.M., 1985. Rock Slope Movements in the Canadian Cordillera. Canadian Geotechnical Journal 22, 528-540.

Cruden, D.M., and Eaton, T.M., 1987. Reconnaissance of rockslide hazards in Kananaskis country, Alberta. Canadian Geotechnical Journal 24, 414-429.

Cruden, D.M., and Hu, X.Q., 1988. Basic friction angles of carbonate rocks from Kananaskis country, Canada. Bulletin of Engineering Geology and the Environment 31, 55-59.

Cruden, D.M., and Hu, X.Q., 1999. The shapes of some mountain peaks in the Canadian Rockies. Earth Surface Processes and Landforms 24, 1229-1241.

de Morgan, J., 1895. Mission scientifique en Perse, v. 2. Paris, 331 p.

Deplazes, G., Anselmetti, F.S., and Hajdas, I., 2007. Lake sediments deposited on the Flims rockslide mass: The key to date the largest mass movement of the Alps. Terra Nova 19, 252-258.

deWit, R., and McLaren, D.J., 1950. Devonian sections in the Rocky Mountains between Crowsnest Pass and Jasper, Alberta. Geological Survey of Canada Paper 50-23.

Dishaw, H.E., 1967. Massive Landslides. Photogrammetric Engineering 33, 603-608.

Donath, F.A., and Parker, R.B., 1964. Folds and folding. Geological Society of America Bulletin 75, 45-62.

Duffy, P.J.B., 1967. The Valley of the Rocks. Canadian Alpine Journal 60, 88-90.

Einsele, G., 2000. Sedimentary basins: evolution, facies, and sediment budget. Springer, Berlin, 792 p.

Eisbacher, G.H., 1979. Cliff collapse and rock avalanches (sturzstroms) in the Mackenzie Mountains, northwestern Canada. Canadian Geotechnical Journal 16, 309-334.

Evans, S.G., 1989. Rock Avalanche Run-up Record. Nature 340, 271-271.

Evans, S.G. 1992. High-magnitude low frequency catastrophic landslides in British Columbia, in: Proceedings, British Columbia Geological Survey Workshop on Geologic Hazards in British Columbia. B.C. Ministry of Energy Mines and Petroleum Resources Open-File 1992-15, 71-98.

Evans, S.G. 2001. Landslides, in: Brooks, G.R. (Ed.), Geological Hazards in Canada: a Synthesis. Geological Survey of Canada Bulletin 548, pp. 43-79.

Evans, S.G., Hungr, O., and Enegren, E.G., 1994. The Avalanche Lake rock avalanche, Mackenzie Mountains, Northwest Territories, Canada: description, dating, and dynamics. Canadian Geotechnical Journal 31, 749-768.

Falcon, N.L., 1969. Problems of the relationship between surface structure and deep displacements illustrated by the Zagros range. Geological Society Special Publications 3, 9-22.

Falcon, N.L., 1974. Southern Iran: Zagros Mountains, in: Spencer, A.M. (Ed.), Mesozoic-Cenozoic orogenic belts. Scottish Academic Press, Edinburgh, pp. 199-211.

Farr, T.G., Rosen, P.A., Caro, E., Crippen, R., Duren, R., Hensley, S., Kobrick, M., Paller, M., Rodriguez, E., Roth, L., Seal, D., Shaffer, S., Shimada, J., Umland, J., Werner, M., Oskin, M.,

Burbank, D., and Alsdorf, D., 2007. The Shuttle Radar Topography Mission. Reviews in Geophysics 45, article RG2004.

Gee, M.J.R., Uy, H.S., Warren, J., Morley, C.K., and Lambiase, J.J., 2007. The Brunei slide: A giant submarine landslide on the North West Borneo Margin revealed by 3D seismic data. Marine Geology 246, 9-23.

Geldsetzer, H., de Mille, G., Sangster, D.F., Chung, C.F., McDonald, J.A., and Jonasson, I.R., 1986. The Upper Devonian Palliser Formation, Rocky Mountains, British Columbia and Alberta: geochemistry and general geology. Geological Survey of Canada Open File 1021, 52.

Ghasemi-Nejad, E., Hobbi, M.H., and Schioler, P., 2006. Dinoflagellate and foraminiferal biostratigraphy of the Gurpi Formation (upper Santonian-upper Maastrichtian), Zagros Mountains, Iran. Cretaceous Research 27, 828-835.

Ghobadi, M.H., Khanlari, G.R., and Djalaly, H., 2005. Seepage problems in the right abutment of the Shahid Abbaspour Dam, southern Iran. Engineering Geology 82, 119-126.

Gholipour, A.M., 1998. Patterns and structural positions of productive fractures in the Asmari reservoirs, Southwest Iran. Journal of Canadian Petroleum Technology 37, 44-50.

Guthrie, R.H., and Evans, S.G., 2007. Work, persistence, and formative events: The geomorphic impact of landslides. Geomorphology 88, 266-275.

Hancox, G.T., and Perrin, N.D., 1994. Green Lake Landslide: a very large ancient rock slide in glaciated terrain, Fiordland, New Zealand. Lower Hutt, New Zealand, Institute of Geological & Nuclear Sciences Report 93/18, 50.

Harrison, J.V., 1945. South-west Persia: a survey of Pish-i-Kuh in Luristan. Geographical Journal 108, 55-71.

Harrison, J.V., and Falcon, N.L., 1934. Collapse structures. The Geological Magazine 71, 529-539.

Harrison, J.V., and Falcon, N.L., 1936. Gravity collapse structures and mountain ranges as exemplified in southwestern Iran. The Quarterly journal of the Geological Society 92, 91-102.

Harrison, J.V., and Falcon, N.L., 1937. The Saidmarreh landslip, southwest Iran. Geographical Journal 89, 42-47.

Harrison, J.V., and Falcon, N.L., 1938. An ancient landslip at Saidmarreh in southwestern Iran. Journal of Geology 46, 296-309.

Hayashi, J.N., and Self, S., 1992. A Comparison of pyroclastic flow and debris avalanche mobility. Journal of Geophysical Research-Solid Earth 97, 9063-9071.

Hessami, K., Koyi, H.A., Talbot, C.J., Tabasi, H., and Shabanian, E., 2001. Progressive unconformities within an evolving foreland fold-thrust belt, Zagros Mountains. Journal of the Geological Society 158, 969-981.

Hessami, K., Nilforoushan, F., and Talbot, C.J., 2006. Active deformation within the Zagros Mountains deduced from GPS measurements. Journal of the Geological Society 163, 143-148.

Heuberger, H., Masch, L., Preuss, E., and Schrocker, A., 1984. Quaternary landslides and rock fusion in Central Nepal and in the Tyrolean Alps. Mountain Research and Development 4(4), 345-362.

Hewitt, K., 1998. Catastrophic landslides and their effects on the Upper Indus streams, Karakoram Himalaya, northern Pakistan. Geomorphology 26, 47-80.

Hodge, R.A.L., and Freeze, R.A., 1977. Groundwater flow systems and slope stability. Canadian Geotechnical Journal 14, 466-476.

Hoek, E., Marinos, P.G., and Marinos, V.P., 2005. Characterisation and engineering properties of tectonically undisturbed but lithologically varied sedimentary rock masses. International Journal of Rock Mechanics and Mining Sciences 42, 277-285.

Hsü, K.J., 1975. Catastrophic debris streams (sturzstroms) generated by rockfalls. Geological Society of America Bulletin 86, 129-140.

Iran Water and Resources Power Development Company. Unpublished data. Long-term suspended sediment yield for the Seymareh River at Nazarabad hydrometric station (1971-1994).

Jackson, J.A., 1980. Reactivation of basement faults and crustal shortening in orogenic belts. Nature 283, 343-346.

Jackson, L.E., Jr., 1980. Glacial history and stratigraphy of the Alberta portion of the Kananaskis Lakes map area. Canadian Journal of Earth Sciences 17, 459-477.

James, G.A., and Wynd, J.G., 1965. Stratigraphic nomenclature of Iranian Oil Consortium Agreement Area. Bulletin of the American Association of Petroleum Geologists 49, 2182-2245.

Kent, P.E., 1966. The transport mechanism in catastrophic rock falls. Journal of Geology, 74, 79-83.

Kojan, E., and Hutchinson, J.N., 1978. Mayunmarca rockslide and debris flow, Peru, in: Voight, B. (Ed.), Rockslides and rock avalanches v. 1. Natural Phenomena, v. 1, Developments in Geotechnical Engineering. Elsevier Scientific Publishing Company, Amsterdam, pp. 315-361.

Korup, O., 2004. Geomorphometric characteristics of New Zealand landslide dams. Engineering Geology 73, 13-35.

Korup, O., Clague, J.J., Hermanns, R.L., Hewitt, K., Strom, A.L., and Weidinger, J.T., 2007. Giant landslides, topography, and erosion. Earth and Planetary Science Letters 261, 578-589.

Korup, O., Strom, A.L., and Weidinger, J.T., 2006. Fluvial response to large rock-slope failures: Examples from the Himalayas, the Tien shan, and the southern Alps of New Zealand. Geomorphology 78, 3-21.

Lay, T., Kanamori, H., Ammon, C.J., Nettles, M., Ward, S.N., Aster, R.C., Beck, S.L., Bilek, S.L., Brudzinski, M.R., Butler, R., DeShon, H.R., Ekstrom, G., Satake, K., Sipkin, S., and Hanson, B., 2005. The great Sumatra-Andaman earthquake of 26 December 2004. Science 308, 1127-1133.

Leech, G.B., 1979. Geological map of Kananaskis Lakes, west half, British Columbia and Alberta (NTS 82J w). Geological Survey of Canada Open File 634.

Legros, F., 2002. The mobility of long-runout landslides. Engineering Geology 63, 301-331.

Lucchitta, B.K., 1978. A large landslide on Mars. Geological Society of America Bulletin 89, 1601-1609.

Lucchitta, B.K., 1979. Landslides in Valles Marineris, Mars. Journal of Geophysical Research 84, 8097-8113.

Luckman, B.H., and Osborn, G.D., 1979. Holocene glacier fluctuations in the middle Canadian Rocky Mountains. Quaternary Research 11, 52-77.

Macleod, J.H., 1970. Kabīr Kūh. Iran Oil Operating Companies, Geological and Exploration Division Map 20812W, scale 1:100 000, 1 sheet.

Marinos, V., Marinos, P., and Hoek, E., 2005. The geological strength index: Applications and limitations. Bulletin of Engineering Geology and the Environment 64, 55-65.

McClusky, S., Reilinger, R., Mahmoud, S., Ben Sari, D., and Tealeb, A., 2003. GPS constraints on Africa (Nubia) and Arabia plate motions. Geophysical Journal International 155, 126-138.

McLaren, D.J., 1955. Devonian formations in the Alberta Rocky Mountains between Bow and Athasbasca Rivers. Geological Survey of Canada Bulliten 35, 59.

McLellan, P.J., and Kaiser, P.K., 1984. The Rockslide Pass rock avalanche in the Mackenzie Mountains, N.W.T. Canadian Geotechnical Conference, Toronto, Canada, 37, 135-140.

McQuarrie, N., 2004. Crustal scale geometry of the Zagros fold-thrust belt, Iran. Journal of Structural Geology 26, 519-535.

McQuillan, H., 1973. Small-scale fracture density in Asmari Formation of Southwest Iran and its relation to bed thickness and structural setting. American Association of Petroleum Geologists Bulletin 57, 2367-2385.

McQuillan, H., 1974. Fracture patterns on Kuh-e Asmari Anticline, Southwest Iran: American Association of Petroleum Geologists Bulletin 58, 236-246.

McQuillan, H., 1985. Fracture-controlled production from the Oligo-Miocene Asmari Formation in Gachsaran and Bibi Hakimeh fields, Southwest Iran, in Roehl, P.O., and Choquette, P.W. in. (Eds.), Carbonate petroleum reservoirs. Springer, Berlin, pp. 513-523.

Meijer Drees, N.C., Johnston, D.I., and Richards, B.C., 1993. The Devonian Palliser Formation and its equivalents, southern Alberta, Canada. Geological Survey of Canada Open File 2698, 98.

Melosh, H.J., 1979. Acoustic fluidization: a new geologic process?. Journal of Geophysical Research 84, 7513-7520.

Milliman, J.D., and Syvitski, J.P.M., 1992. Geomorphic/tectonic control of sediment discharge to the ocean - the importance of small mountainous rivers. Journal of Geology 100, 525-544.

Mohseni, H., and Al-Aasm, I.S., 2004. Tempestite deposits on a storm-influenced carbonate ramp; an example from the Pabdeh Formation (Paleogene), Zagros Basin, SW Iran. Journal of Petroleum Geology 27, 163-178.

Motiei, H., 2003. Geology of Iran, Stratigraphy of the Zagros. Geological Survey or Iran, p. 583.

Murris, R.J., 1980. Middle East; stratigraphic evolution and oil habitat. American Association of Petroleum Geologists Bulletin 64, 597-618.

NASA Landsat Program, 2002a, Landsat ETM+ scene L720000401_20000630_08, USGS, Sioux Falls, 5/29/2000.

NASA Landsat Program, 2002b, Landsat ETM+ scene L7CPF20010101_20010331_06, USGS, Sioux Falls, 03/20/2001.

Oberlander, T., 1965. The Zagros streams: a new interpretation of transverse drainage in an orogenic zone: New York, Syracuse University Press.

Oberlander, T.M., 1985. Origin of drainage transverse to structures in orogens, in: Morisawa, M., and Hack, J.T. (Eds.), Tectonic Geomorphology, The Binghamton Symposia in Geomorphology International Series, no. 15. Allen & Unwin, Boston, pp. 155-182.

Peart, M., 1991. The Kaiapit Landslide: events and mechanisms. Quarterly Journal of Engineering Geology 24, 399-411.

Philip, H., and Ritz, J.-F., 1999. Gigantic paleolandslide associated with active faulting along the Bogd Fault (Gobi-Altay, Mongolia). Geology 27, 211-214.

Pollet, N., and Schneider, J.L.M., 2004. Dynamic disintegration processes accompanying transport of the Holocene Flims sturzstrom (Swiss Alps). Earth and Planetary Science Letters 221, 433-448.

Price, N.J., and Cosgrove, J.W., 1990. Analysis of geological structures. Cambridge University Press, New York, 502 p.

Quantin, C., Allemand, P., and Delacourt, C., 2004. Morphology and geometry of Valles Marineris landslides. Planetary and Space Science 52, 1011-1022.

Rutter, N.W., 1972. Geomorphology and multiple glaciation in the area of Banff, Alberta. Geological Survey of Canada Bulletin 206, 45.

Scheidegger, A.E., 1973. On the prediction of the reach and velocity of catastrophic landslides. Rock Mechanics 5, 231-236.

Schmidt, K.M. and Montgomery, D.R., 1995. Limits to relief. Science 270(5236), 617-620.

Schuster, R.L., and Alford, D., 2004. Usoi landslide dam and Lake Sarez, Pamir Mountains, Tajikistan. Environmental and Engineering Geoscience 10, 151-168.

Schuster, R.L., and Highland, L.M., 2007. Overview of the effects of mass wasting on the natural environment. Environmental and Engineering Geoscience 13, 25-44.

Sepehr, M., and Cosgrove, J.W., 2004. Structural framework of the Zagros fold-thrust belt, Iran. Marine and Petroleum Geology 21, 829-843.

Setudehnia, A., 1978. The Mesozoic sequence in South-west Iran and adjacent areas. Journal of Petroleum Geology 1, 3-42.

Setudehnia, A., and Perry, J.T., 1967a. Dāl Parrī. Iran Oil Operating Companies, Geological and Exploration Division Map 20816E, scale 1:100 000, 1 sheet.

Setudehnia, A., and Perry, J.T., 1967b. Dehlurān. Iran Oil Operating Companies, Geological and Exploration Division Map 20816W, scale 1:100 000, 1 sheet.

Shoaei, Z., and Ghayoumian, J., 2000. Seimareh landslide, western Iran: one of the world's largest complex landslides. Landslide News 13, 23-27.

Shreve, R.L., 1968,.The Blackhawk landslide. Geological Society of America Special Paper 108, 47.

Skempton, A.W., 1966. Some observations on tectonic shear zones. Congress of the International Society of Rock Mechanics, Lisbon, Portugal, 329-335.

SPOT image, 1994, SPOT 5 scene 499700201200.

Stephenson, B., J., Koopman, A., Hillgartner, K., McQuillan, H., Bourne, S., Noad, J., J., and Rawnsley, K., 2007. Structural and stratigraphic controls on fold-related fracturing in the Zagros Mountains, Iran: implications for reservoir development. Geological Society, London, Special Publications 270, 1-21.

Stevens, L.R., Ito, E., Schwalb, A., and Wright, H.E., 2006. Timing of atmospheric precipitation in the Zagros Mountains inferred from a multi-proxy record from Lake Mirabad, Iran. Quaternary Research 66, 494-500.

Stevens, L.R., Wright, H.E., Jr., and Ito, E., 2001. Proposed changes in seasonality of climate during the Lateglacial and Holocene at Lake Zeribar, Iran. The Holocene 11(6), 747-755.

Stöcklin, J., 1968. Structural history and tectonics of Iran: a review. American Association of Petroleum Geologists Bulletin 52, 1229-1258.

Strom, A.L., 1998. Giant ancient rockslide and rock avalanche in the Tien Shan Mountains, Kyrgyzstan. Landslide News 11, 20-23.

Strom, A.L., and Korup, O., 2006. Extremely larger rockslides and rock avalanches in the Tien Shan Mountains, Kyrgyzstan. Landslides 3, 125-136.

Takin, M., Akbari, Y., and Macleod, J.H., 1970. Pul-e Dukhtar. Iran Oil Operating Companies, Geological and Exploration Division Map 20812E, scale 1:100 000, 1 sheet.

Talling, P.J., Wynn, R.B., Masson, D.G., Frenz, M., Cronin, B.T., Schiebel, R., Akhmetzhanov, A.M., Dallmeier-Tiessen, S., Benetti, S., Weaver, P.P.E., Georgiopoulou, A., Zuhlsdorff, C., and Amy, L.A., 2007. Onset of submarine debris flow deposition far from original giant landslide. Nature 450, 541-544.

Tatar, M., Hatzfeld, D., and Ghafory-Ashtiany, M., 2004. Tectonics of the central Zagros (Iran) deduced from microearthquake seismicity. Geophysical Journal International 156, 255-266.

Vaziri-Moghaddam, H., Seyrafian, A., and Taraneh, P., 2002. Biofacies and sequence stratigraphy of the Eocene succession, at Hamzeh-Ali area, north-central Zagros, Iran. Carbonates and Evaporites 17, 60-67.

Vernant, P., and Chery, J., 2006. Mechanical modelling of oblique convergence in the Zagros, Iran. Geophysical Journal International 165, 991-1002.

Vernant, P., Nilforoushan, F., Hatzfeld, D., Abbassi, M.R., Vigny, C., Masson, F., Nankali, H., Martinod, J., Ashtiani, A., Bayer, R., Tavakoli, F., and Chery, J., 2004. Present-day crustal deformation and plate kinematics in the Middle East constrained by GPS measurements in Iran and northern Oman. Geophysical Journal International 157, 381-398.

Voight, B., and Pariseau, W.G., 1978. Rockslides and avalanches: an introduction, in: Voight, B. (Ed.), Rockslides and rock avalanches v. 1. Natural Phenomena, v. 1, Developments in Geotechnical Engineering. Elsevier Scientific Publishing Company, Amsterdam, pp. 1-67.

Walpersdorf, A., Hatzfeld, D., Nankali, H., Tavakoli, F., Nilforoushan, F., Tatar, M., Vernant, P., Chery, J., and Masson, F., 2006. Difference in the GPS deformation pattern of north and central Zagros (Iran). Geophysical Journal International 167, 1077-1088.

Watson, R.A., and Wright, H.E., Jr., 1969. The Saidmarreh landslide, Iran. Geological Society of America Special Paper 123, 115-139.

Wennberg, O.P., Svana, T., Azizzadeh, M., Aqrawi, A.M.M., Brockbank, P., Lyslo, K.B., and Ogilvie, S., 2006. Fracture intensity vs. mechanical stratigraphy in platform top carbonates: the

Aquitanian of the Asmari Formation, Khaviz Anticline, Zagros, SW Iran. Petroleum Geoscience 12, 235-246.

Wheeler, J.O., Charlesworth, H.A.K., Monger, J.W.H., Muller, J.E., Price, R.A., Reesor, J.E., Roddick, J.A., and Simony, P.S., 1974. Western Canada,, in: Spencer, A.M., (Eds.), Mesozoic-Cenozoic orogenic belts. Edinburgh, Scottish Academic Press, pp. 591-623.

Wyllie, D.C., and Mah, C.W., 2004. Rock slope engineering: civil and mining. 4th ed. Spon Press, New York.

Yarnold, J.C., 1991. Internal motion and deformation within large rock avalanches during runout: insights from selected localities. Geological Society of America Abstracts with Programs 23, 125.

Zhou, C.H., Yue, Z.Q., Lee, C.F., Zhu, B.Q., and Wang, Z.H., 2001. Satellite image analysis of a huge landslide at Yi Gong, Tibet, China. Quarterly Journal of Engineering Geology and Hydrogeology 34, 325-332.